Quantifying Trends in Methane, Nitrous Oxide, and Carbon Monoxide Emissions in the Los Angeles Basin Using Remote Sensing Spectroscopy at CLARS: Final Report

Title:	**Quantifying Trends in Methane Emissions in the Los Angeles Basin Using Remote Sensing Spectroscopy at CLARS**
Date Submitted:	April 4, 2021
Agreement Number:	17RD030
CARB Contract Manager:	Dr. Matthias Falk
Prepared by:	Zhao-Cheng Zeng and Stanley P. Sander
Principal Investigator:	Stanley P. Sander
Organization:	Joint Institute for Regional Earth System Science and Engineering (JIFRESSE), University of California, Los Angeles
Project Description:	This project aims to (1) extend the CLARS-FTS data record for 2.5 additional years; (2) process the CLARS-FTS spectra to obtain dry air slant column abundances and mixing ratios of the key greenhouse gases CH_4 and CO_2, as well as CO, N_2O (nitrous oxide), water vapor and O_2 (used for filtering the effects of aerosols and clouds); and (3) calculate spatially and temporally-resolved CH_4 emissions. This project will provide CH_4 emissions data from late 2011 through the end of 2020.

Abstract

Legislation in the State of California mandates reductions of 40% in greenhouse gas (GHG) emissions by 2030 and of 80% by 2050. To establish compliance with California legislation, comprehensive, long-term observing strategies are required. In this report, we present the long-term trends of methane (CH_4), Nitrous Oxide (N_2O), and Carbon Monoxide (CO) emissions beginning in 2011 using the California Laboratory for Atmospheric Remote Sensing (CLARS) facility on Mt. Wilson, which is the home of the CLARS-FTS instrument, a scanning Fourier transform spectrometer (FTS) which maps the spatial distributions of GHGs in the Los Angeles (LA) basin. The CLARS-FTS instrument points to a series of locations in the South Coast Air Basin (SoCAB), providing maps every 90 minutes of dry air mole fractions of CH_4 (XCH_4), N_2O (XN_2O), CO (XCO) and a number of other chemical species with a spatial resolution of a few km.

In the first part of this report, we determine the emissions of CH_4 in LA from 2011 to 2019, extending the work of He et al. (2019), using CLARS-FTS observations based on a tracer-tracer ratio method with CO_2 emissions. We show that the pattern of CH_4 emissions contains both seasonal and non-seasonal contributions. We find that the seasonal component peaks in the winter and is correlated (R^2=0.50) with utility natural gas consumption from the residential and commercial sectors and not from the industrial and gas-fired power plant sectors. The non-seasonal component is (14.0 ± 1.3) Gg CH_4/month. If the seasonal correlation is causal, about (1.8 ± 0.18) % of the commercial and residential natural gas consumption in LA is released into the atmosphere. This report updates these numbers, which are different from He et al. (2019), with two more years of CLARS observations and updated background calculations. Identification of the sector(s) responsible for the CH_4 emissions and their temporal and spatial variability is a key step in achieving the goals of emission reduction.

In the second part, we derive urban N_2O emissions for LA using CLARS-FTS observations from 2013 to 2019. N_2O is an important greenhouse gas contributing both to global radiative forcing and ozone depletion. Though N_2O emissions are largely derived from agricultural activities, urban sources of N_2O also contribute significantly to anthropogenic emissions, but are not well understood and difficult to quantify. CLARS-FTS observations yield a weighted mean of 15.0 $\pm$ 0.1 ppb excess XN_2O (XN_2O_{xs}) above background in the LA basin from 2013-2019. The time series of XN_2O_{xs} show a seasonal cycle with a peak-to-peak amplitude of 5.6 $\pm$ 2.5 ppb, where greater XN_2O_{xs} values are observed during the winter/spring and minima occur in late summer/early fall. A tracer-tracer ratio method is applied using XN_2O_{xs} and $XCO_{2,xs}$ observations to estimate top-down N_2O emissions for the LA basin during 2013-2018. Estimated monthly emissions range from 6-19 Gg N_2O per month and exhibit a similar seasonal cycle to that observed in XN_2O_{xs}. Estimated annual emissions fall within the range 124-144 Gg per year for the years 2014-2018. These top-down annual estimates are 2-3 times larger than the CARB statewide bottom-up inventory for the same time period, but consistent considering uncertainties with other top-down estimates for the LA basin. CARB does not release bottom-up emissions data for individual airsheds in the state; only the State totals. Therefore, comparing the CLARS (or other regional measurements) with the CARB statewide emissions values is subject to very large uncertainties.

In the third part, we used CLARS-FTS data to map the excess of XCO in LA. Atmospheric CO is an effective tracer for monitoring atmospheric transport processes and for detecting pollution sources of anthropogenic origin. However, very few observation systems exist that are capable of providing measurements with high spatial and temporal resolution to identify hotspots for emission

control purposes. Here we use CLARS-FTS observations to derive the XCO enhancement, which is the XCO excess in the PBL compared to the background value. In the LA megacity, the XCO enhancement shows a distinctive diurnal cycle primarily driven by changes in anthropogenic emissions and sea-breeze circulation. Such diurnal patterns can be reproduced by the Weather Research and Forecasting model coupled with Chemistry (WRF-Chem). The enhancement also shows a significant weekly cycle resulting from the weekly pattern in anthropogenic CO emissions. On average, the XCO enhancements on Saturday and Sunday are 4.4% and 16.1%, respectively, lower than weekday values. The weekly XCO enhancement patterns also show high correlation with traffic counts. A seasonal pattern of XCO enhancement with high (low) spatial contrast in summer (winter), resulting from changing sea-breeze circulation, can be observed. These diurnal, weekly, and seasonal patterns of XCO enhancement serve as tracers of the atmospheric pulse of the LA megacity.

In the last part of this report, we take advantage of the multi-angle observational geometries of CLARS-FTS to constrain the aerosol angular scattering effect, which is associated with aerosol compositions, using O_2 absorption spectroscopy. CLARS-FTS provides a wide range of scattering angles, from about 20° (forward) to about 140° (backward). We found that the correlation between measurements at different targets can be used to quantify the strength of the angular dependence of the aerosol phase function. Applying the correlation technique to CLARS-FTS measurements, we find that, from 2011 to 2018, there is no significant trend in the aerosol phase function in the LA megacity. Overall, this experiment provides a practical observing strategy for quantifying the angular dependence of aerosol scattering in urban atmospheres.

These results demonstrate the uniqueness of CLARS-FTS in mapping the urban emissions of LA with high spatial and temporal capability. Its measurements are highly sensitive to anthropogenic emissions due to the long light path along the planetary boundary layer. The CLARS observatory can serve as a testbed for future geostationary missions to track anthropogenic emissions in cities.

Table of Contents

Chapter 1. Introduction

The Los Angeles metropolitan area, the second most populous area in the US, is also the largest urban carbon emitter among all US cities (Moran et al., 2018). In response, California has ambitious mandates to reduce greenhouse gas (GHG) emissions. Legislation in the State of California mandates reductions of 40% in GHG emissions by 2030 and of 80% by 2050. Specifically, California will require that by 2035 all new passenger cars and trucks sold in the state be zero-emissions and by 2045 all medium- and heavy-duty vehicles in California be zero-emission (California EXECUTIVE ORDER N-79-20; https://www.gov.ca.gov/wp-content/uploads/2020/09/9.23.20-EO-N-79-20-text.pdf). These efforts will be important milestones to reach the commitment in the Paris Agreement, which aims to substantially cut anthropogenic GHG emissions. Compliances of the agreement by primarily relying on self-reported emission inventories associated with large uncertainties (Gurney et al., 2021) are not sufficient. Measurement, reporting, and verification (MRV), as suggested by the Intergovernmental Panel on Climate Change (Eggleston et al., 2006), should be implemented to ensure that the emissions controls are working on a long-term scale. Direct observations of atmospheric GHGs to estimate emissions have been proven to be an effective way of verifying and validating the outcomes of the mitigation strategies (e.g., McKain et al., 2012; Wong et al., 2016; Nassar et al., 2017).

To establish compliance with California legislation that mandates the rollback of GHG emissions, comprehensive, long-term observing strategies are required. In this report, advanced atmospheric remote sensing methods are utilized to quantify the long term trends of CH_4, N_2O, and CO emissions in the LA basin. We use observations from the California Laboratory for Atmospheric Remote Sensing (CLARS) facility on Mt. Wilson (~1700 meters a.s.l.), which is the home of the CLARS-FTS instrument, a scanning Fourier transform spectrometer. Using instruments and algorithms developed by NASA (National Aeronautics and Space Administration) for space missions, CLARS-FTS maps the spatial distributions of methane (CH_4), carbon dioxide (CO_2), nitrous oxide (N_2O), carbon monoxide (CO), and other species in the Los Angeles (LA) basin with high precision and accuracy traceable to laboratory spectroscopic databases. CLARS-FTS completes a survey of GHG distributions across the LA basin every 90 minutes, retrieving their slant column abundances and dry-air mole fractions. The CLARS-FTS has been measuring trace gases and inferring emissions continuously since September, 2011, thus providing the longest available data record that covers the entire LA basin.

In the following report, we first give a general introduction to the CH_4, N_2O, and CO emissions in LA. In **Chapter 2**, we provide an overview of the observation, data retrieval, and data processing of CLARS-FTS. In **Chapter 3 to 5**, the estimations of CH_4, N_2O, and CO emissions and their long-term trends derived from CLARS-FTS observations are introduced, respectively. In **Chapter 6**, we introduce the use of angular scattering effect of aerosols to infer the long term trend in aerosol compositions in LA. Future plans on using CLARS-FTS observations to constrain the point sources and long term trend toward 2030 are introduced in **Chapter 7**, following by conclusions in **Chapter 8**.

This report is primarily based on the following four publications, including He et al., (2019), Zeng et al. (2020a), Zeng et al. (2020b), and Addington et al. (2021).

[1] Addington, O., Zeng, Z.C., Pongetti, T., Shia, R.L., Gurney, K.R., Liang, J., Roest, G., He, L., Yung, Y.L. and Sander, S.P., 2021. Estimating nitrous oxide (N_2O) emissions for the Los Angeles Megacity using mountaintop remote sensing observations. *Remote Sensing of Environment*, *259*, p.112351. https://doi.org/10.1016/j.rse.2021.112351.

[2] He, L., Zeng, Z.-C., Pongetti, T., Wong, C., Liang, J., Gurney, K. R., Newman, S., Yadav, V., Verhulst, K., Miller, C. E., Duren, R., Frankenberg, C., Wennberg, P. O., Shia, R.-L., Yung, Y. L., Sander, S. P., 2019. Atmospheric methane emissions correlate with natural gas consumption from residential and commercial sectors in Los Angeles. *Geophysical Research Letters*, 46, 8563–8571. https:// doi.org/10.1029/2019GL083400.

[3] Zeng, Z.C., Wang, Y., Pongetti, T.J., Gong, F.Y., Newman, S., Li, Y., Natraj, V., Shia, R.L., Yung, Y.L. and Sander, S.P., 2020a. Tracking the atmospheric pulse of a North American megacity from a mountaintop remote sensing observatory. *Remote Sensing of Environment*, *248*, p.112000. https://doi.org/10.1016/j.rse.2020.112000.

[4] Zeng, Z.-C., F. Xu, V. Natraj, T. J. Pongetti, R.-L. Shia, Q. Zhang, S. P. Sander, and Y. L. Yung, 2020b. Remote sensing of angular scattering effect of aerosols in a North American megacity, *Remote Sensing of Environment*, 242, p.111760. https://doi.org/10.1016/j.rse.2020.111760.

1.1 CH_4 emissions in Los Angeles

CH_4 is a potent greenhouse gas with a number of biogenic and anthropogenic emission sources. CH_4 accounts for about 25% of the change in radiative forcing total from increases in the well-mixed greenhouse gases since the pre-industrial era (Etminan et al., 2016). With an atmospheric lifetime of only about 10 years, CH_4 is a desirable target for greenhouse gas emission reductions because emission controls will have a relatively rapid impact on radiative forcing. In urban areas, the primary sources include landfills, sewage treatment plants and fugitive emissions from natural gas production, storage and distribution systems. In the South Coast Air Basin (SOCAB), which holds more than 43% of California's population, the annual methane emissions estimates based on atmospheric CH_4 observations exceed bottom-up emissions inventories by 30-100%. Therefore, considerable attention is being devoted to reducing the uncertainties in CH_4 emissions estimates and correctly attributing emissions to their sources. In 2015, the Governor approved Assembly Bill 1496 which requires ARB to: Undertake monitoring and measurements of methane "hot spots"; Understand the life-cycle emissions of natural gas produced and imported into California; Review and assess the atmospheric reactivity of methane as a precursor to the formation of photochemical oxidant; Update relevant policies and programs to incorporate new information. Legislation in the State of California mandates reductions in emissions of short-lived climate pollutants of 40% from 2013 levels by 2030 for CH_4 (*California Legislature*, 2006). In the LA basin and other urban areas, previous studies focused on methane source attribution have used a variety of methods including C_2H_6 as a tracer for fossil methane, and measurements of CH_4 isotopologues to distinguish fossil and biogenic sources (Wennberg et al., 2012; Hopkins et al., 2016; Wunch et al., 2016). These studies indicate that fugitive natural gas emissions account for 56-70% of the difference between annual top-down and bottom-up (annual excess) CH_4 emissions in LA (Wennberg et al., 2012; Peischl et al., 2013; Hopkins et al., 2016).

Almost all previous studies were restricted in spatial and/or temporal coverage and none were able to determine which segments and operations of the natural gas distribution system were responsible for the leakage. Wennberg et al. (2012) proposed that many small leaks downstream of the gas meters could be responsible rather than the transport, storage and distribution segments. Identifying and quantifying the sources of these emissions is critical because methane budgets vary between urban areas, so understanding the emission pathways is essential for mitigation (McKain et al., 2015; Lamb et al., 2016; Jeong et al., 2017).

Using the tracer-tracer correlation method combined with a highly resolved CO_2 emissions inventory, Wong et al. (2016) showed that it was possible to identify seasonal peaks in spatially-aggregated CH_4 emissions in LA. CH_4 emission peaks up to 37 Gg/month were consistently observed in the winter seasons, with a low of 27 Gg/month in the summer. These levels were revised upward in the present study as a result of changes to the underlying CO_2 inventory. Overall, the measured SOFCAB CH_4 emissions were 2-31% higher than the scaled statewide bottom-up emissions estimated by the California Air Resources Board (CARB) from 2011-2013 averaged over the three years (CARB, 2011). This result is consistent with other studies that obtained larger emissions than CARB estimates (Wunch et al., 2009; Hsu et al., 2010; Wennberg et al., 2012; Peischl et al., 2013; Wong et al., 2015; Conley et al., 2016; Wong et al., 2016; Wunch et al., 2016; Cui et al., 2017; Hedelius et al., 2018; Yadav et al., 2019). No seasonal variability has been observed in other intensively monitored cities including Indianapolis and Boston although these cities differ significantly from Los Angeles in topography, meteorology, infrastructure and other factors that influence methane emissions (McKain et al., 2015; Lamb et al., 2016).

In this study, we resolve seasonal and spatial variability of CH_4 emissions from 2011 to 2019 and regress it against consumption data as an important step towards reconciling California's methane budget. The goal is first to leverage our powerful 2011–2019 data record to quantify seasonal to interannual variability in LA CH_4 emissions. Secondly, we investigated whether the seasonality of LA CH_4 emissions is related to natural gas consumption. Finally, we quantified the relative contribution of each sector (including residential, commercial, industrial, vehicle, and power plant) to the seasonality of LA CH_4 emissions. The results of CH_4 are shown in **Chapter 3**.

1.2 N_2O emissions in Los Angeles

Nitrous oxide (N_2O), an important greenhouse gas, is the third largest contributor to global radiative forcing (Stein and Yung, 2003; Butler and Montzka, 2020). Compared to other non-CO_2 greenhouse gases, N_2O has a relatively high global warming potential of 298 on a 100-year time scale and a long atmospheric lifetime of approximately 114 years (US EPA, 2019). Less than 1% of atmospheric N_2O is removed annually, primarily by UV photolysis in the stratosphere (Montzka et al., 2011). A smaller portion undergoes a photo-oxidation reaction with $O(^1D)$, which produces NO_x and in turn contributes to ozone depletion in the stratosphere (Morgan et al., 2004). For these reasons, nitrous oxide is one of the greenhouse gases targeted for emission reduction by the Kyoto protocol (1997) and a focus of global monitoring networks. The present-day atmospheric concentration of 330 ppb (Butler and Montzka, 2020) is significantly greater than pre-industrial levels, estimated around 270 ppb using ice-core and firn air samples (Machida et al., 1995; Battle et al., 1996). Many studies have characterized the annual increase from pre-industrial levels as quasi-linear with a global slope value ranging between 0.7–1.0 ppb/year during the last century (Prinn et al., 1990; Machida et al., 1995; Prinn et al., 2000; Thompson et al., 2004). Thompson et al. (2004) suggested that the magnitude of this growth rate depends on latitude, as larger growth rates are observed in the Northern hemisphere with interhemispheric differences ranging from 0.4 to 1.4 ppb/year from 1987 to 2003. The growth rate also exhibits some interannual variability, which may be attributed in part to variations in tropospheric transport, the magnitude of the stratospheric sink, and the influence of El Niño conditions in certain years (Nevison et al., 2007). Finally, several studies report an observed acceleration in this growth rate over the last century (e.g. Prinn et al.,1990; Battle et al.,1996). According to the World Meteorological Organization Greenhouse Gas Bulletin for observations through 2018, the increase in atmospheric concentrations from 2017 to 2018 was larger than both the increase from the previous year and the average growth rate of the past decade (WMO, 2019).

Other studies observe a significant seasonal cycle in tropospheric N_2O (e.g., Liao et al., 2004; Nevison et al., 2004; Jiang et al., 2007; Nevison et al., 2007). Like the growth rate, the phase and peak-to-peak amplitude of the seasonal cycle has a latitudinal dependence. In the Northern hemisphere, this seasonal cycle appears to have a minimum during late spring/early summer, which is attributed to an influx of N_2O-poor air from the stratosphere due the seasonally varying strength of Brewer-Dobson circulation (Jiang et al., 2007). This explanation is supported by studies showing a correlation between the seasonal cycles of N_2O with other long-lived atmospheric gases such as chlorofluorocarbons (CFCs), which act as tracers for N_2O since both are well-mixed in the troposphere and are primarily destroyed by photochemical reactions in the stratosphere (Nevison et al., 2004). Finally, the observed seasonal amplitudes for the Northern hemisphere are greater than those observed for the Southern hemisphere (e.g. Nevison et al., 2004; Zhou et al., 2019).

Jiang et al. (2007) reported amplitudes at high latitudes exceeding 1 ppb compared to an observed amplitude of 0.29 ppb for the South Pole.

The increase in global N_2O concentrations from pre-industrial levels is attributed to both natural and anthropogenic sources. The largest source of global N_2O emissions is microbial activity in fertilized agricultural soils, as nitrous oxide is a biproduct of nitrification/ denitrification processes occurring within the global nitrogen cycle (US EPA, 2019). Therefore, growing global concentrations are largely linked to the increased use and production of inorganic fertilizers along with the cultivation of nitrogen-fixing crops (Montzka et al., 2011). Agricultural activities also generate indirect emissions in the form of leaching and run-off, which can in turn increase emissions from natural soils and bodies of water (Syakila and Kroeze, 2011). Other anthropogenic sources of N_2O emissions include fossil fuel combustion, chemical production, biomass burning, and treatment of domestic wastewater (US EPA, 2019). While a fair amount of research has been done to investigate mechanisms for N_2O production in plants under various agricultural management practices (e.g., Horwath, 2012; Butterbach-Bahl et al., 2013) and some research has worked to estimate emissions from wastewater treatment plants (e.g., Wunderlin et al., 2011; Daelman et al., 2015; Vasilaki et al., 2019) and automobile combustion (e.g., Huai et al., 2004; Borsari and Assunção, 2009; Graham et al., 2009), urban sources of nitrous oxide are not well understood or quantified. Estimating N_2O emissions using bottom-up approaches includes significant uncertainties because of the difficulty in quantifying sources and an incomplete understanding of emissive processes (Montzka et al., 2011).

Most N_2O emission inventories are derived at the state or national level while few attempts have been made to estimate nitrous oxide emissions for an urban region. In California, interest in quantifying local emissions is stimulated by state and city policy goals concerning emission reduction and air quality improvements. The California Global Warming Solutions Act, which was passed in 2006, aims to reduce GHG emissions in California to 40% below 1990 levels by 2030. As California is home to a number of large cities, like Los Angeles, which contain large proportions of the statewide population and contribute significantly to anthropogenic emissions, monitoring urban emissions plays an important role in the statewide goal. Airborne campaigns, such as CalNex in 2010, have aimed to quantify emissions for both rural and urban regions in California, such as the Central Valley and greater Los Angeles, respectively (Xiang et al., 2013). In addition, the Total Carbon Column Observing Network (TCCON), a ground-based Fourier Transform spectrometer (FTS) network, has sites within the SoCAB, which encompasses greater LA, that have been taking total column GHG measurements, including N_2O, starting in 2007 (Wunch et al., 2009).

While airborne campaigns provide data in target regions with high spatial resolution, the temporal extent of these measurements are limited, given that flights are conducted infrequently. Similarly, ground-based networks provide data with high temporal resolution, as GHG concentrations are measured frequently, but can only provide limited spatial coverage for a sprawling megacity like Los Angeles. This study uses remote sensing observations from CLARS-FTS to quantify nitrous oxide emissions for the Los Angeles Basin by applying a top-down tracer-tracer ratio method to N_2O and CO_2 observations. This method has been previously employed to study urban methane (CH_4) emissions in Los Angeles (Wunch et al., 2009; Wong et al., 2015; Wong et al., 2016). Towards this goal, this study also investigates the temporal trends of N_2O mixing ratio excess within the LA basin. Given the importance of megacities to anthropogenic emissions, the methods

applied in this study could serve as a model for new approaches to monitoring urban greenhouse gases. The results of N_2O are shown in **Chapter 4**.

1.3 CO and Aerosols in Los Angeles

After decades of emissions control in California, the air pollutants associated with passenger cars have decreased substantially. However, LA is still one of the most polluted cities in the US. Its large anthropogenic emissions, special meteorological conditions, and unique geographic landscape are favorable for smog formation and lead to severe air quality problems in LA. Extensive bottom-up and top-down studies have been conducted in LA to quantify anthropogenic emissions on a basin-wide scale (e.g., Cui et al., 2015; Hedelius et al., 2018; Gurney et al., 2019). However, to implement effective emission control policies, advanced top-down measurements must be able to capture the fine-scale spatial/local emission gradients. More than 83% of CO is emitted from mobile sources (of which 47% are from on-road motor vehicles) as indicated by bottom up CO emission estimates (CARB, 2016) in the SOCAB, which consists of the urban areas of LA, Orange, Riverside, and San Bernardino counties in Southern California. Since CO is an effective tracer of atmospheric transport process, quantification of the diurnal, weekly, and seasonal patterns of XCO enhancement will shed light on the atmospheric emissions of trace gases in the LA megacity, possibly leading to better emission reduction strategies to mitigate their adverse effects on public health and global warming. Moreover, CO is also a tracer for emissions of several other co-emitted species, including volatile organic compounds (Borbon et al., 2013), CO_2 (Gamnitzer et al., 2006) and black carbon (Guo et al., 2017); knowledge gained from XCO will help constrain these co-emitted species.

CO is emitted to the atmosphere mainly as a result of incomplete combustion. CO has an adverse impact on public health because of its toxicity. It also participates in atmospheric chemical reactions that form ozone. The fact that CO has a low background concentration and moderately long atmospheric residence time from weeks to months (Holloway et al., 2000) makes it an effective tracer for monitoring atmospheric transport processes as well as for detecting pollution sources of anthropogenic origin (e.g., Pommier et al. 2013; Borsdorff et al. 2018a). In order to identify hotspots for emissions control purposes, observation systems and networks must be capable of providing measurements with high spatial and temporal resolution.

Space-borne instruments, e.g., Tropospheric Monitoring Instrument (TROPOMI; Borsdorff et al. 2018b), Measurement of Pollution in the Troposphere (MOPITT; Jiang et al., 2017) and Tropospheric Emission Spectrometer (TES; Rinsland et al., 2006), provide measurements of CO with global coverage. However, CO measurements from space-borne instruments (e.g., TES) only observing at the CO absorption channel at 4.7 μm in the thermal infrared band are strongly weighted to the mid-troposphere and relatively insensitive to the PBL CO variability. Borsdorff et al. (2019c) demonstrated that TROPOMI can detect CO on sub-city scales. However, these measurements from Low Earth Orbiting (LEO) satellites have limited temporal resolution (usually one overpass a day), and are not an ideal proxy for local emissions partly due to their weak sensitivity to surface layer CO mixing ratio (Jiang et al., 2018). Ground-based measurements of CO in cities, e.g., from the Total Carbon Column Observing Network (TCCON) (Wunch et al., 2009; Hedelius et al., 2018) and the NASA megacity network (Verhulst et al., 2018) have limited spatial coverage. Such limitations make them rely heavily on transport modeling (Feng et al., 2016), whereby the model transport module may contribute non-negligible uncertainties to fine scale

simulation (Lauvaux et al. 2009), for inferring urban-scale emissions. In this study, we present the results from CLARS-FTS on mapping the CO column-averaged dry-air model fraction (XCO) enhancement in the LA megacity. The results are shown in **Chapter 5**.

The CLARS observation geometry makes the measurements not only highly sensitive to the atmospheric composition but also very susceptible to influence by aerosol scattering and absorption due to the long light path across the boundary layer (Zhang et al., 2015; Zeng et al., 2017). Using absorption spectroscopy of molecular oxygen, Zhang et al. (2015) and Zeng et al. (2017) demonstrated the capability of CLARS-FTS observations in monitoring the air pollutants in the LA basin. Aerosols, including those that contribute to poor air quality, are produced primarily within the planetary boundary layer (PBL), which is the bottom layer of the atmosphere and couples the Earth's surface and the atmosphere above. However, this near-surface layer is relatively poorly modeled, including the air pollutants trapped within this mixing layer. Aerosols in the atmosphere affect the Earth's energy balance directly by scattering and absorption of sunlight and indirectly through aerosol-cloud interactions. It has been shown that the aerosol direct and indirect effects are the two largest sources of uncertainties in quantifying anthropogenic radiative forcing (Stocker et al., 2014). The adverse impact of aerosols on public health makes particulate matter air pollution the world's largest environmental health risk (Heft-Neal et al., 2018).

A wide range of observation techniques, including space-based, airborne, and ground-based remote sensing, has been developed to provide constraints on the aerosol optical and microphysical properties. However, due to the large spatiotemporal variation in the loading, vertical distribution and microphysical properties of aerosols, their effects on the retrieval uncertainty in greenhouse gas measurements space are not well quantified. Multi-angle measurements provide additional constraints on the angular dependence of aerosol scattering (Diner et al., 2018). The aerosol phase function, which characterizes the angular signature of scattering, has been continuously monitored from ground-based and space-borne observations. The ground-based network of AERONET stations has been instrumental for global monitoring of aerosol variability and retrieval of their optical and microphysical properties, including phase function (Kaufman et al., 1994; Dubovik et al., 2000). The NASA Multi-angle Imaging SpectroRadiometer (MISR; Diner et al., 2005) has been successful in retrieving aerosol microphysical properties associated with different anthropogenic and naturally occurring aerosol types (Kahn et al., 2001). Benefiting from its multi-angle observing capability, MISR is able to sample a large range of scattering angles, from about 60° and about 160° at mid-latitudes, concentrating on backward scattering (>90°) for most of their observing angles. However, the range of scattering angles these instruments can sample in the forward scattering directions is limited. Ground-based instruments mostly focus on forward scattering, whereas space-borne instruments concentrate on backward scattering. There is a dearth of research on the remote sensing of aerosol angular scattering effects over a wider range of scattering angles (from backward to forward), especially with relevance to observing at city scales with diurnal capability.

This study of using CLARS-FTS observations to investigate urban aerosols in LA has two objectives. First, we report multi-year (2011–2018) measurements of aerosol scattering, at a wider range of scattering angles than any existing instrument, from CLARS-FTS, which provides diurnal observations of aerosol scattering inside the LA megacity. Second, we use measurements of oxygen absorption from CLARS-FTS to investigate the diurnal and seasonal variabilities of angular scattering due to aerosols in the LA basin. Since oxygen is a well-mixed gas with known

concentration, the measurement is a proxy for the average length of the light paths (direct and scattered) and therefore an indicator of the strength of aerosol scattering. The results of aerosols are shown in **Chapter 6**.

Chapter 2. Overview of CLARS observatory

2.1 CLARS-FTS

CLARS, a novel mountain-top observatory, is a first-of-its-kind observation system to monitor urban emissions from a top-down perspective. CLARS is unique in the following ways: (1) it mimics a geostationary satellite observatory for LA with approximately hourly- and kilometer-scale mapping capability; (2) the free tropospheric background atmosphere is measured simultaneously; and (3) the measurements are highly sensitive to anthropogenic emissions due to the long light path along the planetary boundary layer (PBL). As shown in **Figure 2.1**, compared to satellite, CLARS has a longer path in the PBL compared to satellite measurements and therefore higher sensitivity to urban emissions. Compared to ground/tower-based stations that only sample the bottom layer of the atmosphere and are subject to the highly variable boundary layer height, CLARS samples the whole atmospheric column and is therefore not affected by this issue. The CLARS-FTS has been measuring greenhouse gases (GHGs) and air pollutants continuously since September, 2011, thus providing the longest available data record that covers the entire LA basin.

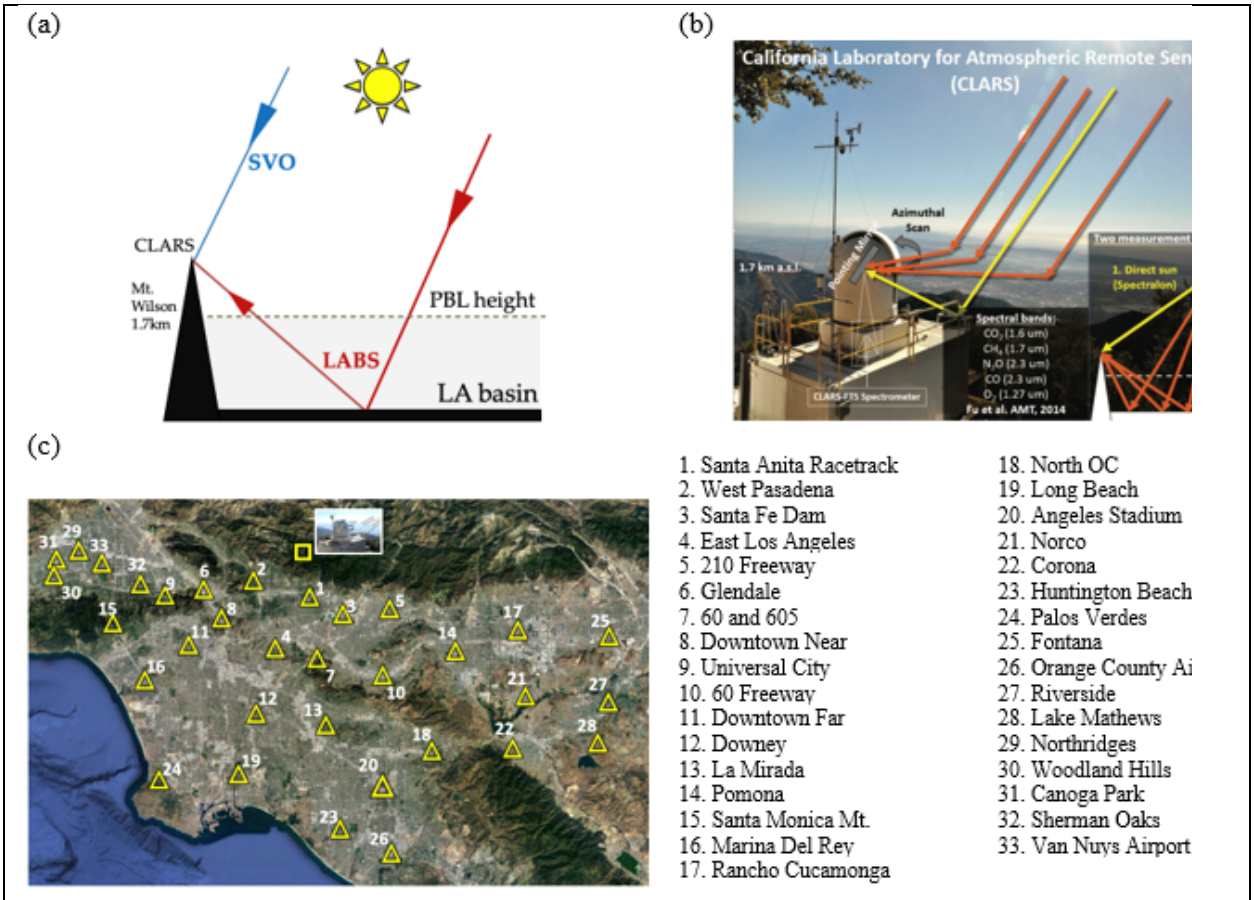

Figure 2.1. (a) Schematic figure showing the observation geometries and modes, including Los Angeles Basin Survey (LABS) and Spectralon Viewing Observation (SVO) modes, of CLARS-FTS; (b) CLARS observatory on the top of Mt. Wilson overlooking the LA basin and measures column abundances of CO_2, CH_4, N_2O, CO, O_2, and other trace gases; (c) The 33 surface reflection points across the Los Angeles basin. The background image is adopted from © Google Earth.

CLARS-FTS was designed and built at Jet Propulsion Laboratory (JPL). It is optimized for reflected sunlight measurements with high spectral resolution in the near-infrared (NIR) region (4,000 –15,000 cm^{-1}). CLARS-FTS uses a pointing system to target a set of predefined reflection points in the LA basin as well as a local diffuse reflector (Spectralon) for measurements of the free tropospheric background (**Figure 2.1**). As shown in **Figure 2.2**, the surface reflection points of CLARS are densely distributed and are capable of capturing the changes in GHGs over the whole basin. Two operating modes are on the CLARS-FTS measurement schedule: Los Angeles Basin Surveys (LABS), and Spectralon Viewing Observations (SVO). In LABS mode, the pointing system stares at each ground site in the LA basin and CLARS-FTS records atmospheric absorption spectra using reflected sunlight as the light source. In SVO, CLARS-FTS measures the trace gas concentration above the CLARS site by pointing at a Spectralon (diffuse reflector) target on the rooftop. Since the CLARS mountaintop site is located above the boundary layer, SVO measurements give the background trace gas abundances in the free troposphere. In the downward viewing geometry used in the CLARS-FTS measurements, the sunlight travels through the boundary layer twice: once on the way to the target and a second time from the target to CLARS. The resulting light path through the boundary layer is typically greater than 20 km which is several times longer than other commonly used viewing geometries, e.g., observing the direct solar beam from the surface, or measurement of surface-reflected sunlight from aircraft and spacecraft vantage points. CLARS covers the whole basin every 1.5 hours. Depending on the season, the total number of observations within a single day ranges from 160 to 260, and the number of repeated scans of the whole basin is between five to eight times. Additional details may be found in Fu et al. (2014).

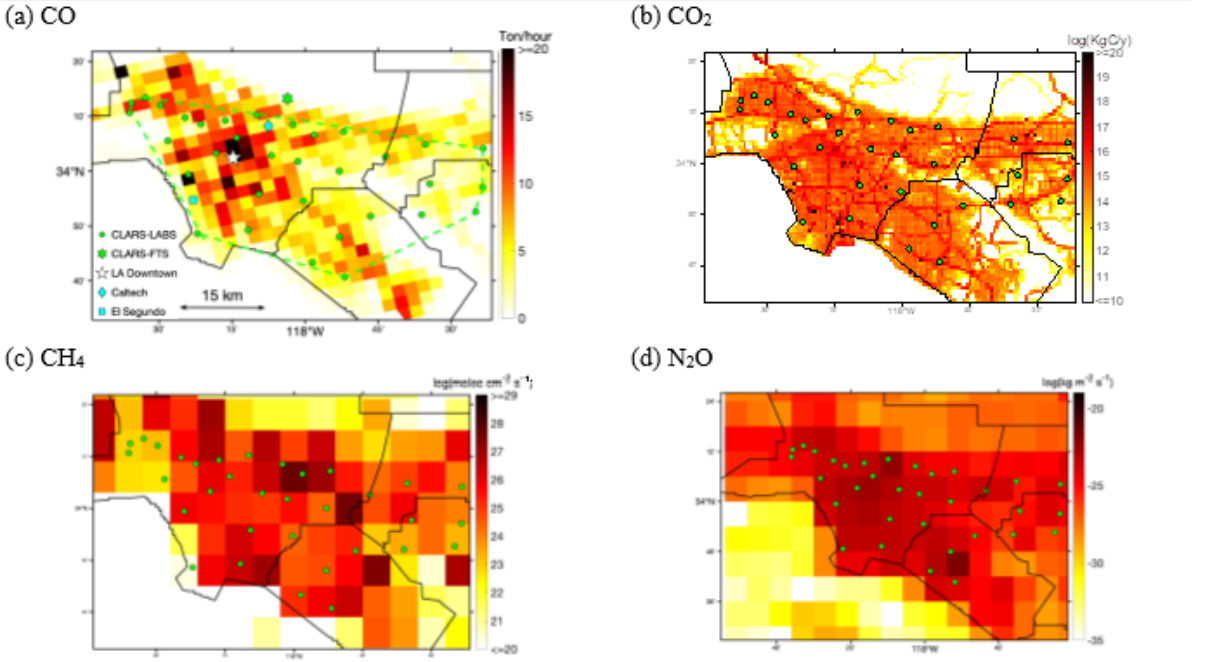

Figure 2.2. The spatial distribution of *a priori* emissions of CO_2, CH_4, N_2O, and CO, overlaid with the 33 CLARS surface targets. The CH_4 emission inventory comes from the EPA gridded 2012 methane emissions (0.1-degree resolution); The CO emission inventory comes from the National Emissions Inventory (NEI) by EPA (4-km spatial resolution). The CO_2 emission inventory comes from Hestia project (1-km spatial resolution); The N_2O emission inventory comes from the Emission Database for Global Atmospheric Research (EDGAR; 0.1-degree resolution).

2.2 CLARS-FTS Retrievals of GHGs

2.2.1 Slant column density and dry-air mole fraction of trace gases

To derive slant column densities (SCDs) of atmospheric trace gases from the measured absorption spectra, we use the retrieval algorithms of CLARS-GFIT, which is a modified version of the GFIT program (Fu et al, 2014), to retrieve CO_2, CH_4, N_2O, CO, and O_2 SCDs using the same spectral bands and spectroscopic parameters used by the Total Carbon Column Observing Network (TCCON; Toon et al., 1992; Wunch et al., 2011) network. From retrieved SCDs, dry-air column averaged volume mixing ratios of greenhouse gases (XGHGs) are calculated by normalizing GHG SCD measurements to the dry-air total column, which can be derived from the measured SCD for O_2 (**Equation 2.1**) and the dry-air O_2 mole fraction:

$$XGHG = 0.2095 * \frac{SCD_{GHG}\ (mol\ GHG/m^2)}{SCD_{O2}\ (mol\ O_2/m^2)} \quad (2.1)$$

Using this method improves measurements of trace gas mixing ratios since any existing systematic errors in retrievals of both the greenhouse gas and O_2 SCDs will be minimized in computing the ratio (Fu et al., 2014).

2.2.2 Data filtering

Before the retrieved mixing ratio data are analyzed, several filters summarized in **Table 1** are applied to remove low quality retrievals (Wong et al., 2015). Data with poor spectral fitting, identified as instances with large solar zenith angles (SZAs), low signal-to-noise ratios (SNRs), and large root-mean-square (RMS) values from the spectral fitting, are removed. Retrievals with high uncertainty values, defined as more than 3 times the standard deviation from the mean uncertainty, are also removed. Additionally, the ratio between retrieved and geometric O_2 slant column densities are used to remove retrievals affected by cloud and aerosol scattering. The geometric O_2 SCD is calculated assuming no scattering occurs, along with additional assumptions outlined in Fu et al. (2014). Because oxygen is well-mixed in the atmosphere, deviation in the retrieved O_2 SCD from the geometric O_2 SCD implies variations in the light path due to clouds and/or aerosols (Zeng et al., 2018; Zeng et al., 2020), and can therefore be used to identify observations that represent especially cloudy or hazy days. The filter criteria for the ratio between retrieved and geometric O_2 is slightly different for LABS and SVO data sets due to the enhanced influence of boundary layer aerosols on LABS retrievals. In general, aerosol scattering results in shorter light paths through PBL, and based on the viewing mode geometries, LABS retrievals are more likely to have retrieved/geometric O_2 SCD ratios that are less than 1.0.

Table 1: Data filter criteria for removing low quality retrievals

Filter	Criterion for removal
High clouds	SVO $O_{2\ \text{SCD Retrieved}} : O_{2\ \text{SCD Geometric}}$ ≥ 1.1 or ≤ 1.0
Low clouds and/or aerosols	LABS $O_{2\ \text{SCD Retrieved}} : O_{2\ \text{SCD Geometric}} \geq 1.1$ or ≤ 0.9
Large SZA	SZA ≥ 70
Low SNR	SNR ≤ 100
Poor spectral fitting	Fitting residual RMS $\geq$ 1 standard deviation above mean

Figure 2.3 shows the measurements of XCO_2, XCH_4, XN_2O, and XCO from CLARS LABS and SVO modes from September 2011 to December 2020. The target observations in the PBL are significantly higher than the Spectralon observations that are the free tropospheric background measurements. Steady increases in XCO_2, XCH_4, and XN_2O can be observed due to the excess of annual anthropogenic emissions in the atmosphere. The XCO, however, shows a slightly decreasing trend attributable to improved emission controls in the automobile fleet. A detailed analysis of these trace gases is present in the following sections.

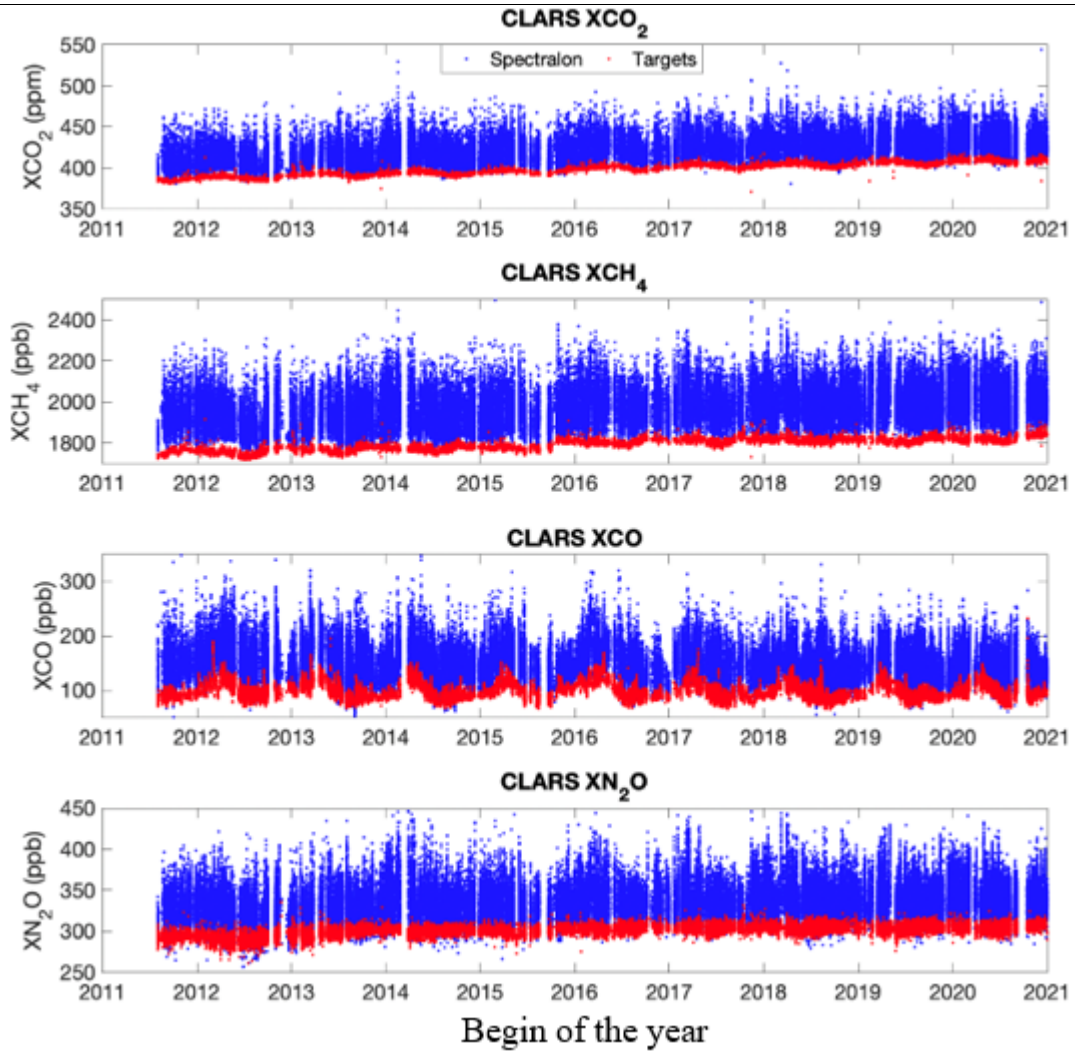

Figure 2.3. Measurements of XCO_2, XCH_4, XN_2O, and XCO by CLARS-FTS from 2011 to 2020. The LABS mode (blue symbols) measures the trace gas concentration within the boundary layer while the SVO mode (red symbols) measures the background value above the boundary layer.

2.3 Tracer-tracer method to estimate CH_4 and N_2O emissions

The XGHG excess is calculated by subtracting the overall background estimation from the XGHG LABS retrievals:

$$XGHG_{xs} = XGHG_{LABS} - XGHG_{Background} \quad (2.2)$$

The uncertainty in the corrected $XGHG_{xs}$ value is calculated using error propagation based on LABS retrieval uncertainties and uncertainties in the background estimate. Using **Equation (2.2)**, the XCH_4 excess ($XCH_{4,xs}$), XN_2O excess (XN_2O_{xs}), and XCO_2 excess ($XCO_{2,xs}$) are calculated. In order to confine analysis to emissions within the basin, $XCO_{2,xs}$ values less than 2ppm are removed, as in Wunch et al. (2009). A basin-averaged emissions value for CH_4 and N_2O can be separately estimated by applying a tracer–tracer correlation method to XCH_{4xs} versus $XCO_{2,xs}$, and XN_2O_{xs} versus $XCO_{2,xs}$, respectively. The objective of this method is to derive an alternate CH_4 and N_2O emission estimates for comparison against bottom-up emissions inventories. These results are especially useful for greenhouse gases like CH_4 and N_2O, which are more difficult to constrain using bottom-up estimation methods compared to CO_2, whose emission sources are well-known and quantifiable to a high degree of accuracy. This tracer-tracer method was previously applied using CLARS-FTS observations to estimate CH_4 emissions for the LA basin (Wong et al., 2016).

In this method, excess ratios of (XN_2O_{xs}/ $XCO_{2,xs}$) and ($XCH_{4,xs}$/ $XCO_{2,xs}$) are separately calculated for each observation. These ratios can be averaged on different time scales in order to reduce associated uncertainties. Although previous studies which employed CLARS-FTS observations to study urban methane, such as Wong et al. (2016), used orthogonal distance regression (ODR) to quantify monthly correlations between excess mixing ratios, He et al. (2019) found that data anomalies may bias estimated correlation slopes and thereby affect the determination of emission ratios. Therefore, the method of determining monthly excess ratios in order estimate top-down CH_4 and N_2O emissions was adjusted to be consistent with the method developed in He et al. (2019), which averages individual observations over various time scales. A basin-averaged excess ratio value (R_{basin}) is calculated for each given year and month by weighting individual observations by their uncertainties. The formula for the basin-averaged monthly ratio is given by **Equation 2.3**:

$$R_{basin,monthly} = \frac{\sum_{i=1}^{i=N} r_i w_i}{\sum_{i=1}^{i=N} w_i} \text{ where } w_i = \frac{1}{\sigma_i^2} \tag{2.3}$$

where N is the total basin measurements for a given month and year, r_i is the ratio value for an individual observation, and the weight w_i is defined as the reciprocal of the squared uncertainty in the ratio observation. Uncertainty values, σ_i, are determined by applying standard rules of error propagation to the individual uncertainties of XN_2O_{xs} (or $XCH_{4,xs}$) and $XCO_{2,xs,}$ both of which are largely dominated by the original retrieval uncertainties. Top-down N_2O (or CH4) emissions can then be estimated for the LA basin using the basin-averaged XN_2O_{xs}/ $XCO_{2,xs}$ ratio value (or $XCH_{4,xs}$/ $XCO_{2,xs}$) and a bottom-up CO_2 emission inventory, correcting for the difference in molar mass by multiplying the ratio of the molecular weights of the two GHGs (**Equation 2.4**):

$$E_{N_2O}|_{top\ down} = E_{CO_2}|_{bottom\ up} \times R_{basin,monthly} \times \frac{MW_{N_2O}}{MW_{CO_2}} \tag{2.4}$$

In this study, the bottom-up CO_2 monthly emissions estimates are derived using Hestia-LA v.2.5 (Gurney et al., 2019, data available at: https://doi.org/10.18434/T4/1502503), CARB CO_2 estimates (California Environmental Protection Agency Air Resources Board, 2019b, data available at: https://www.arb.ca.gov/app/ghg/2000_2017/ghg_sector.php), and ODIAC CO_2 emissions (https://db.cger.nies.go.jp/dataset/ODIAC/). Hestia-LA is a high spatial resolution bottom-up CO_2 emission dataset that has been developed for the Los Angeles Basin (Gurney et al., 2012, 2019). Hestia-LA provides CO_2 emissions associated with the combustion of fossil fuel and cement production in five counties (Los Angeles, Orange, San Bernardino, Riverside and Ventura) in the LA Basin. The Hestia dataset provides more accurate estimates for CO_2 emission in the LA

Basin than other widely used datasets such as Open-source Data Inventory for Anthropogenic CO_2 and Fossil Fuel Data Assimilation System (Wong et al., 2015). The random and systematic error in the Hestia-LA gives the uncertainty around 11% with 95% confidence interval (Gurney et al., 2019). A comparison of CO_2 emission inventories from Hestia, CARB, and ODIAC is shown in **Figure 2.4**. CARB inventory is scaled from state total emission by population ratio of SOCAB (18 million) to total California population (38 million). To match the mean value of Hestia, CARB inventory is further scaled by 0.69. ODIAC is shifted upward by 3.5TgCO_2/month. Consistencies between the three datasets can be clearly observed. Scaled CARB and ODIAC present a decreasing trend from 2011 to 2018. The seasonal cycles amplitudes between Hestia and shifted ODIAC are also consistent. We therefore use the shifted ODIAC emissions for the following analysis since it provides the most updated data to 2019. Emission estimate for the year 2020 in LA, which has been shown to be greatly affected by the lock-down measures during COVID-19 pandemic, is not available at this moment, and will not be analyzed in the report. Monthly N_2O (or CH_4) emissions estimates for the LA basin can be computed by combining the monthly emission values with the excess ratio of XN_2O_{xs}/ $XCO_{2,xs}$ (or $XCH_{4,xs}$/ $XCO_{2,xs}$) using **Equation 2.4**.

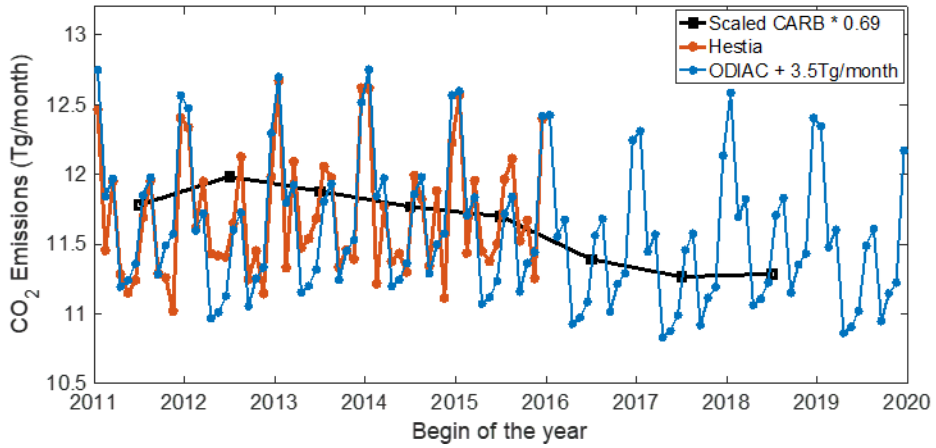

Figure 2.4 A comparison of CO2 emission inventories from Hestia, CARB, and ODIAC. CARB inventory is scaled from state total emission by population ratio of SOCAB (18 million) to total California population (38 million). CARB inventory is further scaled by 0.69 to fit the Hestia total. ODIAC is shifted upward by 3.5TgCO2/month to match the Hestia. The CO2 emission inventories are assumed to have a 10% uncertainty (Gurney et al., 2019).

In order to justify the application of the above tracer-tracer ratio method, the correlation of XN_2O_{xs} and $XCO_{2,xs}$ (or $XCH_{4,xs}$ and $XCO_{2,xs}$) was checked for each surface reflection point location using orthogonal distance regression. Such correlation has been carefully examined by Wong et al (2005) and Wong et al. (2006). Here, we only show the result for XN_2O_{xs}. Using orthogonal distance regression (ODR), rather than simple linear regression, allows for consideration of uncertainties in both GHG mixing ratios. With the exception of surface reflection point #29, which was omitted from analysis due sparse data post- filtering, correlations for all surface reflection point locations had p-values < 0.01, where in most cases the p-value was in fact much smaller, i.e. < 0.002. The R^2 value for all correlations was larger than 0.4 and for a majority of surface reflection points, $R^2 >$ 0.55. **Figure 2.5** provides an example of ODR results for two specific surface reflection points, Santa Anita Race Track and West Pasadena, whose locations within SoCAB can be seen in **Figure 2.1(c)**. In addition to illustrating the presence of a correlation between XN_2O_{xs} and $XCO2_{xs}$ values,

Figure 2.5 also shows the variability in the correlation slope value for different surface reflection point locations.

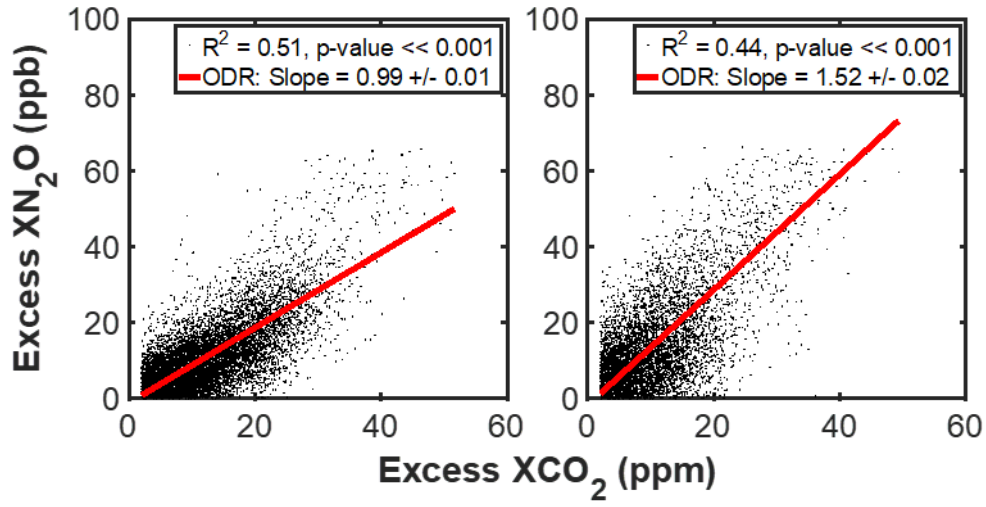

Figure 2.5: $XN_2O_{xs}/XCO_{2,xs}$ ODR correlation plots for two example surface reflection points, Santa Anita Race Track (left) and West Pasadena (right), where ODR slopes are shown by the red lines. The R^2 values for both plots are greater than 0.4 and the p-values for both plots are much smaller than 0.001.

Certain assumptions are inherent in applying this tracer-tracer ratio method to derive top down N_2O emissions. In a manner similar to section 4.1 of Wong et al. (2015), these assumptions are discussed in detail in **Appendix A1**. The main points are summarized here. First, we assume XN_2O_{xs} and $XCO_{2,xs}$ are correlated even though the two GHGs are not emitted from the same sources. This assumption is based on the fact that these GHGs behave like inert tracers in the PBL given their relatively long chemical lifetimes. Second, we assume the averaged $XN_2O_{xs}/XCO_{2,xs}$ ratio for a given surface reflection point is sensitive to emissions over a horizonal path weighted toward the reflection point, along with air mass advected into the atmospheric path, and is therefore relatively independent of local emission ratio variations. Finally, the effect of aerosol scattering on the $XN_2O_{xs}/XCO_{2,xs}$ excess ratio is assumed to be negligible. Evidence to support this assumption is presented in the discussion section of **Chapter 4**.

Chapter 3. CH_4 emissions in LA from 2011 to 2019

In this study, we resolve seasonal and spatial variability of CH_4 emissions from 2011 to 2019 and regress it against consumption data as an important step towards reconciling California's methane budget. The goal is first to leverage our powerful 2011–2019 data record to quantify seasonal to interannual variability in LA CH_4 emissions. Secondly, we investigated whether the seasonality of LA CH_4 emissions is related to natural gas consumption. Finally, we quantified the relative contribution of each sector (including residential, commercial, industrial, vehicle, and power plant) to the seasonality of LA CH_4 emissions.

3.1 Background estimation for XCH_4 and XCO_2

To use the tracer-tracer method, as introduced in **Chapter 2**, to estimate CH4 emissions, we need to examine temporal distributions of excess XGHG ($XGHG_{xs}$), which requires the determination of the XGHG background. In this study, the background is defined using SVO observations along with NOAA Mt. Wilson Observatory (MWO) *in-situ* flask measurements collected near the CLARS-FTS instrument (https://www.esrl.noaa.gov/gmd/dv/site/MWO.html?stacode=MWO). CLARS Spectralon retrievals represent free tropospheric mixing ratios for the atmosphere above CLARS-FTS, while nighttime flask measurements can be used as a representation of the background for the portion of the atmosphere below CLARS-FTS. This is justified by the fact that the height of the PBL reduces to far below the CLARS facility during the night, and therefore, in-situ measurements approximate background conditions for the lower troposphere over the region without human activities. Using both data sets allows the derivation of an unbiased background along the same optical path as LABS measurement mode.

The NOAA portion of the background is determined using the nighttime measurements collected between the hours of 22:00 and 6:00 Local Time. Then the overall background is determined by weighting SVO and NOAA background estimates according to the number of molecules in the respective path lengths. The SVO background is applied for the path above CLARS height and the NOAA background is applied (1) for the path from the CLARS height to the surface and (2) for the reflected path from the surface to the CLARS instrument. A full explanation of background calculation is provided in **Appendix A2**.

3.2 Auxiliary datasets

3.2.1 Monthly natural gas consumption dataset

Natural gas usage data are the sum of natural gas usage data from residential, commercial, industrial, vehicle, and power plant sectors in the SOCAB. The residential, commercial and industrial data are available publicly on Southern California Gas Company (SoCalGas) database (SoCalGas, 2018). Power plant data are provided by the California Energy Commission (CEC) online database (CEC, 2018). An example for the residential sector is shown in **Figure 3.1(a)**. The time series of the natural gas consumption for the three important sectors are shown in **Figure 3.1(b)**.

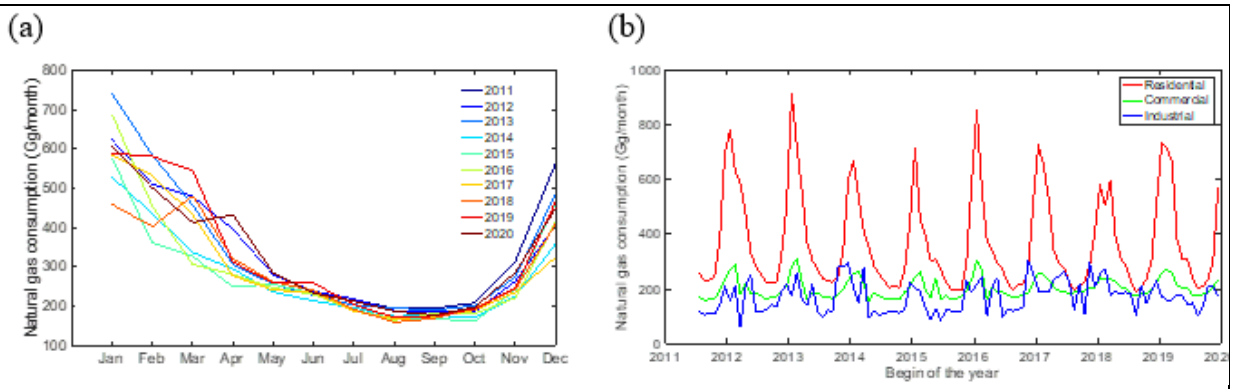

Figure 3.1

3.2.2 Monthly average surface air temperature

The monthly average surface air temperature data in Los Angeles Downtown/USC, CA (171 meters above sea level) are obtained from the stational data inventory in the NOAA/NWS Cooperative Observer Network (https://wrcc.dri.edu/cgi-bin/cliMAIN.pl?ca5115). All months from Sept. 2011 to Dec. 2020 are used. The surface air temperature in this study is the temperature of the free air conditions surrounding the station at a height between 1 and 2 meters above ground level. The air should be freely exposed to sunlight and wind. It is not close to or shielded by trees, buildings, or other obstructions. The temperature data from the observatory are averaged for every 15 seconds, and then averaged to the daily and monthly data.

3.3 Results of CH_4 emissions

Figure 3.2 shows the time series and seasonal cycles of monthly excess ratio of $XCH_{4,xs}/XCO_{2,xs}$ from 2011 to 2020 averaged over all surface reflection targets in LA basin. The excess time series shows a small decreasing trend (slope=0.016/year). However, this trend is not significant (p-value from linear regression is 0.67). **Figure 3.2(b)** clearly shows the seasonal cycle of excess ratio. Winter seasons have significantly larger excess ratio than summer seasons, indicating larger CH_4 emissions in winter relative to CO_2 emissions. There are high values of excess ratio that are possibly associated with some known special events. The spike in emissions in November, 2015 coincides with the period of maximum emissions from a very large natural gas storage well blowout at Aliso Canyon that impacted the entire LA basin (Conley et al., 2016).

The peak blowout of Aliso Canyon methane leakage occurred in November 2015. If we compare the November methane emissions for different years, we can clearly see the emission spike in November 2015, which agrees with the blowout time of Aliso Canyon methane leakage. One of the assumptions underlying in the methane emission derivation is that the 33 discrete surface target sites are sufficient to represent the average $\frac{XCH_{4xs}}{XCO_{2xs}}$ over SOCAB. During the Aliso Canyon blowout period, the enhancement of $\frac{XCH_{4xs}}{XCO_{2xs}}$ varies among different target sites, depending on the distance with the Aliso Canyon, as well as the wind speed and direction. The spike in March 2019 is likely associated with the excessively high usage of natural gas in the same month, as shown **Figure 3.1**.

The year 2020 has seen large reduction in traffic emissions, a large contributor to CO_2 emissions in LA, due to the lockdown measures because of COVID-19 pandemic. As a result, the excess ratio from March to July in 2020 is higher than previous years mainly due to the reduced CO_2 emissions.

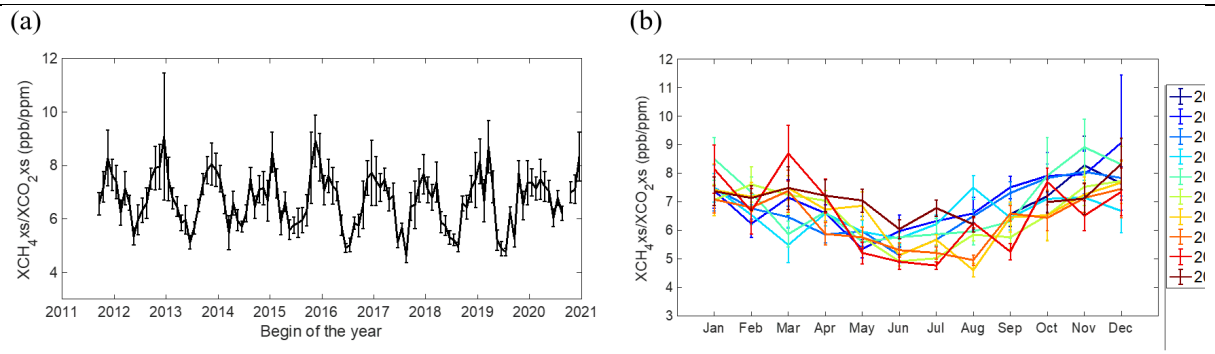

Figure 3.2 (a) Excess ratio of $XCH_{4,xs}/XCO_{2,xs}$ from 2011 to 2020 averaged over all surface reflection targets; (b) Comparison of seasonal cycles of the excess ratio of $XCH_{4,xs}/XCO_{2,xs}$. The uncertainty is calculated as the standard error of the observations for each month.

Figure 3.3 shows the monthly CH_4 emissions in the LA basin from Sept. 2011-Dec. 2019 along with the monthly average for the observing period overlaid year-by-year. Los Angeles CH_4 emissions exhibit a consistent seasonal pattern, ranging from a minimum of ~20 Gg/month in June-July to a maximum of ~40 Gg/month in December-January. We define the observed difference between measured winter and summer CH_4 emissions as the "seasonal excess" to distinguish it from the annual excess emissions defined above. **Figure 3.3(a)** shows the data represented as a continuous time series, illustrating the prominent winter emissions maxima. From the linear regression, we can also see that the CH4 emissions in LA has a near-significant reduction for the past 9-year, with an averaged decreasing rate of 0.325 Gg/month.

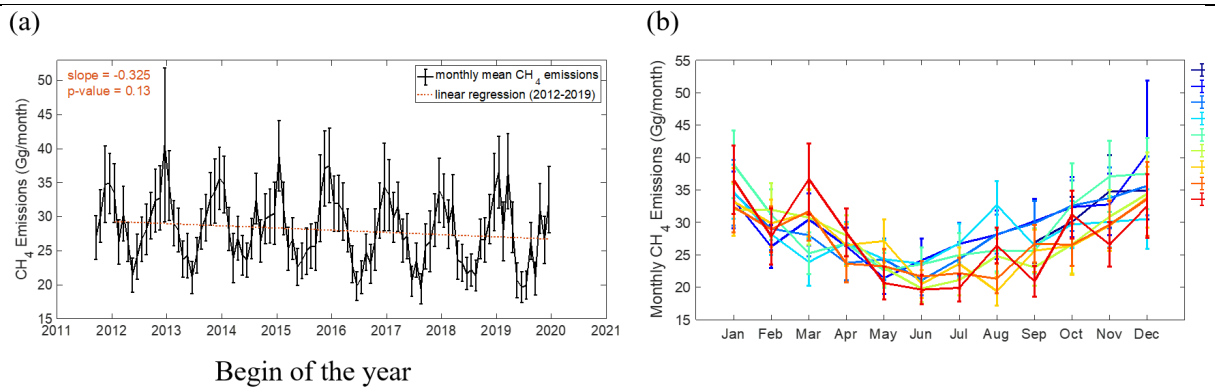

Figure 3.3 (a) Monthly CH_4 emission estimates from September 2011 to December 2019. A linear regression is applied to data from 2012 to 2019. The regressed line with associated slope and p-value are also shown. The uncertainty is calculated as the standard error of the observations for each month.

As discussed above, multiple previous studies have identified fugitive emissions from natural gas infrastructure as a likely contributor to the observed SOCAB annual excess CH_4 emissions. **Figure 3.4** compares our CH_4 emissions data and monthly natural gas consumption in the SOCAB from the residential, commercial and industrial sectors as provided by the utility company (see **Section**

3.2). The natural gas consumption data are based on metered customer usage. While the usage data do not include contributions from transmission line leaks, compressor stations, blowdowns, flaring events and other sources upstream of customer meters, these sources may correlate with metered usage. **Figure 3.4** shows that the observed Dec-Jan peaks in monthly CH_4 emissions closely track natural gas consumption.

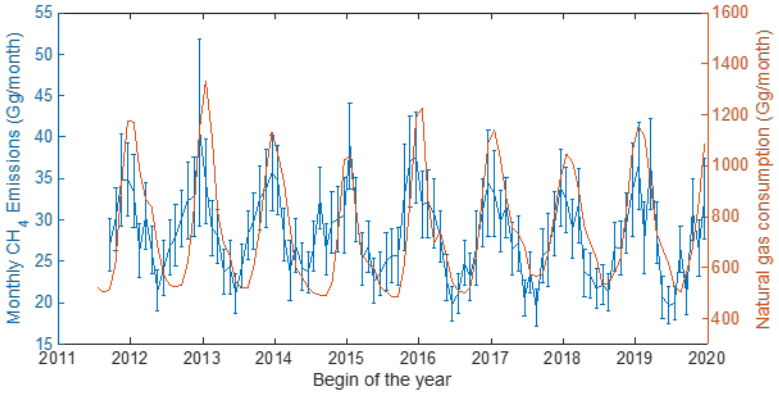

Figure 3.4. SOCAB CH_4 emissions expressed as a continuous time series (left axis). Monthly natural gas consumption data in the LA basin from the residential, commercial and industrial sectors (right axis). The natural gas consumption from the power plant sector does not show significant seasonal variability (**He et al., 2019**) and is not included here. The correlation coefficient between the two time series is 0.70. The natural gas consumption time series has been shifted to the left by a half-month. This temporal shift may be explained by the time difference in consumption and record from meters. The temporal shift can also been verified from the correlation between natural gas usage and air temperature. Shifting the natural gas usage by the same half-month results in the largest correlation coefficients.

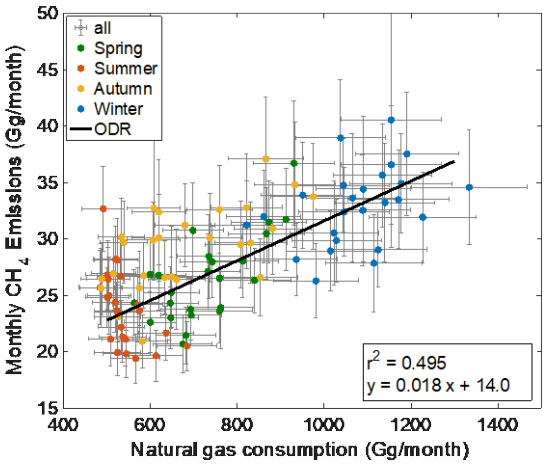

Figure 3.5. Correlation between derived monthly CLARS methane emissions and monthly total natural gas distribution to consumers in SOCAB from September 2011 to August 2017. Points are color-coded by season illustrating the progressive increase in emissions from summer (red) to winter (blue). A linear regression based on ODR, which considers the data uncertainty, is applied. The linear equation is indicated. The errors for the slope and intercept are 0.0018 and 1.289, respectively.

Figure 3.5 shows the weighted linear least squares fit between derived monthly CH_4 emissions and utility natural gas consumption in the SOCAB. The black line is the linear regression weighted

by the uncertainties in the derived CH_4 emissions and uncertainties in the consumption data are assumed to be ± 10%. The regression slope is 0.0180 ± 0.0018 and the y-intercept is 14.0 ± 1.3 Gg/month with $R^2 = 0.50$. We interpret the slope as the fraction of the post-meter natural gas consumption emitted into the atmosphere while the y-intercept gives the CH_4 emissions extrapolated to zero metered consumption, i.e. associated with non-metered emissions. The latter would include emissions from landfills, wastewater treatment, local geological sources, natural gas transmission lines and mains, etc. These sources may have their own seasonality that this simple 2-parameter model cannot capture. The fraction of emissions to consumption derived here, (1.8 ± 0.18)% is somewhat smaller than the range 2.5-6% estimated previously (Wennberg et al., 2012).

The correlation between utility natural gas consumption and CH_4 emissions may be due to increased wintertime demand by appliances for space heating, water heating, cooking, and other purposes that involve heat generation. To gain further insight into the source sectors responsible for this correlation, we use data on natural gas consumption classified by end use in California from the local utility, SoCalGas, and the California Energy Commission. Monthly data are available for five sectors: residential, commercial, industrial, vehicle fuel and electric power. Residential and commercial consumption both peak in the winter months, industrial consumption shows small peaks in the summer while electric power consumption peaks strongly in the late summer (August-September). Consumption by the transportation sector is only a few percent of the total and is not considered. Peaks in industrial consumption are less pronounced and out of phase with residential/commercial usage. A multivariate correlation analysis shows that U.S. Energy Information Administration data for natural gas consumption from the sum of the residential and commercial sectors correlates well (correlation coefficient, $R^2 = 0.88$) while the correlations between industrial consumption and residential/commercial consumption are less evident ($R^2 = 0.19$ and 0.27, respectively).

To quantify the sectoral contributions, the regression equation is given by,

$$E_{CH4}\Big|_{monthly}^{top-down} = a_0 + a_1\left(NG\Big|_{monthly}^{residential} + NG\Big|_{monthly}^{commercial}\right) + a_2 \times NG\Big|_{monthly}^{industrial} \quad (6)$$

where:

E_{CH4} = total monthly excess CH_4 emissions inferred from CLARS data (Gg)

NG_i = reported monthly sectoral natural gas consumption (Gg)

a_i = regression coefficients

The best-fit regression coefficients are 27.03, 0.029 and -0.0048 for a_0, a_1 and a_2, respectively. 45.6% of the variance between the model and observations is explained by the sum of residential and commercial consumption, and 7.7% is explained by industrial consumption. The results from the regression modeling indicate that there is a strong connection between CH_4 emissions into the atmosphere and residential/commercial natural gas consumption based on time series analysis of both data sets. Taking a_0 as the background excess methane emission in the LA basin, we see that the seasonal component results in a doubling of the total emissions relative to the background. Note that the pattern of emissions must have a seasonal component in order to explain the observations. Quiescent emissions (persistent leaks) from equipment and plumbing cannot explain the strong seasonal signal.

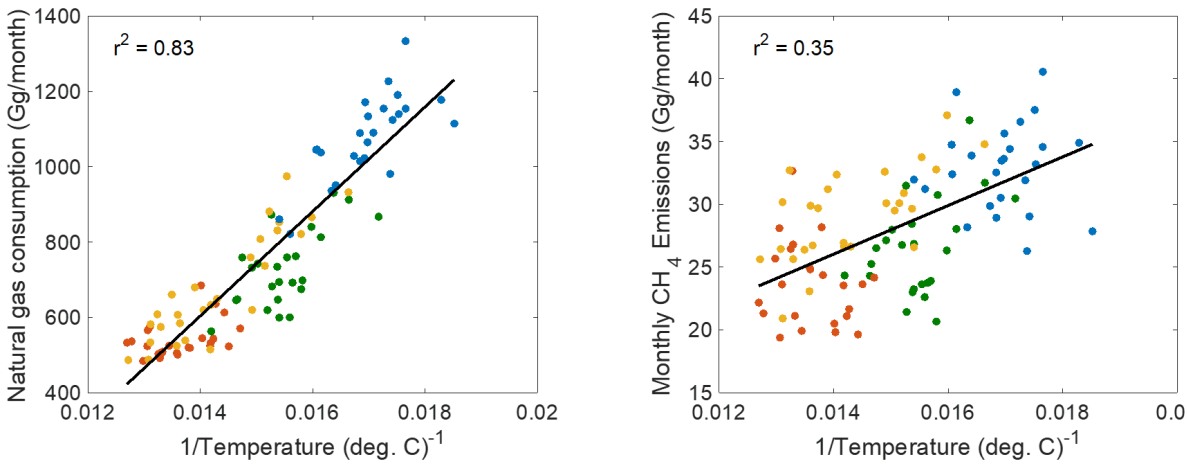

Figure 3.6. Left: The correlation between monthly natural gas consumption and inverse monthly mean temperature at USC/LA Downtown. Right: The correlation between CLARS inferred monthly CH_4 emissions and inverse monthly mean temperature at USC/LA Downtown. Increased natural gas consumption for space and water heating at lower ambient temperatures may provide the link to higher observed CH_4 emissions.

There have been few long-term studies in the SOCAB of CH_4 emissions from the most important sources (natural gas infrastructure, post-meter equipment, landfills, and wastewater treatment plants), providing weak evidence for seasonal variability from these sources (Wong et al., 2016). Only post-meter consumption mimics the observed CH_4 emissions pattern (Wong et al., 2016). **Figure 3.6** shows clear correlations between the inverse of the ambient temperature measured near downtown Los Angeles and both natural gas consumption and CH_4 emission rates. Reduced surface air temperatures drive air and water heating demands, resulting in the expected increase in observed CH_4 emissions with decreasing surface temperature (see **Section 3.2**). These observations reinforce the connections between ambient temperature, heating demand and fugitive natural gas emissions. **Figure 3.6** also provides some insight for considering the temperature as an important variable linking natural gas consumptions and CH_4 emissions.

3.2 Discussions of CH_4 emissions

Since there are no national air quality standards for methane, very little work has been done to characterize the methane emission factors from natural gas-fired appliances such as furnaces, water heaters, stoves, ovens, swimming pool and spa heaters and similar equipment. Currently, the only available emission factor for CH_4 from natural gas-fired furnaces is 5 g/GJ for both commercial and residential furnaces (U.S. Environmental Protection Agency, 2018). From **Figure 3.4**, SOCAB winter natural gas consumption surpasses 1000 Gg/month. Using the EPA emission factor, this would result in about 0.29 Gg/month seasonal excess methane emissions, which is far less than the observed value of ~20 Gg/month.

There are a number of factors that may close the gap between top-down and bottom-up estimates of seasonal excess methane emissions. Far more research needs to be conducted on emission factors from gas-fired appliances and industrial combustors under different operating conditions (start-up, operation, shut-down). While increased demand for space heating is clearly associated with lower ambient temperatures in the winter, water heating demand also increases because of

decreases in supply water temperature. For example, in the mild, Mediterranean climate of Pasadena, California, measurements from 2001-2016 at six locations showed an average difference of 12 °C in supply water temperature from winter to summer (Kimbrough, 2017). Significantly larger seasonal temperature variability would be expected in colder climates. There is increasing evidence that the probability density functions for CH_4 emissions have a long tail, characterized by a small number of emitters with very large emissions, perhaps due to malfunctioning equipment or improper operating conditions (Zavala-Araiza et al., 2015). This will require a concerted measurement campaign examining large numbers of emitters (thousands) under actual operating conditions targeting residential, commercial and industrial sectors (Fischer et al., 2018).

3.3 Section conclusions

In conclusion, using mountaintop remote sensing with coverage over the greater Los Angeles basin, we observe seasonal excess methane emissions that correlate very well (R^2=0.50) with combined commercial and residential natural gas consumption. From the covariance we observe that the emissions arise from two terms: one that is seasonally invariant (14.0 ± 1.3 Gg/month) and another that peaks in the colder months of the year corresponding to (1.8 ± 0.18) % of residential plus commercial natural gas consumption. Other natural gas consumption sectors (industrial, power plant and transportation) either have no clear seasonal relationship that matches the observed emissions or are too small. The available emission factor data for residential and commercial natural gas-fired combustion sources fail to explain the observed emissions. Indeed, far more work needs to be done to measure the seasonally varying probability distribution functions of emitters under actual operating conditions.

Chapter 4. Long term trend of N_2O emissions in LA

4.1 Temporal Variability in XN_2O Excess

Time series using data from all reflection locations illustrate significant temporal variability in XN_2O_{xs} in the LA basin. The plot of monthly averages of XN_2O_{xs} (**Figure 4.1**) illustrates that CLARS consistently observed seasonal fluctuations in XN_2O_{xs} during 2013 to 2019. The weighted mean value of XN_2O_{xs} for the entire basin during this time period is 15.0 $\pm$ 0.1 ppb, and the mean uncertainty for excess values is 13.8 ppb.

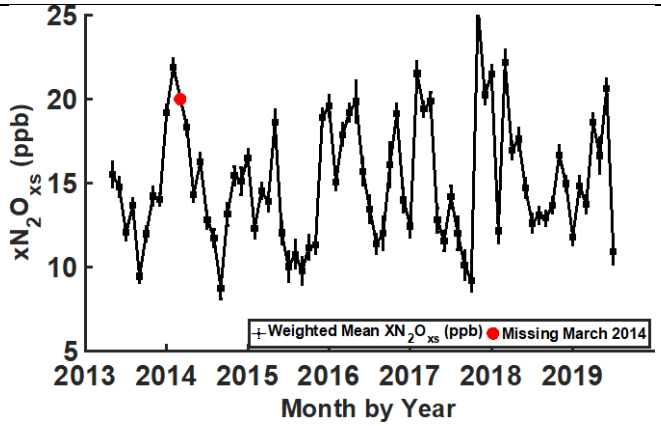

Figure 4.1 Monthly mean XN_2O_{xs} from 2013 to 2019 shown in black with the uncertainty given by the grey area. March 2014 is removed from the plot due to an instrumental issue which resulted in only 3 days of data collection.

Comparing interannual monthly means yields further insight into the observed seasonal cycle of XN_2O excess. **Figure 4.2** shows the monthly weighted mean plotted versus month for each year from 2013-2018. The black line indicates the weighted mean calculated for each month using all years of data. For most years, peak excess values were observed in the winter or spring months with clear minima occurring around late summer/ early fall. Similarly, the smallest interannual variability in monthly means occurs during months with smaller excess values, while greater variability from year to year is observed in winter and spring.

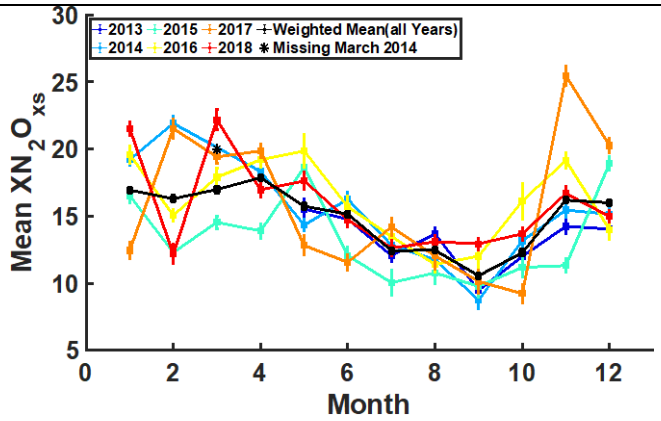

Figure 4.2 The plot of basin-wide weighted mean XN_2O_{xs} vs month for years 2013-2018. The black line gives the monthly weighted mean for all years of data.

To further analyze this time series, a basin-averaged XN_2O_{xs} value is calculated for each day of the year for years 2013-2019 using a weighted averaged of available surface reflections point values on the given day. Performing PCR on the set of daily basin-averaged XN_2O_{xs} values, no significant linear interannual trend is observed in XN_2O_{xs} from 2013 to 2019 for SoCAB. Summing the seasonal terms from the PCR results yields a seasonal cycle with a peak-to-peak amplitude of 5.6 ± 2.5 ppb where minima occur in August and maxima occur in early February. These results are visually consistent with **Figure 4.2**.

4.2 Mapping $XN_2Oxs/XCO_{2,xs}$ Excess Ratios

Maps of the $XN_2O_{xs}/XCO_{2,xs}$ excess ratios according to surface reflection point location also show significant spatial variability across the LA basin (**Figure 4.3**). These $XN_2O_{xs}/XCO_{2,xs}$ values lie in the range 0.80 – 1.50 with uncertainties on the order of about 0.05 (see Supplementary Table 2 for exact values).

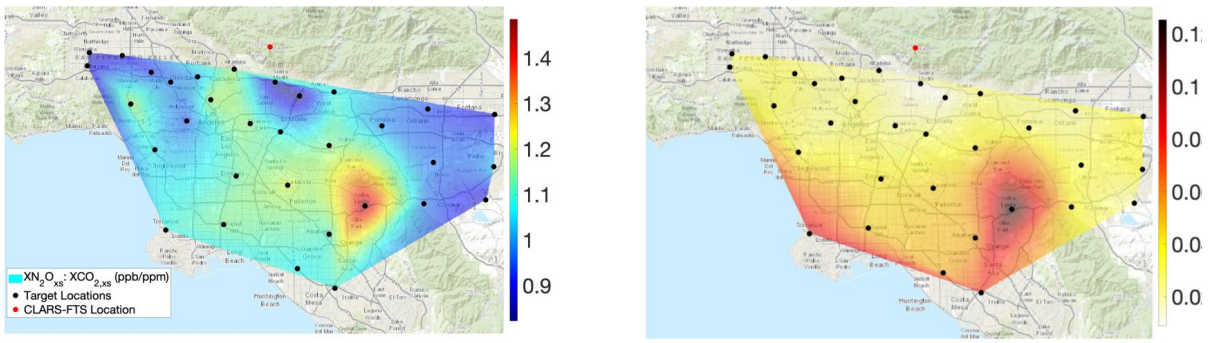

Figure 4.3 (a) Map of $XN_2O_{xs}/XCO_{2,xs}$ excess ratios (ppb/ppm) by surface refection point location for 2013-2019; (b) Associated map of uncertainties in $XN_2O_{xs}/XCO_{2,xs}$ excess ratios (ppb/ppm) determined from error propagation.

Figure 4.3(a) indicates greater $XN_2O_{xs}/XCO_{2,xs}$ values in the central section of SoCAB, with a particularly large ratio associated with surface reflection point located in Orange county (see **Figure 2.1**). The region of the map corresponding to ratio values > 1.1 tends to be more densely populated and additionally houses a number of wastewater treatment plants. **Figure 4.3(b)** shows the associated uncertainty map for reference. Larger uncertainty values are observed for targets farther from CLARS (indicated by the red dot) due to higher retrieval uncertainties for greater slant distances through the PBL.

4.3 Bottom-up N_2O emissions estimate for LA Basin

Figure 4.4 illustrates the seasonal time series of top-down N_2O emissions for SoCAB during 2013-2018. Like **Figure 4.1** for XN_2O_{xs}, **Figure 4.4** indicates seasonal variability in emissions with most monthly emission values falling in the range of 8-14 Gg N_2O per month. Applying principal component regression to the monthly emission values, no statistically significant interannual trend is observed for top-down emissions. Uncertainty in these seasonal estimates shown in grey is

determined considering uncertainty in the basin-averaged $XN_2O_{xs}/XCO_{2,xs}$ excess ratio and the uncertainty in the HESTIA-LA bottom-up CO_2 emission inventory, which is estimated to be about 10% (Gurney et al., 2019).

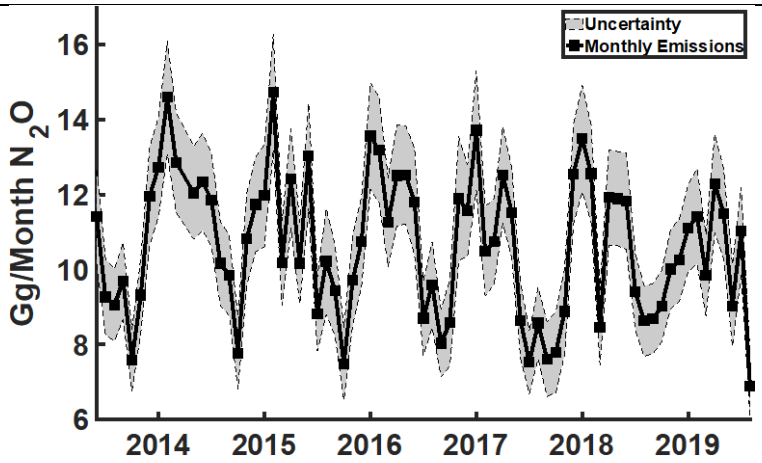

Figure 4.4 Top-down seasonal N_2O emissions for LA Basin from 2013 to 2018. Uncertainty shown in grey is quantified considering uncertainty in the basin-averaged $XN_2O_{xs}/XCO_{2,xs}$ value for a given month and year and uncertainty in the HESTIA-LA bottom-up CO_2 inventory, estimated at 10% of the CO_2 emissions value.

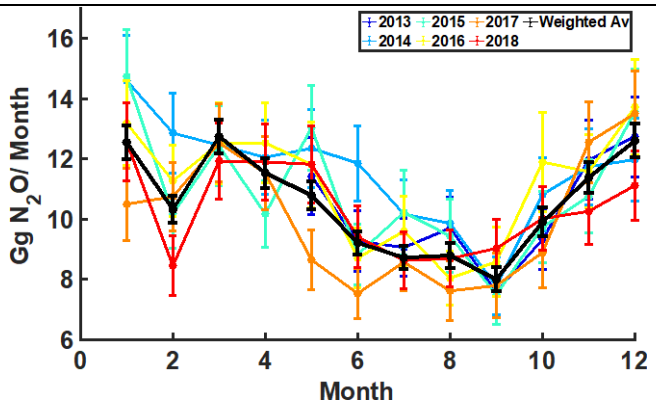

Figure 4.5. Top-down monthly emissions versus month for each year from 2013 to 2018. The black line indicates the weighted average of monthly emissions for all years of data. The uncertainty in each monthly emission estimate is shown with error bars.

Figure 4.5 further examines the seasonal cycle in emissions by illustrating both the interannual variability and the consistent monthly trend derived from all years of data. In **Figure 4.5**, monthly emissions are plotted versus month for each year from 2013 to 2018. The black line indicates the weighted average of monthly emissions for all years of data. The uncertainty in monthly emissions estimate and in the weighted average are shown with error bars. Monthly emissions follow a similar temporal pattern to the XN_2O_{xs} (**Figure 4.2**), where minima tend to occur during the late summer and early fall. Larger monthly emissions values correspond to winter and spring months. For all years, we see a general declining trend starting from January through the start of the fall, which generally includes a clear dip in monthly emissions during the month of February. In a manner similar to XN_2O_{xs} (**Figure 4.2**), months associated with greater monthly emissions also

exhibit higher degrees of interannual variability, whereas fall emissions, which tend to be smaller, are also less variable from year to year.

Monthly emissions in **Figures 4.4 and 4.5** can be aggregated to estimate annual N_2O emissions for SoCAB for the years 2013-2018. Exact values of annual emissions along with associated uncertainties are listed in **Table 4.1**. **Figure 4.6** shows the annual time series of N_2O emissions derived from CLARS-FTS observations in dark blue, in comparison with other N_2O emissions estimates for greater LA (SoCAB) and for California (statewide). The emissions estimates referring only to SoCAB are distinguished by square markers and light or dark blue color. The light blue square represents a 2007 emission estimate reported by Wunch et al. (2009), which employed a similar tracer-tracer correlation method using TCCON measurements of N_2O and CO_2. The star markers represent to statewide N_2O emissions estimates with the red line referring to the California Air Resource Board (CARB) bottom-up inventory from 2006 to 2017 (California Environmental Protection Agency Air Resources Board, 2019b), and the pink line indicating a statewide N_2O emissions estimate from CalNex flights made in 2010 (Xiang et al., 2013).

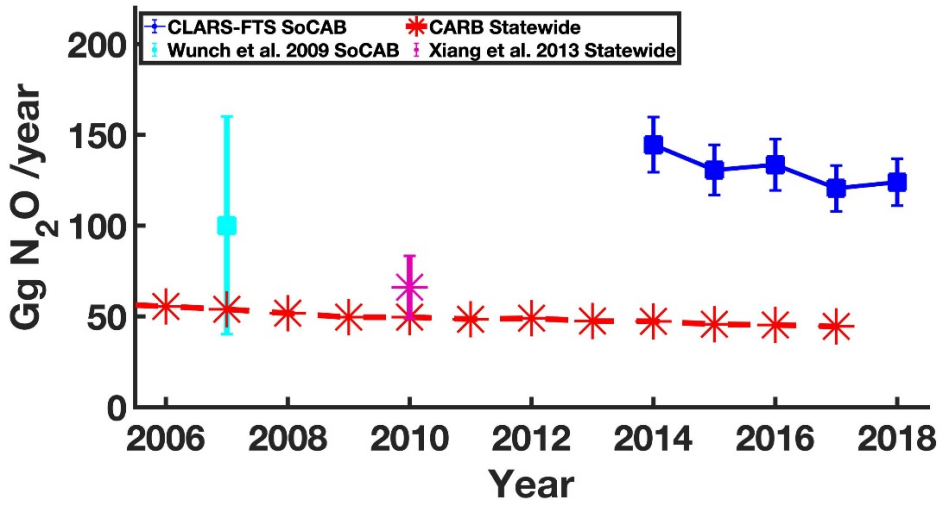

Figure 4.6. CLARS-FTS annual top-down N_2O emissions for SoCAB as compared with another top-down SoCAB N_2O emissions estimate for 2007 (Wunch et al., 2009), shown in light blue, and two estimates of statewide N_2O emissions. The CARB statewide bottom-up inventory is shown in red (CARB, 2019b), and a statewide estimate from the CalNex aircraft campaign in 2010 is shown in pink (Xiang et al., 2013).

Table 4.1 Annual N_2O Emissions calculated for 2014-2018 (Gg/y)

	Annual	Uncertainty
2014	144	5
2015	131	4
2016	133	4
2017	120	4
2018	124	4

Applying a linear regression to annual emissions estimates gives a $p > 0.05$, and therefore a statistically significant interannual decrease is not observed from the top-down basin emissions estimates. **Figure 4.6** illustrates that the CLARS estimate of annual emissions is larger than even statewide N_2O emission estimates, although CLARS annual emissions are consistent within uncertainties with the Xiang et al. (2013) statewide estimate along with the Wunch et al. (2009) SoCAB estimate. The discrepancy between the CLARS SoCAB N_2O emissions estimate and the CARB statewide inventory aligns with other studies reporting discrepancies between bottom-up and top-down emissions values for various GHGs (Montzka et al., 2011), a fact that highlights the importance of comparing results from the two methods.

4.4 Discussion on N_2O emissions

4.1.1 Impacts of aerosol scattering on the tracer-tracer excess ratio

The light scattering effect due to aerosols changes the light path and therefore affects the GHG retrievals from CLARS-FTS (Zhang et al., 2015; Zeng et al., 2020). The tracer-tracer ratio method used to calculate $XN_2O_{xs}/XCO_{2,xs}$ cancels out the aerosol scattering effect to first order. Here we further examine its impact under different aerosol abundances by using different filter criteria for the observed O_2 ratios. **Figure 4.7** shows the time series of the basin-averaged $XN_2O_{xs}/XCO_{2,xs}$ excess ratio calculated using three different filter criteria for O_2 ratios (Geometric O_2 SCD: Retrieved O_2 SCD) when filtering the LABS data set. The blue line indicates filter criteria applied for analysis in this study, while the green and red represent increasingly narrow filter limits respectively.

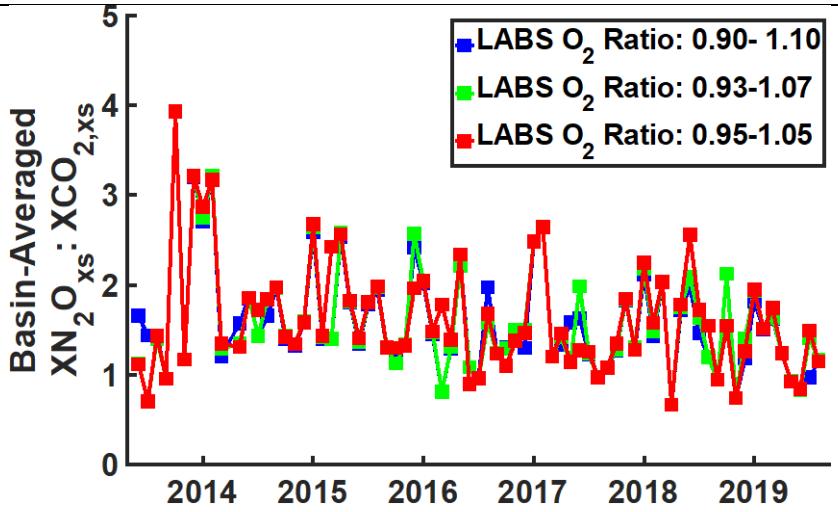

Figure 4.7. Time series of basin-averaged $XN_2O_{xs}/XCO_{2,xs}$ excess ratio for various O_2 ratio (Geometric O_2 SCD: Retrieved O_2 SCD) filter criteria applied to LABS data set.

By imposing narrower filter limits, larger amounts of data affected by aerosol and cloud scattering are excluded from analysis, and the data set is restricted to increasingly clear observations. However evident from **Figure 4.7**, narrowing filter limits does not have a significant effect on the basin-wide weighted average $XN_2O_{xs}/XCO_{2,xs}$ values. While XN_2O and XCO_2 are retrieved in different spectral windows, the dependence of aerosol scattering on wavelength does not result in a bias in the excess ratio of the two GHGs. Thus, it is reasonable to assume that the effect of aerosol

scattering on the $XN_2O_{xs}/XCO_{2,xs}$ excess ratio values is negligible. By extension, we can conclude that the effect of aerosol scattering on top-down N_2O emissions results, derived by applying the tracer-tracer correlation method, is also negligible.

4.4.2 Comparison of XN_2O results with previous studies

CLARS-FTS LABS retrievals of XN_2O includes values which are generally larger than boundary layer XN_2O measurements reported by previous studies. For example, Wunch et al. (2009), who also used ground-based remote sensing to measure GHG concentrations in the LA basin, provide daily XN_2O retrievals for 5 days of measurements within the range of ~290-300 ppb, and estimate XN_2O anomalies on the order of 20 ppb. In another study of urban XN_2O, Byrne et al. (2020) report open path Fourier Transform Infrared (OP-FTIR) measurements of XN_2O in the boundary layer over downtown Toronto as ranging between 327-338 ppb. From a survey of global NDACC and TCCON sites, Zhou et al. (2019) report similar magnitudes for XN_2O retrievals ranging from 290-340 ppb for various locations.

In contrast, it is clear from the time series in **Figure 2.3** that the set of CLARS-FTS LABS retrievals from all surface reflection point locations during the period 2013-2019 exhibits a greater degree of variability compared to these previous studies and includes some observations of $XN_2O >$ 340 ppb. However examining the distributions of LABS retrievals for two specific surface reflection point locations indicates that the majority of XN_2O retrievals lie below the threshold of 340 ppb, an observation that is somewhat obscured by the time series.

In general, larger XN_2O values are associated with larger slant distances in the basin and correspondingly larger retrieval uncertainty values. The effect of these data on subsequent analysis is minimized through the application of averaging methods which weight data according to associated uncertainties. For example, examining the excess XN_2O values inferred from CLARS-FTS LABS observations, we see that while some data are significantly larger than 20 ppb, the weighted mean of all XN_2O_{xs} observations is 15.0 ± 0.1 ppb. Therefore, the weighted mean is comparable to anomaly values reported in Wunch et al., (2009). As an extension given that multiple averaging methods are applied in order to estimate the top-down N_2O emissions for the LA basin, larger retrieval values with greater associated uncertainties have a negligible effect on the final result.

Furthermore, certain large retrieval values which do not have large associated uncertainties may represent true signal, as the CLARS-FTS data record for all GHGs generally exhibits a high degree of variability, both spatially and temporally, within SoCAB. This can be understood in part due to the unique qualities of the CLARS-FTS viewing geometry in LABS mode, which makes it highly sensitive to GHG concentrations within the PBL. In particular, CLARS-FTS retrievals are more heavily weighted toward the boundary layer compared to TCCON and NDACC total column measurements (Wunch et al., 2009; Zhou et al., 2020), which are comparatively more sensitive to the atmosphere above the PBL. Given that the concentration of N_2O in the upper atmosphere is smaller than its background levels in the lower troposphere, it is reasonable that total column retrievals would be smaller than CLARS-FTS retrievals, even for a similar location. In addition, through its method of spatial scanning, CLARS-FTS can make observations for a large area, while total column measurements are primarily representative of conditions in close proximity to the instrument location. The spatial coverage of the CLARS-FTS measurement capability represents an additional source of variability within the data.

Finally, the methodology for removing low-quality retrievals prior to analysis enhances the robustness in reported retrieval results. Specifically, the quality of CLARS-FTS retrievals is verified by the application of several data filters, one of which targets the root-mean-squared (RMS) residuals due to spectral fitting. Observations with RMS spectral residuals greater than one standard deviation from the mean are removed. As a result, RMS residual values are less than 1.5% for all GHG observations, and a large majority of observations have RMS values less than 1%. Observations with retrieval uncertainties more than three standard deviations above the mean are also filtered out. The relatively small RMS values from spectral fitting and the low retrieval uncertainty values of the filtered data provides additional confidence in the CLARS-FTS retrieval results.

4.4.3 Trends in XN_2O in the free troposphere

CLARS-FTS observations of free tropospheric N_2O mixing ratios yield an interannual increase of 0.95 ± 0.04 ppb/year. This result is highly consistent with recent studies quantifying the interannual increase in background XN_2O over the past decade (Zhou et al., 2019). From CLARS-FTS SVO observations, we also observe a seasonal cycle, which has a minimum occurring in April and a maximum occurring in late October with a peak-to-peak seasonal amplitude of 4.3 ± 0.4 ppb. This result agrees with other reports of a seasonal cycle in tropospheric N_2O with a minimum in late spring/ early summer. This seasonal minimum has been previously attributed to an influx of N_2O-poor air from the stratosphere (e.g., Liao et al., 2004; Nevison et al., 2004; Jiang et al., 2007). Furthermore, the peak-to-peak amplitude for the seasonal cycle observed by CLARS-FTS is comparable in magnitude to seasonal amplitudes observed by TCCON and NDACC stations in the Northern hemisphere (Zhou et al., 2019).

4.4.4 Trends in XN_2O Excess in the LA Basin

CLARS-FTS observations of XN_2O_{xs} exhibit a seasonal cycle which has a minimum in late summer/early fall and a maximum in winter/ early spring with a peak-to-peak amplitude of 5.6 ± 2.5 ppb. One hypothesis for this observed seasonal cycle in XN_2O_{xs} could relate to precipitation trends for Southern California. Previous work has shown that greater soil moisture can increase N_2O fluxes from fertilized soils depending on soil type and temperature (e.g. Avrahami and Bohannan, 2009; Butterbach-Bahl et al., 2013, Horwath, 2012). In LA, the summer/early fall is usually a period of extended drought and could correspond with conditions of low soil moisture. Similarly, the greater interannual variability in monthly means during winter/spring months could also relate to rainfall patterns since although winter/spring months are generally wetter months in LA compared to the summer, seasonal precipitation varies widely from year to year. Another explanation for the spring maximum relates to fertilization patterns in Los Angeles. Townsend-Small et al. (2011) reports that fertilization rates for urban landscapes in Los Angeles are equal or greater than that for agricultural fields, with comparable N_2O emission factors. Given that rapid increases in N_2O fluxes are observed directly following fertilization (e.g. Townsend-Small et al., 2011), application of fertilizer to urban lawns in spring months could correlate to overall increase in XN_2O_{xs} in this season.

4.4.5 Top-Down N_2O Emissions from CLARS-FTS observations

Monthly N_2O emissions derived from CLARS-FTS observations for SoCAB range from 6-19 Gg N_2O per month during the years 2013 to 2018. Examining monthly emissions for each year along with the weighted average of monthly emissions from all years of observation, we observe a seasonal cycle similar to that of XN_2O_{xs}, where minima occur during late summer/ early fall and

annual maxima tend to occur in the winter. We similarly observe slightly less interannual variability during the fall months when the estimated monthly emissions are smallest. It is not clear from these results how various source sectors, whose seasonal cycles likely differ in phase and amplitude, impact the overall seasonal cycle observed by CLARS-FTS. For example, another source of N_2O emissions which is likely an important factor in overall emissions from SoCAB is coastal upwelling. Townsend-Small et al. 2014 found that coastal waters were a positive source of N_2O, and positive fluxes from the ocean surface would likely be largest during the summer when upwelling is the strongest. However, this seasonal signal is not necessarily apparent in the basin-wide emission results. Overall, more work is needed disentangle the relative contributions from various source sectors in order to better analyze the seasonality of N_2O emissions within the SoCAB basin.

The derived annual N_2O emissions for SoCAB from 2014 to 2018 range between 124 – 144 Gg N_2O per year. These annual emission estimates are significantly larger the CARB statewide bottom-up inventory for N_2O, which reports a mean annual N_2O emission of about 46 Gg per year for the same time period. Other studies have reported similar discrepancies between top-down and bottom-up estimates. For example, Xiang et al. (2013) suggested that bottom-up N_2O inventories could be significantly underestimating annual emissions for California. Using data from CalNex flights conducted in 2010, Xiang et al. (2013) estimated statewide annual emissions at 132 ± 35 Gg N_2O for that year, which is roughly 2 times larger than the respective annual emission estimate from the CARB inventory.

Very few estimates of N_2O emissions on a citywide scale have been reported, and only one other estimate of N_2O emission has been made for SoCAB specifically (Wunch et al., 2009). Wunch et al. (2009) employed a tracer-tracer correlation method, similar to that used in this study and reported a XN_2O/ XCO_2 anomaly ratio value of 0.5 ± 0.3. This anomaly ratio yielded an annual emission estimate for 2007 of 100 ± 60 Gg N_2O. This anomaly ratio value is slightly smaller than $XN_2O_{xs}/XCO_{2,xs}$ excess ratios observed by CLARS-FTS. For example the mean excess ratio for the West Pasadena location, which is the closest surface reflection point to the TCCON tower used in Wunch et al. 2009, is 1.16 ± 0.02 for 2013 to 2019. Similarly, the SoCAB emission estimate from Wunch et al. (2009) is slightly smaller than that derived from CLARS-FTS observations, but the two values agree within their uncertainties.

4.4.6 Relative importance of N_2O sources in urban setting

CLARS-FTS observations clearly indicate significant enhancements of XN_2O above background levels in the PBL. These emissions largely originate within the Los Angeles megacity, which is home to approximately 40% of the state's population. The observation of urban XN_2O_{xs} highlights the importance of urban N_2O sources in contributing to cumulative statewide emissions. Yet most statewide and national estimates prioritize quantifying rural emissions derived from agriculture. For this reason, it is difficult to justify estimating citywide emissions by downscaling statewide N_2O inventories using proportional populations. Rather, quantifying the overall N_2O emissions in an urban setting requires an understanding of both the N_2O source sectors and their variabilities. The following discussion contains an assessment of the relative importance of urban N_2O emission sources based on information contained in the California's 2000-2014 Greenhouse Gas Emissions Inventory Technical Support Document (CARB, 2016), which outlines the methodology used in calculating their bottom-up N_2O emissions inventory for California.

A major source of anthropogenic N_2O emissions worldwide is combustion from fossil fuels (Montzka et al., 2011). According to the CARB inventory, N_2O emissions from fuel combustion fall under the category of Energy and comprise about 27% of the total N_2O emissions inventory for 2017, making it the second largest contributor to statewide emissions after agriculture, forestry, and other land use (CARB, 2019a). Of activities within the category of fuel combustion, transportation contributes more emissions than any other activity. 24% of all N_2O emissions in the CARB 2017 statewide inventory are derived from aviation, on-road transportation, railways, and water-borne navigation (CARB, 2019a). Top-down studies on N_2O, which quantify relative contributions from various economic sectors, have also highlighted the importance of transportation in statewide emissions (Xiang et al., 2013). Given that LA has a high traffic density and is a large transportation hub for aviation and overseas shipping, N_2O emissions from transportation likely play a significant role in total urban emissions. Other sources of N_2O associated with combustion include electricity generation, heat production, and petroleum refining, all of which make up a smaller proportion of the CARB inventory but likely contribute to emissions in areas of LA adjacent to these industrial centers.

A second important source of urban N_2O emissions is derived from the fertilization of urban lawns. As previously stated, Townsend-Small et al. (2011) reported urban landscapes (lawns and athletic fields) have annual N_2O fluxes equal to or greater than agricultural fields with comparable emission factors. Though the understanding of emission factors for different soils under various conditions is continuously improving (e.g. Bouwman et al., 2002; Horwath et al., 2012; Zhiseng et al., 2020), it is difficult to aggregate emissions from urban lawns based on heterogeneity of fertilizer application practices and land cover type. For this reason, emissions from urban landscapes are often not quantified or underestimated in statewide N_2O bottom-up emissions inventories, which could partially explain some of the discrepancy between top-down and bottom-up N_2O emissions estimates for urban areas.

Other sources of urban N_2O emissions associated with microbial activity include landfills, composting organic waste, and wastewater treatment plants. The statewide CARB estimate of N_2O emissions from landfills is primarily calculated according to recorded quantities of combusted landfill gas. Therefore, N_2O emitted directly from microbial activity in the landfill is not included in this estimate. Additionally, according to CARB, industrial composting of organic waste has increased by 3 times in the last 20 years and represents a growing source of N_2O emissions (CARB, 2016). The annual CARB inventory only accounts for industrial composting in its emissions estimate, meaning backyard composting in residential areas, which is popular in Los Angeles, also represents a source of urban emissions that is currently not captured by the bottom-up estimate.

Finally, wastewater treatment plants can also serve as important sources in urban settings. The CARB inventory divides N_2O emissions from wastewater treatment plants into two categories: direct emissions and indirect emissions due to the effect of effluent on aquatic environments. N_2O emissions under various wastewater plant management practices have been consistently studied in order to determine optimal conditions to minimize direct emissions from the plant (e.g., Wunderlin et al., 2011; Daelman et al., 2015; Vasilaki et al., 2019). Generally, direct plant emissions are small compared to indirect emissions from effluent discharged into aquatic ecosystems (CARB, 2016), which are more difficult to quantify. For a highly populated coastal city, such as Los Angeles, these indirect emissions are likely significant sources to the regional N_2O budget, given the large anthropogenic effect on nearby aquatic ecosystems. Furthermore, previous research has suggested that even direct emissions may be greater in Los Angeles compared to other cities, due to the

importance of water reclamation processes in reducing dependencies on imported water resources, which can be necessary in arid environments. Surveying several wastewater treatment plants in Southern California, Townsend-Small et al. (2014) found that plants which utilize processes for nitrogen removal may lead to in-situ N_2O emission rates that are three or more times greater than traditional treatment processes, which aim for carbon oxidation only. Given that LA has a higher proportion of wastewater treatment plants that use nitrogen removal processes compared to other cities, direct emissions may play an elevated role in regional emissions compared to other urban areas.

4.5 Section conclusions

This section employed a unique data set from a mountaintop remote sensing instrument, CLARS-FTS, which has surveyed GHG mixing ratios in the LA basin since 2011, in order to examine the climatology of N_2O in this region. CLARS-FTS observations were used to investigate the temporal variability of N_2O excess mixing ratios and to calculate a top-down N_2O emissions estimate for SoCAB. No significant interannual trend is observed in $XN_2O_{xs,}$ but XN_2O_{xs} does exhibit a seasonal cycle with minima in late summer/ early fall and maxima in the early spring. A similar seasonal cycle is observed in top-down monthly emissions estimates calculated using a tracer-tracer ratio method with CO_2. The seasonal cycle could in part be related to precipitation and fertilization patterns in Los Angeles, as both soil moisture levels and fertilization practices are important factors in N_2O fluxes from urban lawns.

Top-down monthly emissions estimates range from 6-19 Gg N_2O per month, while annual emissions range from 124–144 Gg per year for the years 2014 to 2018. Annual emissions estimates are roughly 3 times larger than statewide bottom-up inventories, but consistent within uncertainties with the top-down SoCAB emission estimate for 2007 reported by Wunch et al. (2009). The discrepancy between top-down and bottom-up N_2O estimates for both California and SoCAB highlights the difficulty in constraining N_2O emissions using bottom-up methods and in quantifying urban emissions on a local level.

Extending the length of the CLARS-FTS database is essential to reducing statistical noise and enhancing future work that would utilize these unique observations to study GHG and pollutant concentrations in the LA basin. With respect to the topic of urban N_2O, more work is needed in order to clarify the relative importance of various source sectors to anthropogenic emissions. Future work could examine specific instances of anomalies in the $XN_2O_{xs}/XCO_{2,xs}$ excess ratio in order to connect these observations with emissions from special events. Another approach would be to employ N_2O isotopologes (Yoshida and Toyoda, 2000) to isolate and quantify relative contributions from different source sectors to the overall change in XN_2O over time and to the seasonal cycle in N_2O emissions. All in all, enhancing our understanding of the landscape of urban N_2O emissions is key to evaluating local measures for emission reduction.

Chapter 5. Diurnal, weekly and seasonal cycles of CO emissions in LA

5.1 Time series of XCO from CLARS-FTS observations in LA

Figure 5.1(a) shows the time series of all available XCO retrievals from CLARS. Since we focus on the CO climatology in LA, XCO outliers, which are defined as data that are more than three standard deviations away from the mean, are excluded from the XCO retrievals. Seasonal cycles with peaks in spring and troughs in summer can be clearly seen in both LABS and SVO mode observations. This cycle, well known from previous CO observations, is driven by the seasonal change of OH, the dominant sink of CO in the atmosphere (Spivakovsky et al., 2000; Canty and Minschwaner, 2002). Before spring, when OH is relatively low, CO concentration accumulates and eventually reaches its peak in early spring. In summer, the OH production reaches its peak and drives the CO concentration down. The XCO from LABS, which measures the PBL change contributed by anthropogenic emissions, is significantly higher and has larger variability than SVO values, which measure the background change above the PBL. The difference between the two, as shown in **Figure 5.1(b),** is about 55.1 ppb on average. The XCO enhancement, as shown in **Figure 5.1(c)**, is about 87.2 ppb on average, which is about 59% of the average LABS XCO measurement. Such a high enhancement of XCO in the LA megacity makes it easy to be detected and therefore makes it a good tracer of source emissions. Both the XCO difference and the enhancement show a weak seasonal cycle due to the seasonal pattern of atmospheric dynamics. In the following sections, we investigate the diurnal, weekly, and seasonal pulses of XCO enhancement and how they are associated with anthropogenic emissions and atmospheric dynamics in the LA megacity. We primarily focus on CO climatology; interannual variability will not be discussed in this paper. Measurements potentially affected by wildfire emissions, which will lead to extremely high CO concentration, have also been filtered by excluding days with large wildfires (e.g., Woolsey wildfire and Holy wildfire in 2018), filtering out observations with high fitting residuals and low O_2 ratio resulting from strong aerosol emissions during wildfires, and removing data that are more than three standard deviations away from the mean.

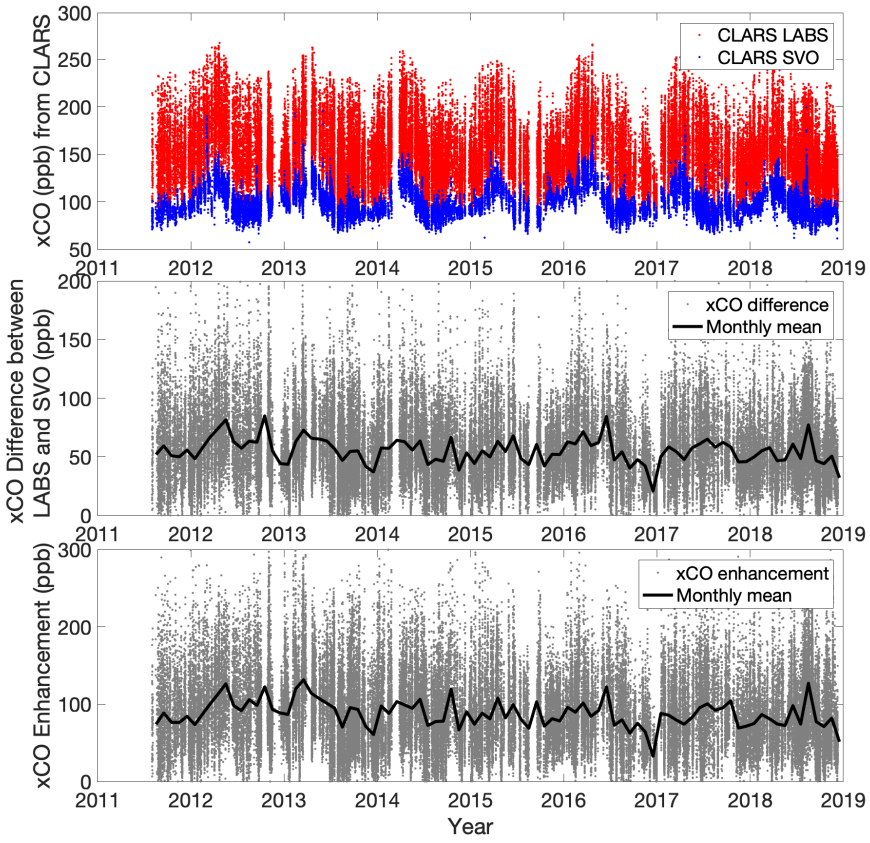

Figure 5.1. Top panel: Time series of XCO retrievals from CLARS, including both LABS and SVO observing modes. These measurements have been filtered and corrected to remove the bias due to aerosol scattering effects. Furthermore, XCO outliers, which are defined as data that are more than three standard deviations away from the mean, are excluded from the XCO retrievals; Middle panel: XCO difference between LABS and SVO modes; Bottom panel: XCO enhancement, which is the difference between PBL and background XCO, is calculated by applying the geometric correction (**Appendix A3**) to the XCO difference in the middle panel. An averaging kernel smoothing correction (**Appendix A4**) is also implemented to account for the different vertical sensitivity of the LABS and SVO modes. The monthly means of XCO difference and enhancement are also shown.

5.2. Diurnal cycles of XCO enhancement

The XCO enhancement is averaged hourly and mapped to illustrate the diurnal patterns in the LA basin from 8 am to 5 pm, as shown in **Figure 5.2**. All retrievals from 2011 to 2018 are used. Following Wong et al. (2015), natural neighbor interpolation (Sibson, 1981) is used to generate the maps using XCO enhancement from the 33 surface reflection points. The corresponding hourly mean wind fields at ~50 meters above ground from WRF-Chem simulations—which uses ECMWF ERA5 reanalysis for the initial and boundary conditions — are also shown. The results indicate three clear features: (1) The XCO enhancement is generally higher in the early morning (8–10 h) near the downtown area and the northern LA basin, when the land-sea breeze (typically land breeze in summer and sea breeze in winter) is weak. This pattern is generally consistent with bottom-up CO emission estimates in the LA basin. The east-west contrast of XCO enhancement in the early morning is about 50 ppb; (2) A strong diurnal variability in XCO enhancement can be observed. The XCO enhancement increases and expands from morning to early afternoon primarily driven by increasing CO emissions and atmospheric transport even though the winds are relatively weak compared to late afternoon. On average, the magnitude of the XCO enhancement in the day time is about 16.8% (an increase of 10.5 ppb from 62.5 ppb at 8–9 h to 73.0 ppb at 14–15 h; **Figure 5.3**); (3) Atmospheric dynamics (sea breeze and wind fields in Figure 7) and terrain effects significantly affect the spatial distribution of XCO enhancement in the late afternoon. The dynamical effect also has a strong seasonal cycle, which will be discussed in **Section 5.4**. When winds from the ocean cross downtown and bring the pollution eastward, the XCO enhancement in the downtown areas drops rapidly. In the late afternoon, the high XCO enhancement is mostly concentrated in and just below the San Gabriel Mountains in the north, as the winds drive the emissions toward the mountains. The XCO enhancements in **Figure 5.3** are averaged values over all the 33 sites. The drop between 14 h and 15 h is about 20% (from 72 ppb to 57 ppb). As can be seen in **Figure 5.2**, between 14–15 h and 15–16 h, the XCO enhancement in some sites near the ocean drops by more than 50%, due to the strong sea breeze from the ocean. On average, there is a 20% drop between 14 h and 15 h. The rise and mixing of the PBL may have an impact in diluting the local CO, but it is the strong sea breeze in the late afternoon that pushes the CO-rich air eastward and out of the observation domain. The reproduction of diurnal patterns of XCO enhancement using WRF-Chem model simulations is described in **Section 5.5**. This diurnal variability is different from *in-situ* measurements from ground-based or tower stations (Newman et al., 2013), because surface measurements are sensitive to local traffic induced emissions while column abundance measurements are more sensitive to emissions integrated over a larger area and are driven by regional-scale meteorology (McKain et al., 2012).

These diurnal patterns revealed by CLARS-FTS observations have important implications for the inversion of urban carbon emissions from trace gas concentration measurements. First, the snapshot measurement provided by current LEO satellites (mostly with overpasses at local time of 13.5 h) is not representative of the emission pattern due to the high diurnal variability in urban trace gas concentrations. Second, ground-based measurements need to be combined with accurate atmospheric dynamics models for reliable emission inversion. Given the fact that most of the megacities are located in coastal regions with strong diurnal sea-land circulation, the diurnal patterns as shown in the LA basin highlight the importance of atmospheric dynamics in deriving carbon fluxes in coastal cities. This diurnal pattern of atmospheric dynamics has been a feature characterizing the landscape of the LA megacity (**Lu and Turco, 1995**).

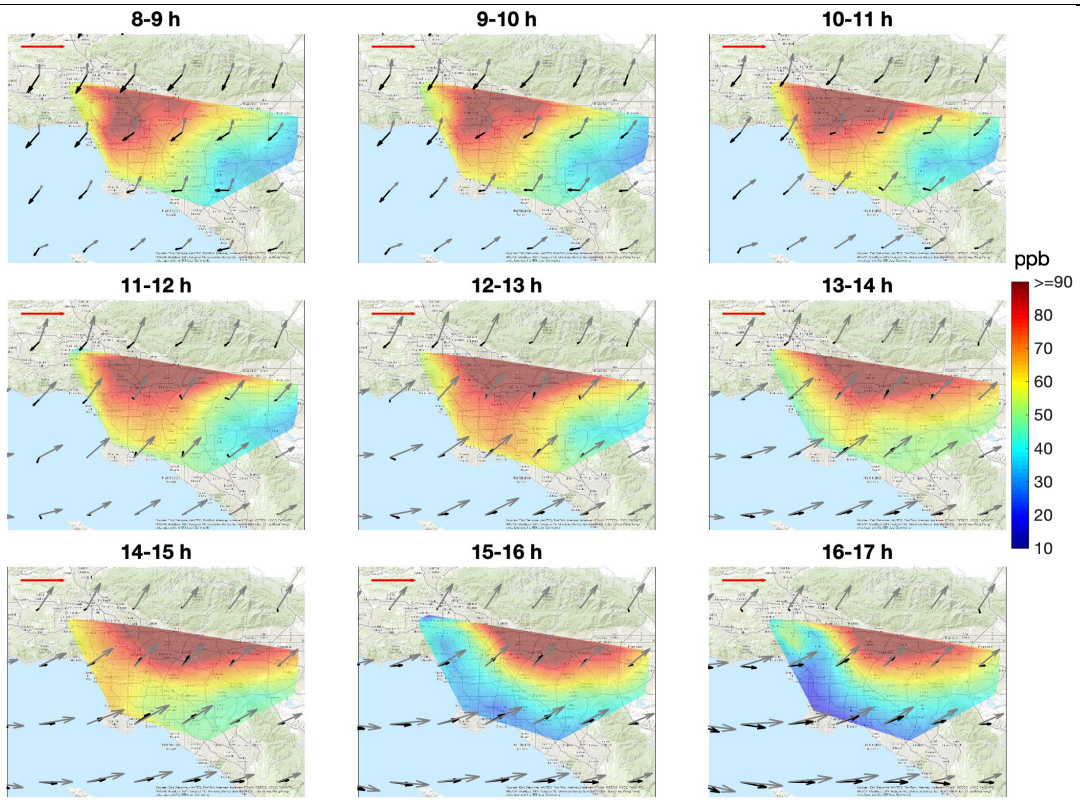

Figure 5.2. Hourly maps of XCO enhancement (ppb) in the LA megacity using CLARS measurements averaged from 2011 to 2018. The map is obtained by interpolating measurements at the 33 surface targets. The winds are monthly averages for January (black) and July (grey) at 100 meters above ground from ECMWF ERA5 reanalysis from 2012 to 2019. A comprehensive analysis of winds in the LA basin is presented in **Appendix A5**. The length of the arrows is proportional to the wind speed. The red arrow on the top left indicates a wind speed of 5 m/s, for reference.

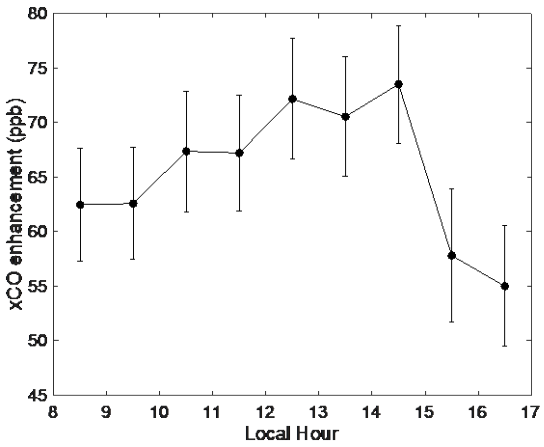

Figure 5.3. Hourly mean of diurnal XCO enhancement (ppb), which is an average of all CLARS retrieved values in the LA megacity from 2011 to 2018. The error bars denote the standard deviation.

5.3 Weekly cycles of XCO enhancement

The CO emission contrast between weekday and weekend has been reported using ground-based and airborne measurements (Kim et al. 2016) in the LA basin. This is primarily due to a 70–80% decrease in heavy-duty truck emissions over the weekends (Marr et al., 2002). Here, we report the spatial pattern of XCO enhancement weekday-weekend contrast in the LA megacity, as shown in **Figure 5.4**. To first order, the spatial patterns of XCO enhancement averaged over weekday and weekend are similar and generally consistent with the CO emission inventory. On average, the weekday XCO enhancement (90.5 ppb) is about 11.4% larger than the weekend value (81.2 ppb). This result is consistent with results from CalNex measurements and model simulations driven by the CO emission inventory (Kim et al. 2016), in which the weekend CO concentration is about 10% and 12% less than weekday values for the CalNex measurements and model simulations, respectively. The spatial distribution of weekday-weekend contrast can be seen in **Figure 5.4(c)**, which shows the ratio of weekday to weekend XCO enhancements. It is interesting to see that areas with relatively larger ratios are located in the western and southern parts of the LA basin. A possible explanation may be that these two areas experience larger decreases in heavy-duty truck emissions over weekends compared to weekdays. However, further investigation is needed with more truck emission observations over highways and local streets, which are currently not available, making the investigation beyond the scope of this study. Given the assumption that there are no major changes in atmospheric dynamics between weekdays and weekends, the spatial pattern of weekday-weekend contrast indicates the pattern of change of anthropogenic CO emissions, which is dominated by the change in heavy-duty truck traffic (Marr et al., 2002). In LA, more than 83% of CO is emitted from mobile sources and among them 47% is from on-road motor vehicles. We compare the weekly variability of XCO enhancement with the traffic count, as shown in **Figure 5.4(d)**. The traffic count is the sum of hourly flows over the day from the Caltrans Performance Measurement System (Caltrans PEMS, 2019). The PEMS traffic count data is collected in real-time from over 39,000 individual detectors distributed along the freeway system in California. Here we use the data from Los Angeles and Ventura counties, San Bernardino and Riverside counties, and Orange county, respectively. Since PEMS traffic count data are only available on highways, we assume their weekly variability is representative of the total traffic in LA. The variabilities in both quantities correlate well with each other when considering the data uncertainty. Compared to the average weekday (Monday through Friday) XCO enhancement, Saturday enhancements are 3.3% lower and Sunday values 14.0% lower. For the traffic count, the corresponding values are 3.3% and 14.8%, respectively. The consistency shows the effectiveness of CLARS-FTS measurements in quantifying the change of human activity-related carbon emissions between weekdays and weekends. The mismatch between the weekly time series of XCO enhancement and traffic count can be attributed to the following two causes: (1) vehicle count is assumed to be a direct indicator of emissions; this may not always be true since the variation in emission factors for different vehicle types is not considered. Different vehicle types will have different emission factors, implying that the total emission could be different even if the traffic count remains the same; (2) the PEMS traffic sensors are only available on highways. Therefore, PEMS traffic count data may not be representative of all the traffic in the basin, especially those on local streets.

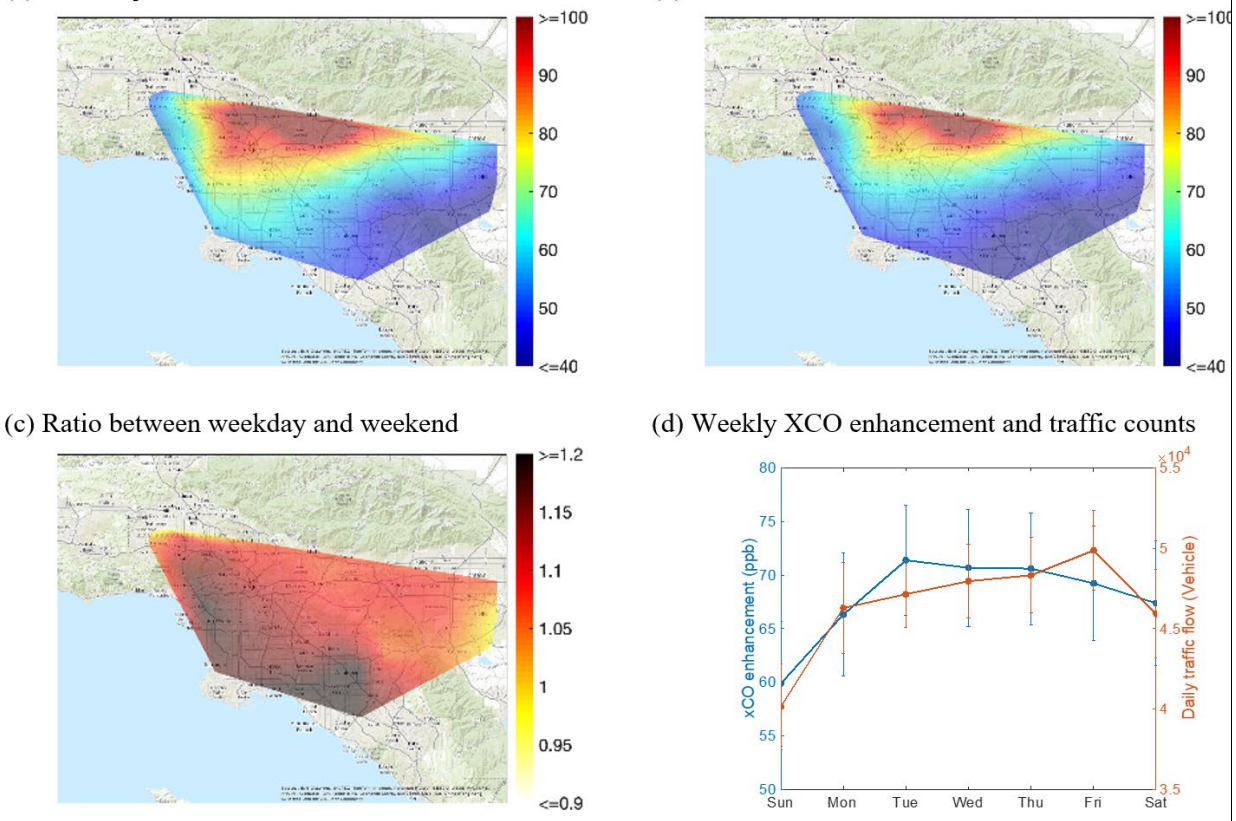

Figure 5.4. Weekly variability of XCO enhancement in the LA megacity. (a) Spatial pattern of weekday XCO enhancement averaged over all retrievals from 2011 to 2018; (b) Same as (a) but for weekends; (c) Ratio of weekday and weekend XCO enhancements; (d) Weekly variability of XCO enhancement compared with traffic counts from PEMS (pems.dot.ca.gov). Daily measurements for all stations in District 7 (Los Angeles and Ventura counties), District 8 (San Bernardino and Riverside), and District 12 (Orange County) are used. The spatial distribution of sensors is shown in **Appendix A6**. The PEMS traffic count data is collected in real-time from over 39,000 individual detectors distributed along the freeway system in California.

5.4. Seasonal cycles of XCO enhancement

The spatial pattern of seasonal XCO enhancement, as shown in **Figure 5.5,** shows significant change from season to season. Spatial correlation of the corresponding wind fields with XCO enhancement indicates that such changes are primarily driven by seasonal wind patterns. In winter, the strong Santa Ana winds (Raphael et al. 2003) coming from the northeast can be clearly seen. However, the atmosphere in the basin is relatively calm and the spatial distribution of XCO enhancement shows higher values around the downtown region and the foothill region below the San Gabriel Mountains in the north. In summer, the sea breeze is much stronger than in the other seasons, leading to higher contrast in XCO enhancement between northern and southern LA. In spring and autumn, the sea breeze is moderate. On average, the XCO enhancements for spring, summer, autumn, and winter are 71.5 ppb, 60.2 ppb, 66.0 ppb, and 71.3 ppb, respectively. Due to the spatial mapping capability of CLARS and the fact that CLARS measurements are largely unaffected by PBLH changes, analysis of the influence of atmospheric dynamics in regulating the CO concentration in the LA megacity becomes more effective and straightforward; on the other

hand, this may be harder for conventional ground-based measurement networks, whose samples of the near surface CO change have smaller footprints than those of CLARS column measurements. To get the same mapping capability, a large number of ground-based measurement towers may be needed. Further, the diurnal variability of PBLH needs to be simultaneously and accurately quantified for supporting the analysis of ground-based measurements (Newman et al. 2013), which is challenging.

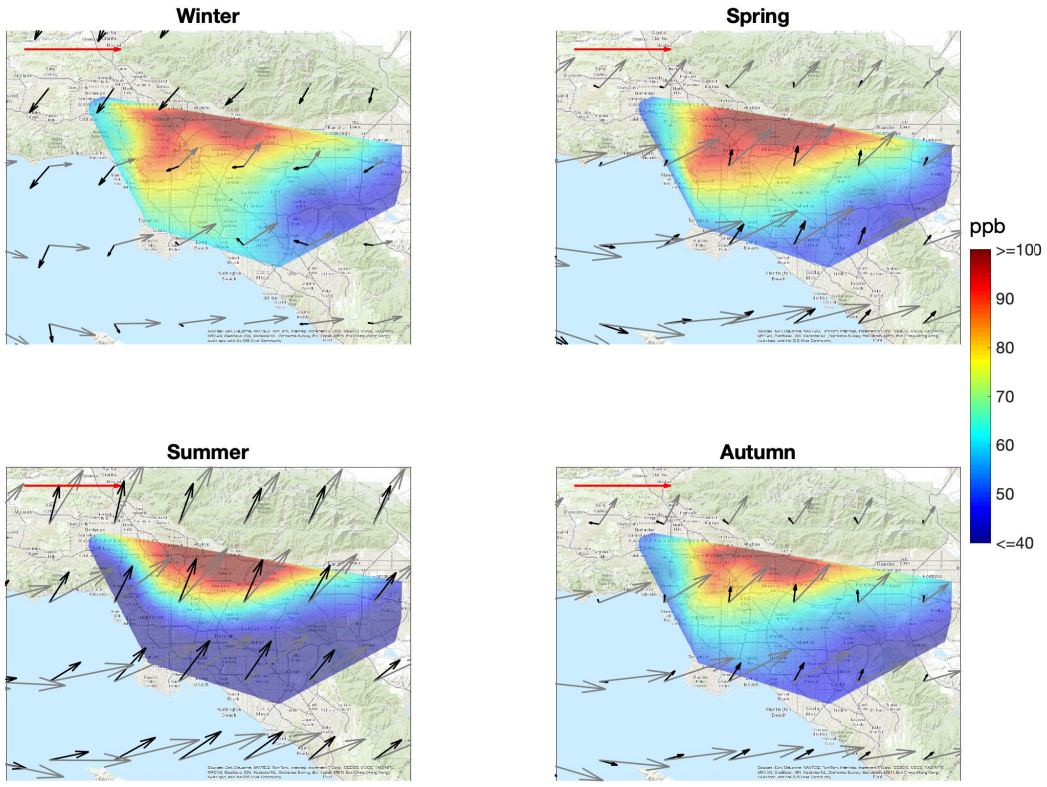

Figure 5.5. Spatial pattern of averaged XCO enhancement in the LA megacity for different seasons (Spring: March, April, and May; Summer: June, July, and August; Autumn: September, October, and November; Winter: December, January, and February). CLARS-FTS measurements from 2011 to 2018 are used to calculate the mean for all surface targets and to produce maps. The winds are monthly means for January (black) and July (grey) at 100 meters above ground averaged over 2012-2019 from ECMWF ERA5 reanalysis. A comprehensive analysis of winds in the LA basin is presented in **Appendix A5**. The length of the arrows is proportional to the wind speed. The red arrow on the top left indicates a wind speed of 5 m/s, for reference.

5.5. Evaluation using WRF-Chem simulations

The ability of the CLARS observation system to capture the atmospheric patterns of urban emissions in LA has not yet been studied. CLARS retrievals provide the slant column mixing ratio of CO. However, the quantity of interest is the change of XCO in the urban PBL. The spatial patterns of the relationship between the observed slant column XCO from CLARS and the change in XCO in the LA PBL need to be quantified. This quantification will define the representativeness of the CLARS observing strategy for capturing the variability of XCO enhancement. An effective approach for this investigation, similar to the OSSE (Observing System Simulation Experiment; Byrne et al. 2017) technique, is to use model simulations to create synthetic CLARS XCO measurements (as shown in **Figure 5.6(a)**) and calculate XCO enhancement in the urban PBL (as shown in **Figure 5.6(b)**). By comparing these two datasets (retrieved XCO enhancement and assumed truth), we will be able to answer the following question: how accurately can the CLARS observatory, or more generally a mountain-top remote sensing instrument, reproduce the general pattern of XCO enhancement in a city, given its very special slant observing geometry?

A description of the WRF-Chem model is in **Appendix A7. Figure 5.6(a)** shows the XCO enhancement in summer from WRF-Chem model simulations. The XCO enhancement in the morning agrees with the trend in the emission changes, in which the enhancement increases until the early afternoon while the sea breeze is getting stronger and gradually bringing more CO rich air eastward. In the late afternoon, the strong breeze brings high XCO air to the north-east of the basin. We apply the CLARS observation operator, by tracing the light path using the observation and solar geometries of CLARS, to the simulation data and create synthetic CO measurements, which act as a proxy for CLARS observations where the simulation field represents the "truth". We then compare the derived maps of XCO enhancement from CLARS synthetic observation to the "true" XCO enhancement. The result is shown in **Figure 5.6(b)**. Clearly, the CLARS synthetic data capture the essential features of the model simulations in (a). A scatter plot is shown in **Figure 5.7** to quantify the correlation between the CLARS synthetic and WRF-Chem simulations. Both maps show a high degree of agreement for all hours of day (r^2=0.69). CLARS synthetic maps, created from sampling the 33 surface reflection points, can explain more than 69% of the spatial variability of the "true" atmosphere from WRF-Chem. The CLARS synthetic maps show higher values than the model simulations (with a regression slope of 1.09). This is because of the heterogeneous distribution of XCO in the northern LA basin such that the reflected light path of CLARS is always passing through a high concentration atmosphere on its way to the CLARS instrument in summer. This result demonstrates the representativeness of the CLARS observing strategy towards capturing realistic XCO enhancements in the LA megacity.

(a) WRF-Chem

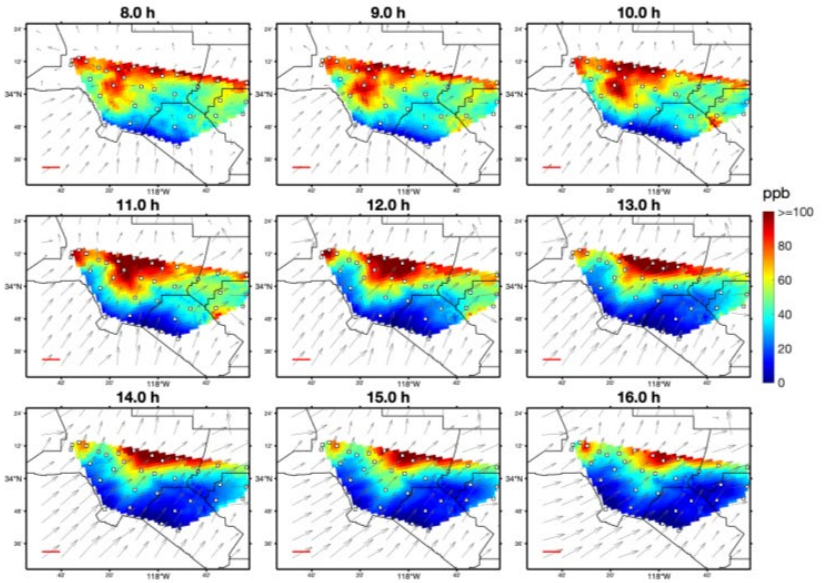

(b) CLARS synthetic

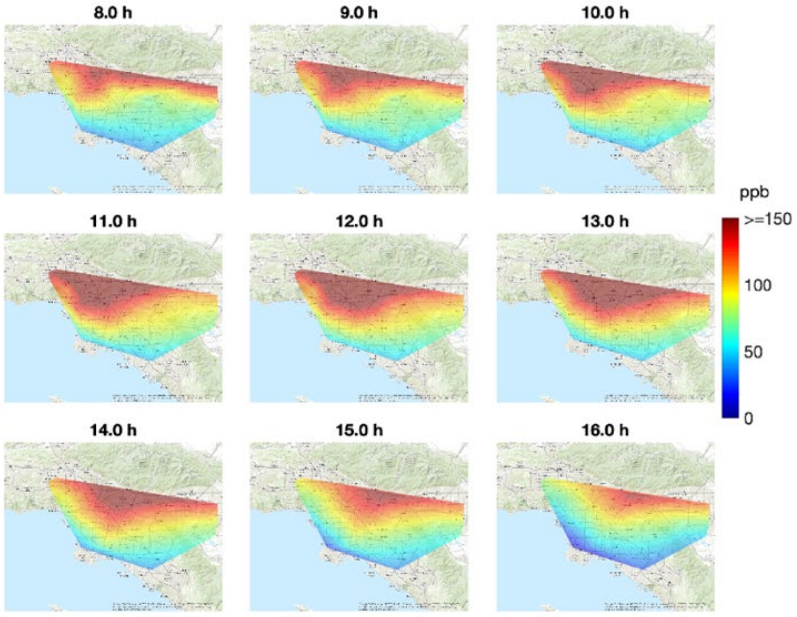

Figure 5.6. (a) Hourly maps of XCO enhancement in the basin simulated by WRF-Chem. The locations of the 33 surface reflection points of CLARS are indicated by white circles; The winds are averaged over the simulation days from model wind fields at 925 hpa simulated by WRF-Chem, which in turn is driven by ECMWF ERA5. The length of the arrows is proportional to the wind speed. The red arrow on the bottom left indicates a wind speed of 5m/s, for reference. (b) Hourly maps of XCO enhancement produced by first applying the observation operator to the WRF-Chem simulation in (a) to generate synthetic CLARS observations and then deriving the XCO enhancement maps. The CLARS observation operator traces the light paths, and the corresponding CO and O_2 densities along the path, in order to generate the SCD that CLARS might measure if the WRF-Chem simulation represents the "true" atmosphere. The simulations are generated for July 2016, representing a summer scenario. For the winter scenario, refer to **Appendix A8**. Please note that the data ranges for the color bars in (a) and (b) are not the same for the sake of spatial pattern comparison.

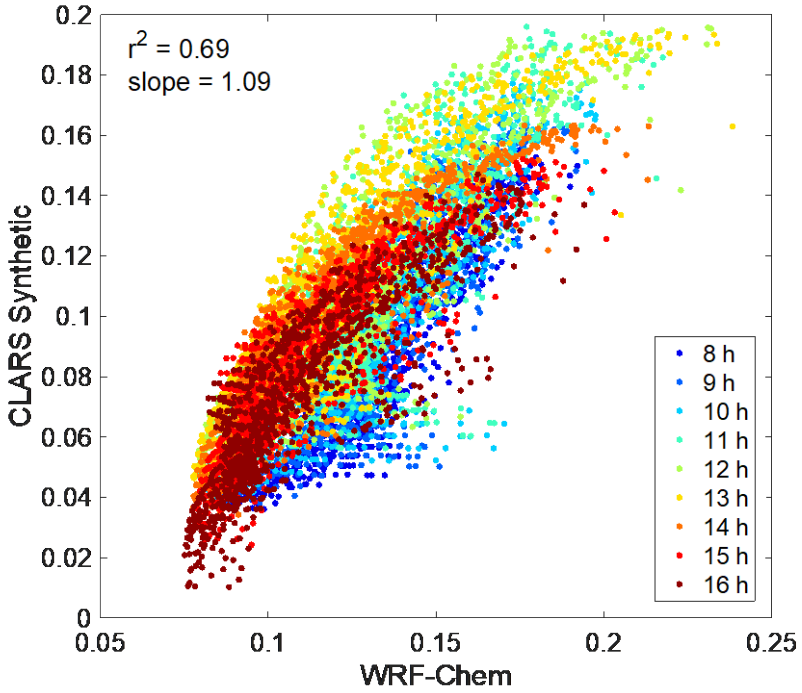

Figure 5.7. Correlation between maps from CLARS synthetic and WRF-Chem simulations. The CLARS synthetic data are sampled from the 2 km by 2 km grids of WRF-Chem. There are about 1000 points in the study domain.

5.6. Reduction of CO enhancement in LA during COVID-19

Carbon monoxide (CO) is a primary pollutant subject to a National Ambient Air Quality (NAAQS) standard. Health effects of CO are related to the onset of tissue hypoxia caused by binding with hemoglobin in the blood, increasing mortality for individuals with underlying conditions such as heart disease. In urban areas such as Los Angeles, more than 70% of CO is emitted from mobile sources with smaller contributions from fossil-fueled power plants and other stationary sources (Zeng et al., 2020). As discussed in Section 1, lockdown measures had a very large impact on vehicle miles traveled (VMT) in the South Coast Air Basin (SoCAB) resulting in a clear signal in CO emissions as measured by the CLARS-FTS remote sensing spectrometer on Mt. Wilson, overlooking the SoCAB. **Figure 5.8** shows that the CO column abundance decreased by 37.5% in April, 2020 compared with the April mean from 2012-2019. The LA downtown region, where CO concentrations are normally the highest, experienced the largest decrease.

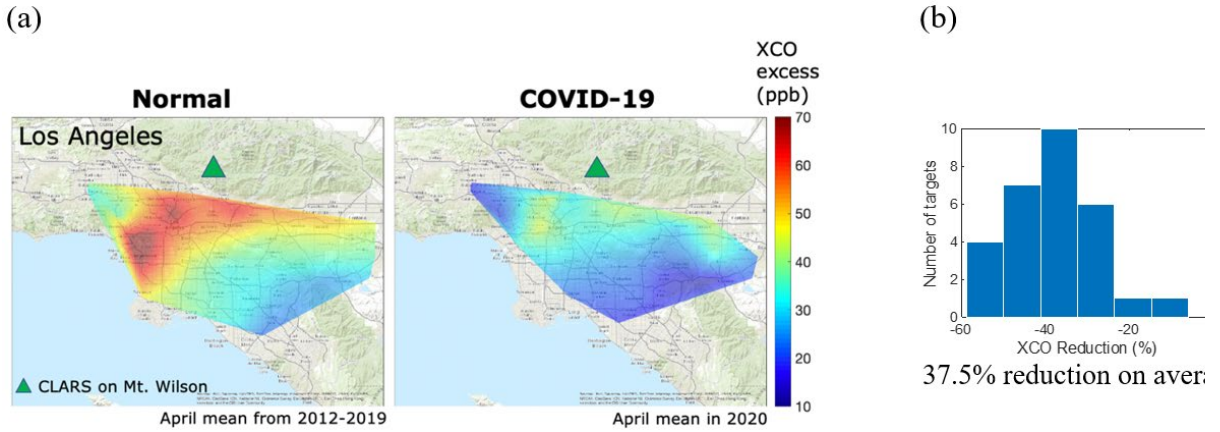

Figure 5.8. (a) Maps of CO column abundance (XCO) in excess of the background in the Los Angeles (LA) basin averaged for the month of April. Left panel (Normal): April noontime average for 2012-2019. Right panel (COVID-19): April 2020 during lockdown. These maps are interpolated from the 33 surface observation targets by CLARS-FTS; (b) The histogram of difference between XCO excess measurements in (a) for all the surface observation targets. The averaged XCO excess reduction is 37.5% on average due to the lockdown order.

6. Inferring long term trend in aerosol compositions using angular scattering effect of aerosols

In this section, we take advantage of the multi-angle observational geometries of CLARS-FTS to constrain the aerosol angular scattering effect, which is associated with aerosol compositions, using the O_2 absorption spectroscopy. CLARS-FTS provides a wide range of scattering angles, from about 20° (forward) to about 140° (backward).

In order to study the aerosol scattering effect, we retrieved the O_2 SCD in the oxygen singlet delta ($^1\Delta$) band, which results from the transition between singlet and triplet oxygen **(**Leshchishina et al., 2010), at 1.27 μm using GFIT algorithm. However, aerosol scattering effects are not considered in the GFIT retrieval algorithm. Therefore, errors in the O_2 SCD retrieval are largely due to light path changes caused by aerosol scattering; this bias can be used to investigate the aerosol optical properties (Zhang et al., 2015; Zeng et al., 2018). The surface reflectance at the target reflection points can be calculated from the ratio of SVO-observed (incident solar spectrum) and LABS-observed (reflected sunlight) solar radiance under clear atmospheric conditions (defined as O_2 ratio larger than 0.98) using continuum measurements (where gas absorption is negligible) around the oxygen $^1\Delta$ band.

For this study, we chose three surface reflection points located in the western San Gabriel Basin: West Pasadena (W-P), Santa Anita (S-A), and Santa Fe Dam (S-F), as shown in **Figure 6.1(a)**. CLARS measurements over these three reflection points cover a wide range of aerosol scattering angles. Moreover, the aerosols in this area originate from the LA downtown area since the sea breeze induced by land-sea thermal contrast brings air pollution from downtown eastward to the San Gabriel Basin. The pollution in this region is especially severe in the afternoon, when the pollution may be trapped aloft as the mixed layer stabilizes (Lu and Turco, 1994). Observations of aerosol scattering from these three surface reflection points provide information on the aerosols from the LA megacity in general.

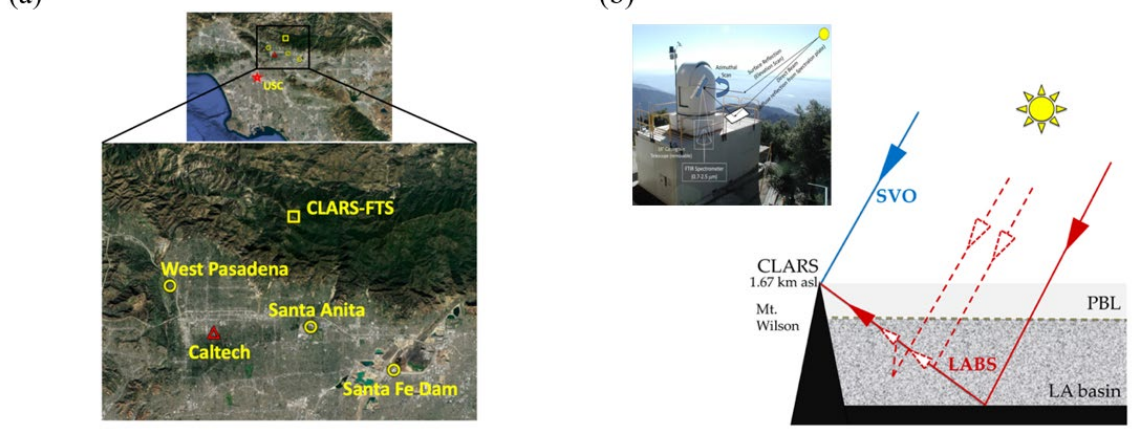

Figure 6.1. (a) CLARS-FTS near the top of Mt. Wilson and three of its surface reflection points in the LA basin: West Pasadena, Santa Anita, and Santa Fe Dam. The AERONET site at Caltech and meteorological station at USC in LA downtown are also indicated. The background image is adopted from Google Maps; (b) Schematic diagram of CLARS-FTS observing geometries. As an example, the light path change (in dotted red) due to aerosol scattering along the optical path from the basin surface to the instrument is illustrated. The aerosol scattering includes contributions from single scattering and multiple scattering.

6.1 O_2 Ratio as an indicator of aerosol scattering effect

In this study, we use the oxygen (O_2) SCD ratio (denoted by O_2 ratio), which is the ratio of retrieved O_2 SCD (denoted by $O_{2,\text{retrieved}}$ SCD) to geometric O_2 SCD (denoted by $O_{2,\text{geometric}}$ SCD), as a proxy for light path change due to aerosol scattering:

$$O_2 \text{ ratio} = \frac{O_{2,\text{retrieved}} \text{ SCD}}{O_{2,\text{geometric}} \text{ SCD}} \tag{6.1}$$

The geometric O_2 SCD is derived from National Center for Environmental Prediction (NCEP) reanalysis data with known observing and solar geometries and a constant oxygen dry-air volume mixing ratio of 0.2095. We also assume hydrostatic equilibrium and no scattering or absorption along the optical path (Zhang et al., 2015). In a non-scattering atmosphere, O_2 SCD retrievals from CLARS-FTS should have the same value as the geometric O_2 SCD. The Rayleigh scattering contribution is negligible since we employ measurements in the near infrared band at 1.27 μm. In a scattering atmosphere with aerosols, the change in optical light path due to aerosol scattering makes the retrieved O_2 SCD deviate from the calculated geometric O_2 SCD. Therefore, the deviation of O_2 ratio from unity provides a proxy for the extent of aerosol scattering over the basin, when the deviation is larger than the retrieval uncertainty, which is 0.5% for LABS measurements (Fu et al., 2014; Zeng et al., 2018). This approach of utilizing the O_2 retrieval as a proxy for scattering effects is equivalent to that used for GOSAT (Yokota et al., 2009) and OCO-2 (Crisp et al., 2008) retrievals, where O_2 A-band observations are compared with reanalysis data to discriminate light path-induced changes from changes in actual trace gas concentration (O'Dell et al., 2012; Taylor et al., 2016). The O_2 $^1\Delta$ absorption band at 1.27 μm used by CLARS-FTS for retrieving O_2 SCD is shown in **Figure 6.2**. The O_2 ratio effectively quantifies the strength of aerosol scattering. The rule of thumb for using the O_2 ratio to quantify aerosol scattering effects is: the lower the O_2 ratio, the stronger the aerosol scattering. If the O_2 ratio is 1.0, then there is negligible aerosol scattering effect.

Compared to the visible band, the 1.27 μm NIR band is much less sensitive to the fine mode aerosol particles (e.g., fresh smoke is almost transparent at 1.27 μm because of its very small particle sizes, which is on the order of 0.1 μm). Comparatively, it is the large mode particle aerosols that have larger impacts on GHG retrievals from NIR measurements with wavelengths greater than 1 μm. However, given the large amount of fine mode aerosol particles in the LA Basin, their impacts on the measurements in the 1.27 μm band can be large. Here we use MERRAero AOD reanalysis data (Rienecker et al., 2011) at 1.24 μm (which is very close to 1.27 μm) to calculate the contribution of fine mode aerosols to the total aerosol loading, as shown in **Figure 6.4(b)**. We used data for the five composite MERRA aerosols (black carbon, organic carbon, sulfate, dust, and sea salt) at 1300h local time over the LA region and averaged them from 2012 to 2014. Data below the CLARS elevation (1.67km) are used in this analysis. From **Figure 6.4(b),** it is evident that the monthly contribution from fine mode aerosols (black carbon, organic carbon, and sulfate), due to their high abundance in LA, is around 40% to 60%. Therefore, the O_2 ratio at 1.27 μm used in this study can be used to infer aerosol scattering effects for both fine- and coarse-mode aerosols.

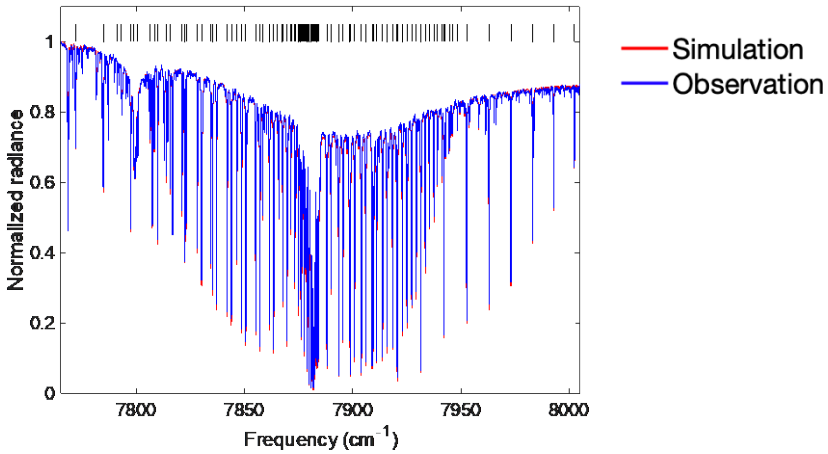

Figure 6.2. An example of normalized radiances in the oxygen $^1\Delta$ band at 1.27 μm, centered at 7885 cm^{-1} (1.27 μm) with width of 240 cm^{-1}, selected for retrieving O_2 SCD from CLARS-FTS measurements. The blue lines indicate CLARS-FTS measurements, including contributions from all trace gases and solar lines at a solar zenith angle of 69°. The red lines show the simulated absorption spectra calculated by the 2S-ESS RT model (**Appendix A9**) assuming no aerosol scattering effects. The black vertical bars indicate the spectral line positions of O_2. The spectra were measured at 15:20 local time over the West Pasadena surface reflection point.

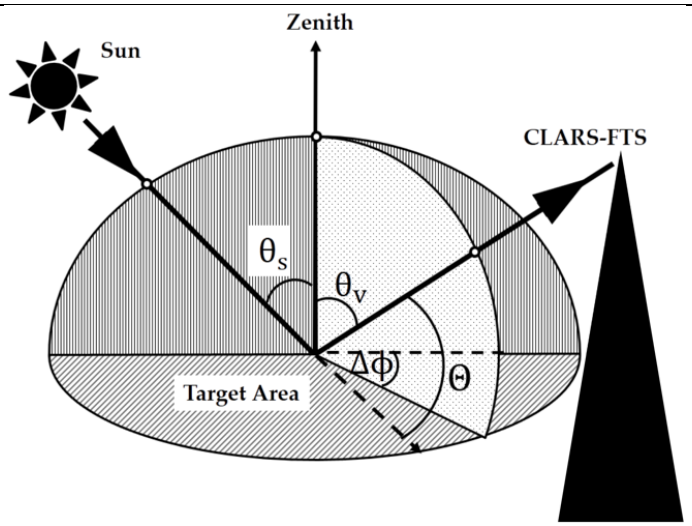

Figure 6.3. Illustration of the observing geometries of CLARS-FTS, including the scattering angle (Θ), solar zenith angle (θ_s), viewing zenith angle (θ_v) and relative azimuth angle ($\Delta\phi$). The scattering angle can be calculated from the zenith angles and the relative azimuth angle using **Equation (6.2)**.

The scattering angle is defined as the angle between the incident and scattered light beams, as shown in **Figure 6.3**. From spherical geometry (Liou, 2002), the scattering angle can be derived from the incoming and outgoing directions:

$$\cos(\Theta) = \mu\,\mu' + (1-\mu')^{1/2}(1-\mu'^2)^{1/2}\cos(\phi'-\phi) \qquad (6.2)$$

where μ and μ' are the cosines of solar and viewing zenith angle, respectively, and ϕ and ϕ' are the solar and viewing azimuth angles, respectively. The aerosol scattering phase function defines

the angular distribution of aerosol scattering energy in terms of scattering angle. **Figure 6.4(a)** shows the scattering phase functions following the Henyey-Greenstein approximation for various values of the asymmetry parameter g. The Henyey-Greenstein phase function (Henyey and Greenstein, 1941) has an analytical expression:

$$P_{HG}(\Theta) = \frac{1}{4\pi} \frac{1-g^2}{(1+g^2-2g\cos(\Theta))^{3/2}} \tag{6.3}$$

g=0.0 corresponds to isotropic scattering, where the scattering energy is the same in all directions. As the peak of the phase function sharpens in the forward direction, g increases. In **Figure 6.4(a)**, g=0.67 is the averaged asymmetric parameter at 1020 nm derived from the AERONET retrievals at Caltech (see **Appendix A10**). As a comparison, the phase functions for the five types of aerosols obtained from the MERRA aerosol reanalysis data (Rienecker et al., 2011) and calculated using the GOCART model (Colarco et al., 2010) are also shown. Clearly, the averaged phase function from AERONET ranges between the phase function of aerosols from natural sources (dust and sea salt) and those from mostly anthropogenic sources (black carbon, organic carbon and sulfate).

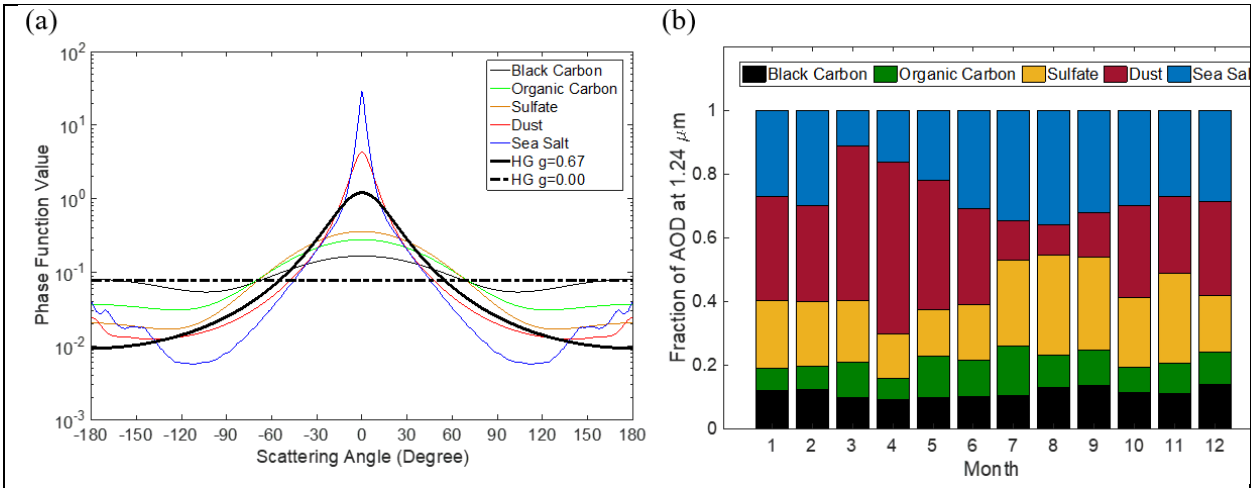

Figure 6.4. Aerosol scattering phase function for five different aerosol types, including black carbon, dust, organic carbon, sea salt, and sulfate, and two phase functions following the Henyey-Greenstein approximation with asymmetry parameter (g) values of 0.67 and 0.0, respectively. The value g of 0.67 is the averaged asymmetry parameter in Pasadena inferred from AERONET-Caltech; (b) Monthly averaged fraction of AOD at 1.24 μm for five different composite MERRA aerosol types (black carbon, organic carbon, sulfate, dust, and sea salt) at 1300h local time in LA, averaged over the time period from 2012 to 2014. MERRA AOD data below CLARS-FTS elevation (1.67km) are used. The five types of aerosols are obtained from MERRA aerosol reanalysis data (Rienecker et al., 2011), with optical properties calculated using the GOCART model (Colarco et al., 2010).

6.2. Simulating aerosol scattering using radiative transfer model

6.2.1 2S-ESS RT Model

The Two-Stream-Exact-Single-Scattering (2S-ESS) RT model (Spurr and Natraj, 2011) is used to simulate the observations and quantify the effect of aerosol scattering on the changes in O_2 ratio retrieved from CLARS-FTS. The 2S-ESS RT model is a numerically efficient but quite accurate (typically within a few percent of exact calculations and in most cases with biases less than 1%) technique for simulating radiances for hyperspectral observations. This model analytically computes the single scatter contribution in an exact manner by using all scattering phase function moments, and uses the two-stream approximation only to simulate the multiply scattered radiation field. The exact single scattering calculation largely eliminate biases due to the severe truncation of phase function inherent in a traditional two-stream approximation. Therefore, the 2S-ESS model is much more accurate than a typical two-stream model, especially in optically thin atmospheres where single scattering dominates or in scenarios dominated by strong gaseous absorption where the single scattering approximation is also very accurate. This model has been widely used for remote sensing of trace gases in previous studies (Xi et al., 2015; Zhang et al., 2015; Zhang et al., 2016; Zeng et al., 2017; Zeng et al., 2018). The settings of the RT model follow those used by Zhang et al. (2015) and Zeng et al. (2018). Basically, the *a priori* profile of atmospheric composition is obtained from NCEP-NCAR reanalysis data (Kalnay et al., 1996); the absorption coefficients for the oxygen molecules and the vertically stratified optical depths are computed using the GFIT program (Toon et al., 1992); the surface reflection is derived from CLARS-FTS measurements; Rayleigh scattering calculations are included in the model; the aerosol scattering phase function in the RT model is assumed to follow the Henyey-Greenstein approximation (Henyey and Greenstein, 1941). Below the CLARS altitude, the atmosphere is divided into five layers. Aerosols in these layers are assumed to be horizontally homogeneous. The aerosol optical properties, including single scattering albedo and asymmetry parameter, are adopted from AERONET measurements at Caltech. The radiance computed by the RT model is convolved using the CLARS-FTS instrument line shape (ILS) (Fu et al., 2014). The spectral resolution of the output radiance wavelength grid is set to be the same as the CLARS measurement resolution (0.06 cm^{-1}). The signal-to-noise ratio (SNR) is assumed to be constant at 300. Gaussian white noise is then added to the simulated spectra. The aerosol optical depth (AOD) measurements from AERONET-Caltech cover the wavelength range from 340 nm to 1020 nm; however, the O_2 $^1\Delta$ absorption bands (7885 cm^{-1}, ~1270 nm) used in this study are outside that range. To calculate the AOD in this band, we use the Ångström exponent law (Seinfeld and Pandis, 2006) to extrapolate the AERONET data. The extrapolated AOD is evenly distributed in the PBL.

In order to quantitatively evaluate the effect of aerosol scattering on the retrieval of O_2 SCD from CLARS-FTS, we estimate the retrieval bias caused by aerosol scattering using a two-step process. First, synthetic spectral radiance data are generated by the 2S-ESS RT model using observed AOD from AERONET-Caltech. Second, O_2 SCD is retrieved by fitting the synthetic spectra using the RT model based on Bayesian inversion theory (Rodgers, 2000). In the retrieval, the RT model has the same configuration as that used for generating the synthetic spectrum, but with AOD set to zero and not retrieved. As shown in Zeng et al. (2018), this two-step process reproduces the O_2 SCDs measured by CLARS and approximately quantifies the effect of neglecting aerosol scattering in the retrieval. The non-linear Levenberg-Marquardt algorithm is employed for fitting the spectra (Rodgers, 2000). A scaling factor, *viz.*, the ratio of retrieved O_2

SCD to the geometric O_2 SCD derived from NCEP reanalysis data, is the state vector element to be retrieved using the Bayesian inversion approach. This scaling factor is equivalent to the O_2 ratio.

6.2.2 O_2 Ratio as an Indicator of Aerosol Scattering Effects

The correlation between O_2 ratio, an indicator of light path changes due to aerosol scattering, and AOD, and its sensitivity to SSA, asymmetry parameter and surface albedo are shown in **Figure 6.5**. In general, the O_2 ratio decreases with increasing AOD. However, the slope decreases as the AOD increases. When aerosols are present, there are direct and diffuse (primarily aerosol scattering) components of solar radiation reaching CLARS-FTS. The diffuse component can be further separated into single scattering and multiple scattering components. The single scattering shortens the length of the light path through the lower atmosphere and leads to less O_2 molecular absorption (in this case, O_2 ratio < 1.0), while multiple scattering increases the absorption path length and leads to more absorption (in this case, O_2 ratio >1.0). Therefore, if the single scattering effect dominates (for optically thin atmospheres), the O_2 ratio is less than 1, as shown in **Figure 6.5**. As the AOD increases, the multiple scattering component becomes more important, which increases the O_2 ratio. This explains the decreasing correlation slope between O_2 ratio and AOD as AOD increases.

The O_2 ratio increases with decreasing SSA. On the other hand, it increases with increasing asymmetry parameter or surface albedo. This can be explained as follows. When SSA decreases, the aerosol becomes relatively darker and the scattering effect becomes weaker, resulting in a larger O_2 ratio. When the surface albedo is large, the surface contribution becomes dominant compared to the aerosol scattering effect. When asymmetry parameter increases, more scattering is concentrated in the forward direction (scattering angle < 20°) and less in other directions. Therefore, the light path is not modified significantly, leading to an increase in O_2 ratio. It can be concluded that O_2 ratio is an effective indicator of aerosol scattering effects and that the correlations establish sensitivity to aerosol and surface optical properties.

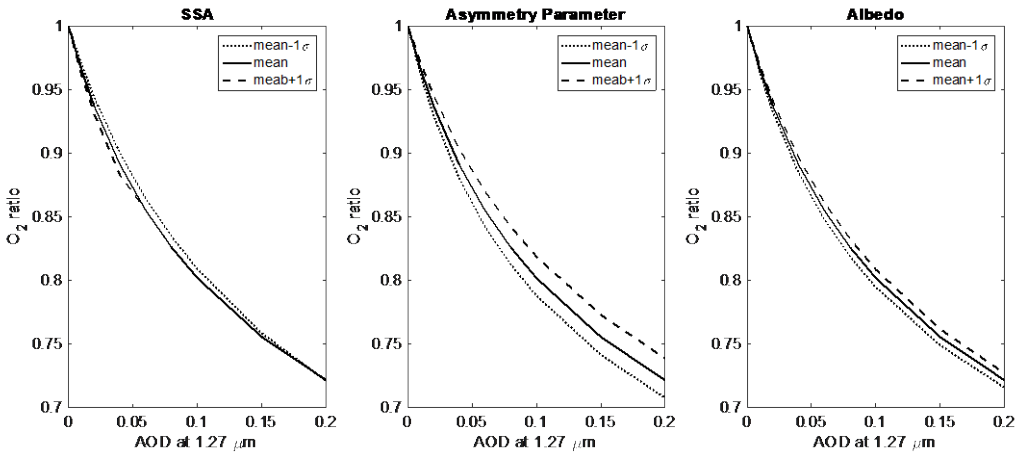

Figure 6.5. Correlation between O_2 ratio and AOD at 1.27 μm and its sensitivities to changes in SSA, asymmetry parameter, and surface albedo, respectively. The averaged SSA, asymmetry parameter, and albedo, from AERONET measurements at Caltech, are 0.92, 0.67, and 0.21, respectively, with corresponding standard deviation (one sigma) values of 0.13, 0.05, and 0.02. The dashed and dotted lines represent scenarios when the parameter is increased and decreased by one sigma, respectively. SSA is set to be 1.0 if the sum is over 1.0. The RT model settings are described in Section 3.1. The simulation is for the West Pasadena target, with a constant solar zenith angle of about 40°. The scattering angle is about 55°.

6.3. Results of aerosol angular scattering effects

6.3.1 Diurnal Variability of Aerosol Scattering Angle

The viewing zenith angles for the W-P, S-A, and S-F surface reflection points are 83.13°, 80.48°, and 84.07°, respectively. For these three surface reflection points, the reflected light goes through 8.36, 6.04, and 9.68 times the air mass, respectively, of nadir mode geometry in the PBL where most urban pollutants are trapped. Further, the observation geometries span a wide range of aerosol scattering angles. As illustrated in **Figure 6.6**, the S-F measurements are in the forward scattering direction in the morning, moving to backward scattering in the afternoon. The reverse is the case for W-P. A detailed quantitative description of diurnal scattering angle changes is provided in **Figure 6.7**. For S-F, the scattering angle increases from 30° (forward scattering) in the morning to 120° (backward scattering) in the afternoon. Conversely, for W-P, the scattering angle decreases from 140° (backward scattering) in the morning to 20° (forward scattering) in the afternoon. Interestingly, the scattering angle change for S-A is much smaller compared to W-P and S-F. For all seasons, the change for S-A is less than about 20°. Moreover, from **Figure 6.7**, the scattering angles have seasonal dependence due to the change in the geometries of the incoming solar beam. The scattering angles in summer are generally larger than those in winter. Considering such distinct diurnal variability of scattering angles at these surface reflection points and the long reflected light path within the PBL, CLARS-FTS measurements are highly sensitive to the scattering effects due to urban aerosols.

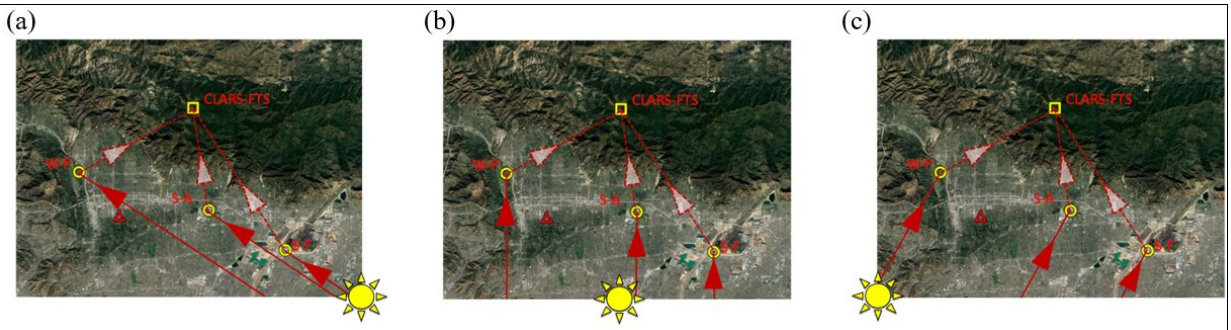

Figure 6.6. Illustration of incident (solid red) and reflected (dashed red) sunlight at the three surface reflection points (W-P for West Pasadena, S-A for Santa Anita, and S-F for Santa Fe Dam) for three different times of the day: (a) morning, (b) noon, and (c) afternoon. The light paths are the projections on the surface. The actual light paths in 3-D space are not shown.

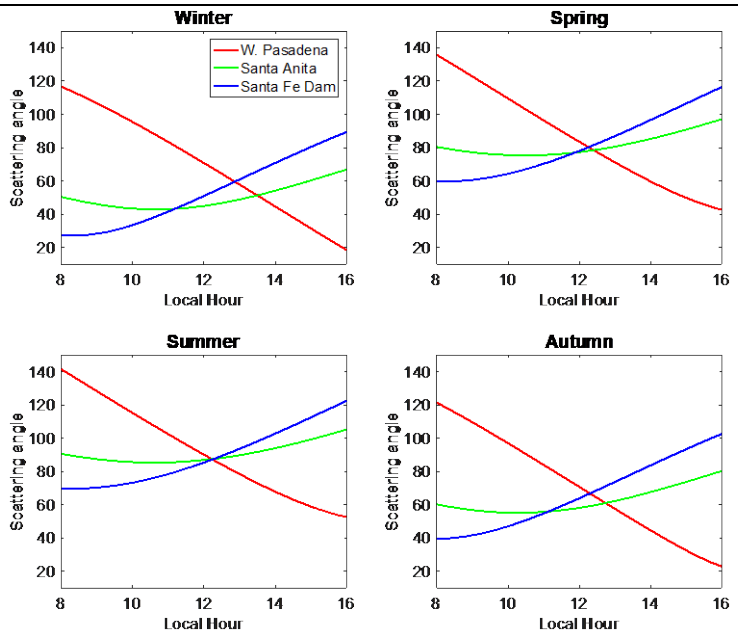

Figure 6.7. Diurnal variation of aerosol scattering angle, calculated using **Equation (6.3)**, from 8.0 h to 16.0 h local time over the three surface reflection points of West Pasadena, Santa Anita, and Santa Fe Dam for four different seasons: Winter, Spring, Summer, and Autumn, represented by the observing geometries on Jan 15, April 15, July 15, and October 15, respectively.

6.3.2 Diurnal Variability of O_2 Ratio

Since all the reflection points are located very close to the AERONET-Caltech site (the distances are 5.0, 7.7 and 14.9 km, respectively for W-P, S-A, and S-F), it is reasonable to assume that the vertical aerosol loadings at these three locations are almost the same. Therefore, the diurnal difference in aerosol scattering effects can be primarily attributed to differences in scattering angle, given that the surface reflectance can be estimated with high accuracy. **Figure 6.8** shows the O_2 ratio retrievals from CLARS-FTS for W-P, S-A, and S-F. Even though the observed AOD keeps increasing from the morning to the afternoon (**Figure 6.8(c)**), the changes in O_2 ratio for S-A are relatively small, and remain constant in the afternoon. This is because the change in scattering angle for S-A is smaller compared to W-P and S-F. The O_2 ratio for W-P, however, decreases from the morning to the afternoon, corresponding to enhanced aerosol scattering from two effects: increase in AOD and change from backward to forward scattering. On the other hand, the O_2 ratio for S-F has a small increase from the morning to the afternoon, indicating a weakening scattering effect. This is due to the sharp change in scattering angle from forward to backward scattering (**Figure 6.7**), partially offset by the increasing AOD. Such diurnal patterns are very coherent over all the measurements (over eight years) at the surface reflection points, as shown in **Figure 6.9**. S-F has larger variability compared to W-P and S-A because of the competition between AOD and scattering angle effects on the S-F O_2 ratio. The same conclusions can be drawn when O_2 ratios are plotted against scattering angle, as shown in **Appendix A11**.

The simulation results from the 2S-ESS RT model are shown as solid and dashed lines in **Figure 6.8** and as red lines in **Figure 6.9**. Overall, the RT model qualitatively reproduces the diurnal variation of O_2 ratios for all surface reflection points. The small differences between the measurements and the simulations may be due to the simplified assumption of H-G phase function and the usage of identical vertical aerosol loadings at all reflection points. To further investigate

the effect of angular scattering dependence, a control run as shown in **Figure 6.8(b)** was conducted. We kept all the same settings as for **Figure 6.9(a),** except that the asymmetry parameter of the aerosol phase function was changed to zero, i.e., scattering was assumed to be isotropic. Therefore, any changes in the simulation results can be attributed to the angular scattering effect. From **Figure 6.8(b)**, we can see that the distinctive diurnal patterns of W-P, S-A, and S-F disappear. All changes in O_2 ratio primarily follow the change in AOD. The results from this experiment suggest that the variation in scattering effects between W-P, S-A, and S-F CLARS-FTS measurements is primarily driven by the angular distribution of aerosol scattering in the LA basin.

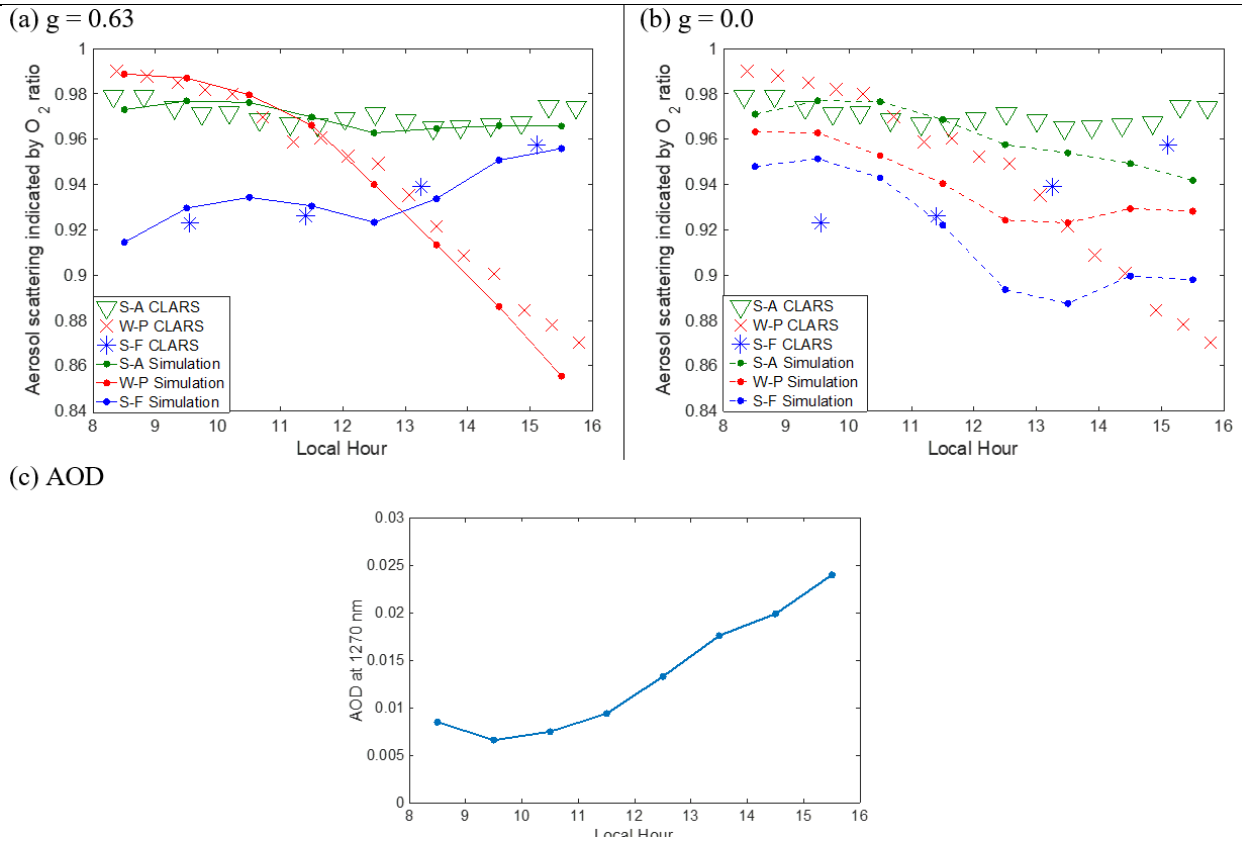

Figure 6.8. Comparison of O_2 SCD ratio, which is the ratio of retrieved O_2 SCD to geometric O_2 SCD, between measurements from CLARS and simulations from the 2S-ESS RT model over the West Pasadena (W-P), Santa Anita Park (S-A), and Santa Fe Dam (S-F) surface reflection points. (a) model simulations with asymmetry parameter (g=0.67) derived from the average of AERONET-Caltech data from 2011 to 2018; (b) control experiment (g=0.0) of model simulations assuming no angle-dependent aerosol scattering effect; (c) diurnal AOD from AERONET-Caltech on Oct 15, 2013. The AOD are sampled according to the observation time of the available CLARS measurements after filtering.

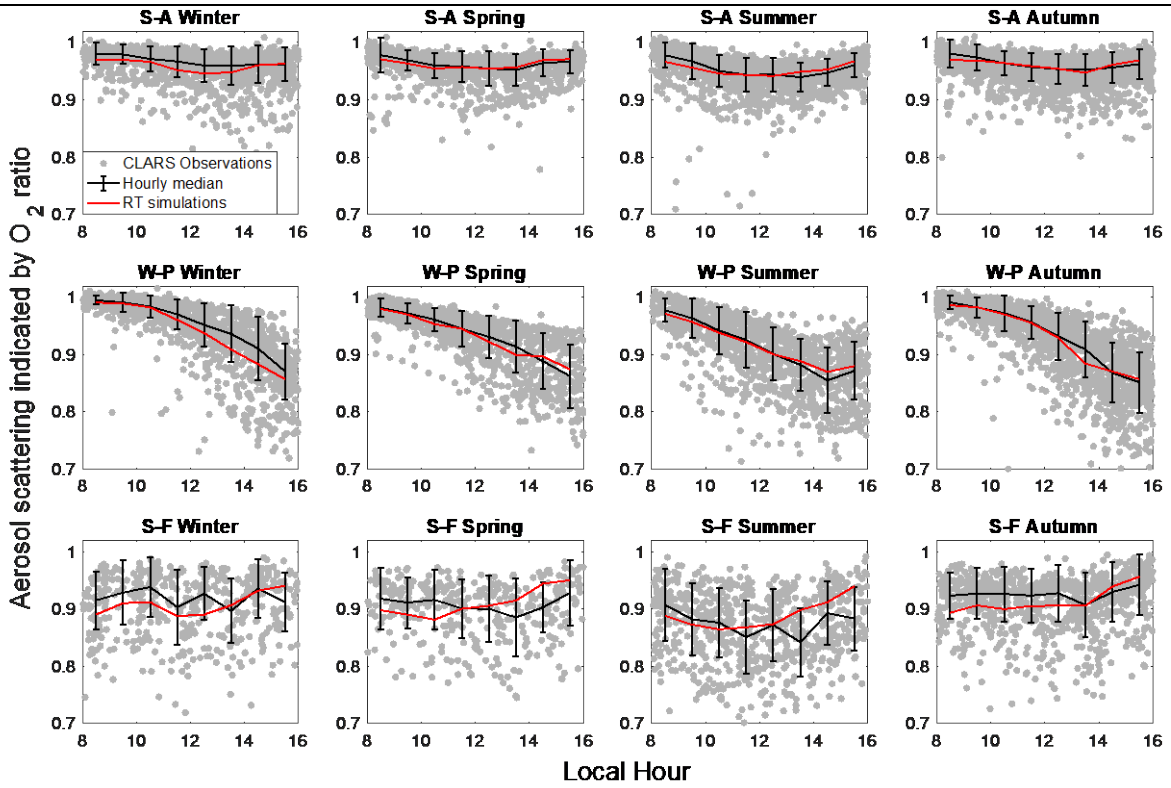

Figure 6.9. Multiyear average of O_2 ratio for the three surface reflection points, Santa Anita (S-A) on the top, West Pasadena (W-P) in the middle, and Santa Fe Dam (S-F) at the bottom from CLARS-FTS data for all seasons (original measurements in grey and hourly mean in black). The corresponding simulation estimates use the 2S-ESS RT model with averaged solar geometry, aerosol optical properties, and surface reflectance. All the data from 2011 to 2018 are used. **Appendix A11** shows the same plots but with the scattering angle as the x-axis.

6.3.3. Inter-annual Variability of O_2 Ratio

The interannual variability of the aerosol phase function may indicate changes in aerosol composition. For example, if there is an increase in fine mode particles from anthropogenic sources (e.g., black carbon, organic carbon, and sulfate), the asymmetry parameter will decrease since the angular dependence becomes weaker (as indicated by the phase function change in **Figure 6.4**). On the other hand, if the coarse mode fraction from natural sources (e.g., dust or sea salt) increases, the angular dependence will become stronger. Here, we develop a correlation technique between measurements at surface reflection points to quantify the strength of the angular dependence of the aerosol phase function. This technique investigates the correlation between the O_2 ratios from W-P and S-A in the late afternoon (14-16h in this study) when they have very different scattering angles. RT model simulations are shown in **Figure 6.10(a)**; we can see that the O_2 ratios are highly correlated between W-P and S-A. The slopes depend on the asymmetry parameter. To the first order, if the asymmetry parameter is higher, the slope between W-P and S-A will be higher. This correlation technique provides a way to quantify the anisotropy of the phase function.

We applied this correlation technique to the CLARS-FTS measurements as shown in **Figure 6.10(b)**. A strong correlation between W-P and S-A can be seen here. The real measurements are much noisier because the true aerosol properties have higher variability than

those assumed in the RT model simulations, which can affect the retrievals. It is evident that the CLARS-FTS measurements are highly mixed for different years, such that one can hardly disentangle the measurements by year. A linear regression is applied to fit the data for different years. The hypothesis here is that, if there is an interannual trend in the asymmetry parameter, there will be a trend in the regression slopes between W-P and S-A O_2 ratios. **Figure 6.10(c)** shows the time series of the regression slopes and the comparison with the annually averaged asymmetry parameter from AERONET-Caltech. Clearly, there is no significant trend from 2011 to 2018, inferred from both CLARS-FTS and AERONET data. This flat trend may be explained by a further investigation of wind measurements, as presented in **Appendix A12**, showing no significant trend in eastward wind speeds based on meterorological measurements in LA downtown from 2012 to 2018.

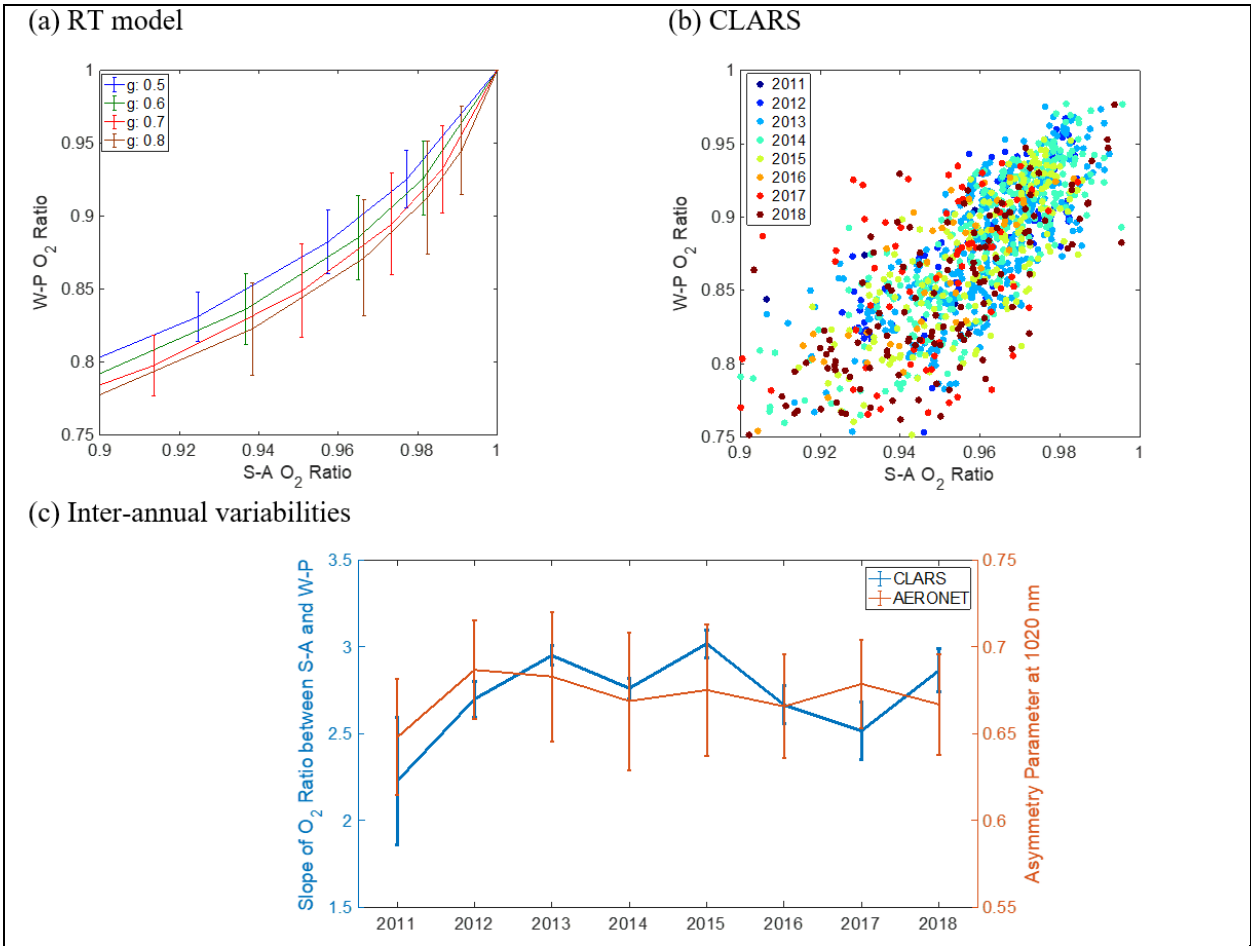

Figure 6.10. (a) Correlation of O_2 ratios between West Pasadena (W-P) and Santa Anita (S-A) surface reflection points for different asymmetry parameters (g) from 0.5 to 0.8 using the 2S-ESS RT model. The observing and solar geometries and all other related RT model inputs between 14h and 16h for all seasons are used for the RT simulation. The mean values are plotted and their standard deviations are shown as the error bars; (b) Scatter plot of O_2 ratio between W-P and S-A between 14h to 16h from CLARS-FTS retrievals from 2011 to 2018; (c) Regression slopes of O_2 ratio between W-P and S-A and comparison with annually averaged asymmetry parameter from AERONET-Caltech. The regression slopes are derived from applying a linear regression to fit the data in (b) for different years with the regression line forced to cross the [1,1] point.

6.4. Discussions of aerosol angular scattering effect

6.4.1 Impact of Aerosol and Surface Properties on O_2 Ratios at Different Target Sites

The correlation between W-P and S-A O_2 ratios is a good indicator of the aerosol phase function, as demonstrated in **Section 6.4.3**. Here, we explore the sensitivity of this correlation to different aerosol and surface properties, including asymmetry parameter, SSA and surface albedo, as shown in **Figure 6.11**. The simulation is implemented based on average solar and observation geometries at 15h for the spring season. The results show that, to the first order, the asymmetry parameter determines the different slopes between W-P and S-A, while SSA and surface albedo have smaller impacts on the correlation slope. This is because, when SSA or surface albedo changes, the O_2 ratios change simultaneously with similar magnitudes for both W-P and S-A. As a net result, their impacts on the correlation slope cancel out. On the other hand, when asymmetry parameter (indicative of the scattering phase function) changes, the O_2 ratio changes differently between W-P and S-A, which leads to different correlation slopes as seen in **Figures 6.10 and 6.11**. The data spread in **Figure 6.10(b)** and the error bars in **Figure 6.10(a)** are mainly due to the change in solar geometry (solar zenith angle and solar azimuth angle) over different seasons.

6.4.2 Applicability of CLARS Aerosol Observation System to Other Cities

This measurement system can be used for many other megacities with vantage points above high buildings or mountains. Even if the vantage points are not above the boundary layer, the measurement system can be optimized for measurements of aerosol optical properties such as phase function and single scattering albedo, which do not require the instrument to be situated above the PBL. This is different from measuring total aerosol loading or trace gas columns, which do have this requirement in order to get the best observation. The surface reflection points should be carefully selected to have surfaces with homogeneous characteristics. The universal measurement system for all cities will be similar to the current open-path remote sensing instrument (**Griffith et al., 2018; Byrne et al., 2019**) above a high tower or building for trace gas studies. Such open-path instruments can be adjusted to monitor the aerosol optical properties on a city scale.

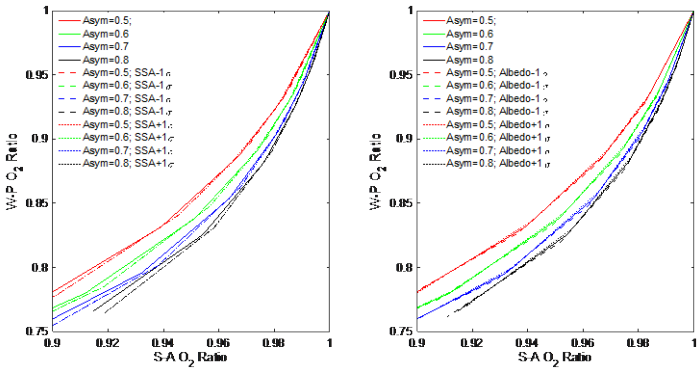

Figure 6.11. Similar to **Figure 6.10(a)** but varying aerosol SSA and surface albedo to investigate the sensitivity of the correlation between W-P and S-A O_2 ratio to aerosol and surface properties. (Left) Correlation of O_2 ratios between W-P and S-A surface reflection points for different asymmetry parameter (Asym) values from 0.5 to 0.8, different SSA (average value of 0.92, standard deviation (σ) of 0.13) using the 2S-ESS RT model, color-coded for different values of Asym. SSA is set to be 1.0 if the sum is over 1.0. The simulation is implemented based on average solar and observation geometries at 15h for the spring season; (Right) Same as left but for changing surface albedo (averaged value of 0.21, standard deviation of 0.02).

Chapter 7. Future work

7.1 Monitoring the long-term emission trends toward 2030

To establish compliance with California legislation that mandates the rollback of greenhouse gas (GHG) emissions (e.g., 40% reduction in GHG emissions by 2030), comprehensive, long-term observing strategies are required. We have demonstrated the capability of CLARS-FTS observations in monitoring the near-decadal trends of CH_4, N_2O, and CO. For future work, we will continue to 1) extend the CLARS-FTS data record; 2) process the CLARS-FTS spectra to obtain dry air slant column abundances and mixing ratios of the key greenhouse gases CH_4 and CO_2, as well as CO, N_2O, water vapor and O_2 (used for filtering the effects of aerosols and clouds); and 3) calculate trends of CH_4 and N_2O emissions using the tracer-tracer correlation method relative to CO_2. Successful completion of this project will provide CH_4 emissions data from late 2011 through the end of 2020. We will also analyze the data to search for relationships that may enable attribution of the measured emissions to the various contributing sectors including leakage from the natural gas infrastructure, landfills and sewage treatment plants. Where possible we will compare our results with other ongoing studies including surface monitoring stations operated by ARB and the Megacities Carbon Project. With CLARS-FTS data extending toward 2030, we will be able to provide a clear indication whether technical and administrative controls on CH_4 emissions targets specified in California legislation are succeeding.

7.2 Inverse modeling to retrieve spatially-resolved CO_2 and CH_4 emissions to help constrain point sources in LA

CLARS data coupling with inverse modeling framework would generate GHG emission maps with 1-4-kilometer spatial resolution to inform/detect emission hotpots and the potential super emitters. Moreover, the benefit of long-term CLARS data provide an opportunity to dissolve the source analysis according to the different temporal behaviors of individual source, including landfills, sewage treatment plants and fugitive emissions from natural gas production, storage and distribution systems which are primary sources in urban areas. The existing tower network in LA (e.g., Megacities Carbon Project) is sparse and subject to the high uncertainty of quantifying boundary layer height. Available global retrievals from satellites, e.g., OCO-2 and TROPOMI, have limited spatial resolution, limited sensitivity to GHG concentrations in the boundary layer and limited overpass time.

As a future work, we will apply an inverse modeling scheme to CLARS-FTS measurements to constrain the anthropogenic GHG emissions down to hourly and few-kilometer scales. The inversion analysis is conducted based on Bayesian optimal estimation. The transport from the surface to the ambient atmosphere is simulated by a Lagrangian particle dispersion model driven by the WRF mesoscale model. High-resolution meteorological simulations were performed using the WRF model to drive FLEXPART in order to simulate contributions to GHG mixing ratios from surface fluxes. By applying this inverse modeling scheme to CLARS-FTS measurements, we can constrain the GHG emissions of CO_2 and CH_4 down to hourly and kilometer scales. This study will be the first decadal trend analysis of spatially- and temporally- resolved anthropogenic GHG emissions in a major American megacity, thus providing a model for future studies mapping urban emissions at finer scale. It will also provide complementary information to previous global and regional trend analyses and significant diagnostic and prognostic information for urban emission management purposes.

Chapter 8. Conclusions

8.1 CH_4

Using mountaintop remote sensing with coverage over the greater Los Angeles basin, we observe seasonal excess methane emissions that correlate very well (R^2=0.50) with combined commercial and residential natural gas consumption. From the covariance we observe that the emissions arise from two terms: one that is seasonally invariant (14.0 ± 1.3 Gg/month) and another that peaks in the colder months of the year corresponding to (1.8 ± 0.18) % of residential plus commercial natural gas consumption. Other natural gas consumption sectors (industrial, power plant and transportation) either have no clear seasonal relationship that matches the observed emissions or are too small. The available emission factor data for residential and commercial natural gas-fired combustion sources fail to explain the observed emissions. Indeed, far more work needs to be done to measure the seasonally varying probability distribution functions of emitters under actual operating conditions.

8.2 N_2O

CLARS-FTS observations were used to investigate the temporal variability of N_2O excess mixing ratios and to calculate a top-down N_2O emissions estimate for SoCAB. No significant interannual trend is observed in $XN_2O_{xs,}$ but XN_2O_{xs} does exhibit a seasonal cycle with minima in late summer/ early fall and maxima in the early spring. A similar seasonal cycle is observed in top-down monthly emissions estimates calculated using a tracer-tracer ratio method with CO_2. The seasonal cycle could in part be related to precipitation and fertilization patterns in Los Angeles, as both soil moisture levels and fertilization practices are important factors in N_2O fluxes from urban lawns. Top-down monthly emissions estimates range from 6-19 Gg N_2O per month, while annual emissions range from 124 – 144 Gg per year for the years 2014 to 2018. Annual emissions estimates are roughly 3 times larger than statewide bottom-up inventories, but consistent within uncertainties with the top-down SoCAB emission estimate for 2007 reported by Wunch et al. (2009). The discrepancy between top-down and bottom-up N_2O estimates for both California and SoCAB highlights the difficulty in constraining N_2O emissions using bottom-up methods and in quantifying urban emissions on a local level.

8.3 CO

With CO being an effective tracer of anthropogenic emissions and atmospheric transport processes, the diurnal, weekly, and seasonal patterns of XCO enhancements inform the atmospheric pulse of the LA megacity. We show for the first time from a measurement perspective these patterns for CO in the LA basin. Using CLARS measurements from 2011 to 2018, we find that (1) the XCO enhancement shows a distinctive diurnal cycle primarily driven by changes in anthropogenic emissions and sea-breeze circulation. The diurnal patterns can be reproduced by WRF-Chem model simulations; (2) the XCO enhancement also shows a significant weekly cycle resulting from weekly patterns of anthropogenic CO emissions. On average, the XCO enhancements on Sunday and Saturday are 16.1% and 4.4%, respectively, lower than corresponding weekday values. The weekly XCO enhancement also shows significant correlation with traffic counts; (3) a seasonal pattern of XCO enhancement with high (low) spatial contrast in summer (winter) can be observed, resulting from seasonal variations in sea-breeze circulation. CLARS mimics geostationary observations of LA and can serve as a testbed for future geostationary missions to track anthropogenic emissions in cities. Aerosol scattering is the most important factor contributing to

biases in trace gas retrievals over urban areas. We demonstrate how to potentially mitigate aerosol-related biases by using a SCD scaling technique in conjunction with a simple data filter. This technique may be of use for future satellite missions measuring CO and/or other trace gases. Finally, we demonstrate the capability of WRF-Chem modeling to capture the CO emission patterns. Such a comparison would not be possible with conventional existing observations from LEO satellites or from ground-based measurements.

8.4 Aerosols

We used CLARS-FTS to quantify the angular scattering effect of urban aerosols on a city scale, which has been challenging due to a lack of appropriate observing systems. The angular scattering effects of aerosols are quantified by careful selection of surface reflection points that allow the observatory to measure the scattered light at different scattering angles. In this study, we use the ratio of retrieved to geometric O_2 SCDs instead of the absolute radiance to study the aerosol scattering effects, for two main reasons: (1) O_2 ratio has higher sensitivity to the ground level aerosols since the air density is higher and there are more O_2 molecules per unit volume. Therefore, the O_2 ratio as defined has advantages for detecting changes in aerosol optical properties close to the source of anthropogenic emissions; (2) understanding aerosol scattering effects on trace gas retrievals will help evaluate the impacts of light path uncertainty on the retrieval of trace gases from space, such as for the recently launched OCO-3 mission. However, if the aerosols are optically thick, the O_2 ratio may lose sensitivity since the O_2 absorption will be saturated. Using CLARS-FTS measurements from 2011 to 2018, we found that (1) the observation geometries from a mountain-top FTS over the LA megacity make it feasible to examine the aerosol scattering effect from forward to backward scattering. The long light path through the PBL makes the observations highly sensitive to aerosol scattering within the boundary layer; (2) The diurnal variability of aerosol scattering show distinct patterns for different surface reflection points, which are controlled by the total aerosol loading and changes in the scattering angle; (3) The changes in the angular scattering effects between the surface reflection points can be used to infer changes in the aerosol phase function. Analysis of CLARS measurements from 2011 to 2018 showed no significant changes in aerosol phase function during this timeframe in the LA megacity.

Appendix

Appendix A1. Detailed assumptions of tracer-tracer correlation method as applied to XN_2O_{xs} and $XCO_{2,xs}$

- XN_2O_{xs} and $XCO_{2,xs}$ are correlated even though the two GHGs are not emitted from the same sources. Both N_2O and CO_2 have chemical lifetimes that are much longer than the time scales for mesoscale transport and therefore will behave like inert tracers in the boundary layer. Though N_2O and CO_2 share some sources, such as fossil fuel combustion, certain major sources of N_2O, such as microbial activity in soils, are relatively insignificant sources of CO_2 emissions. Even so, mixing processes in the PBL occur on relatively short time scales on the order of 10-20 minutes and CLARS-FTS samples air masses that have undergone this short time scale mixing. The strong correlation values at 32 reflection points (excluding #29 due to lack of data) supports this mixing assumption over the entire basin.
- The $XN_2O_{xs}/XCO_{2,xs}$ ratio values observed at each LABS measurement point are sensitive to both the relative emissions over a horizontal path weighted toward the reflection point and the composition of the air mass advected into the atmospheric path. The long optical path in the boundary layer and the effect of advection smear out the effects of local emission ratio variations.
- The effect of aerosol scattering on the $XN_2O_{xs}/XCO_{2,xs}$ excess ratios is assumed to be negligible. Even though N_2O and CO_2 are retrieved at different wavenumbers (N_2O is retrieved near the 2.3 μm absorption band, while CO_2 is retrieved near the 1.61 μm absorption band), and aerosol scattering does exhibit a wavelength dependence, the difference in the bias due to aerosol scattering does not significantly affect the ratio between N_2O and CO_2 excess values. Evidence to support this assumption is presented in section 4.1 of the discussion.
- The number of discrete reflection points included in each basin averaged $XN_2O_{xs}/XCO_{2,xs}$ excess value is sufficient to characterize the average emission ratio over the Los Angeles megacity. The CLARS-FTS LABS mode spans slant distances in the range 4–40 km in the Los Angeles PBL and therefore should have sufficient spatial coverage of the megacity. Although data filtering reduces the number of reflection point locations included in basin-averaged excess ratio values for specific months and years, all basin-averaged seasonal excess ratios are calculated using data with sufficient spatial coverage to be considered basin-wide representations.
- Seasonal bias in the $XN_2O_{xs}/XCO_{2,xs}$ excess ratios is small. Although certain times of the year in LA are more likely to be influenced by cloud and aerosol events, we assume seasonal bias in the averaged $XN_2O_{xs}/XCO_{2,xs}$ excess ratios to be small.
- Spatial variation in the atmospheric column of CO_2 and N_2O above Mount Wilson is minimal and does not affect the $XN_2O_{xs}/XCO_{2,xs}$ ratio. Spatial variation in the CO_2 and N_2O mixing ratios above Mount Wilson in the basin is possible due to entrainment of boundary layer air mass into the free troposphere and long-range transport, but does not contribute significantly to the uncertainty in the $XN_2O_{xs}/XCO_{2,xs}$ ratio.

Appendix A2. Background calculation.

In order to calculate an excess mixing ratio value for each LABS measurement, an unbiased background value is derived along the same optical path as the CLARS LABS mode. SVO observations result from a direct solar beam and provide a useful representation of background mixing ratios for the portion of the atmosphere above the CLARS-FTS facility. At the same time, flask observations obtained from a NOAA in-situ instrument also located on Mt. Wilson provide a representation for the background below CLARS-FTS height. Since the height of the boundary layer reduces far below the CLARS facility during the night, nighttime flask samples provide representative background conditions for the lower troposphere above SoCAB, excluding influences from human activities. To construct a background for the entire LABS measurement path, the SVO retrievals are used for path 1, while NOAA flask measurements collected between 22:00 - 6:00 LT are used for paths 2 and 3 in **Figure A2**. The weights applied to SVO and NOAA flask measurements are based on the number of molecules along these respective paths:

$$Background\ XGHG = \frac{c_{SVO} * (n_1) + c_{NOAA} * (n_2 + n_3)}{n_1 + n_2 + n_3} \quad \text{(A1)}$$

where c_{SVO} is the complete result from applying PCR to the data record of SVO retrievals, c_{NOAA} is the complete result from applying PCR to the nighttime NOAA flask measurements for 2013-2019, and n_1, n_2, n_3 give the number of molecules along paths 1, 2, and 3 respectively. The number of particles within a vertical column particles can be defined using basic force principles as:

$$\frac{\Delta P * S}{g M_{air}} \quad \text{(A2)}$$

where ΔP is the pressure difference between the top and the bottom of the air column, S is the surface area of the column endcaps, and M_{air} is the molar mass of air. The number of slant column particles can then be determined geometrically:

$$n = \frac{\Delta P * S}{g M_{air} cos\emptyset} \quad \text{(A3)}$$

where $\emptyset$ is the angle the slant path makes with the vertical. Therefore the weights are respectively equal to:

$$n_1 = \frac{P_1\ X\ S}{g * M_{air} * \cos(\theta)} \quad \text{(A4)}$$

$$n_2 = \frac{(P_2 - P_1)\ X\ S}{g * M_{air} * \cos(\theta)} \quad \text{(A5)}$$

$$n_3 = \frac{(P_2 - P_1)\ X\ S}{g * M_{air} * \cos(\theta_0)} \quad \text{(A6)}$$

where θ is the solar zenith angle, θ_0 is the viewing zenith angle, and P_1, P_2 are pressures at the top of Mt. Wilson and at the basin surface respectively. The pressure at the top of the atmosphere P_0 is taken to be zero in the equation for n_1. Plugging in and canceling like terms yields

$$Background\ XGHG = c_{NOAA} * F_1 + c_{SVO} * F_2 \quad \text{(A7)}$$

Where F_1 and F_2 are defined as

$$F_1 = \frac{(P_2 - P_1) * (\cos(\theta) + \cos(\theta_0))}{P_2 \cos(\theta_0) + (P_2 - P_1)(\cos(\theta)} \quad \text{(A8)}$$

$$F_2 = \frac{P_1 \cos(\theta_0)}{P_2 \cos(\theta_0) + (P_2 - P_1)(\cos(\theta)} \quad \text{(A9)}$$

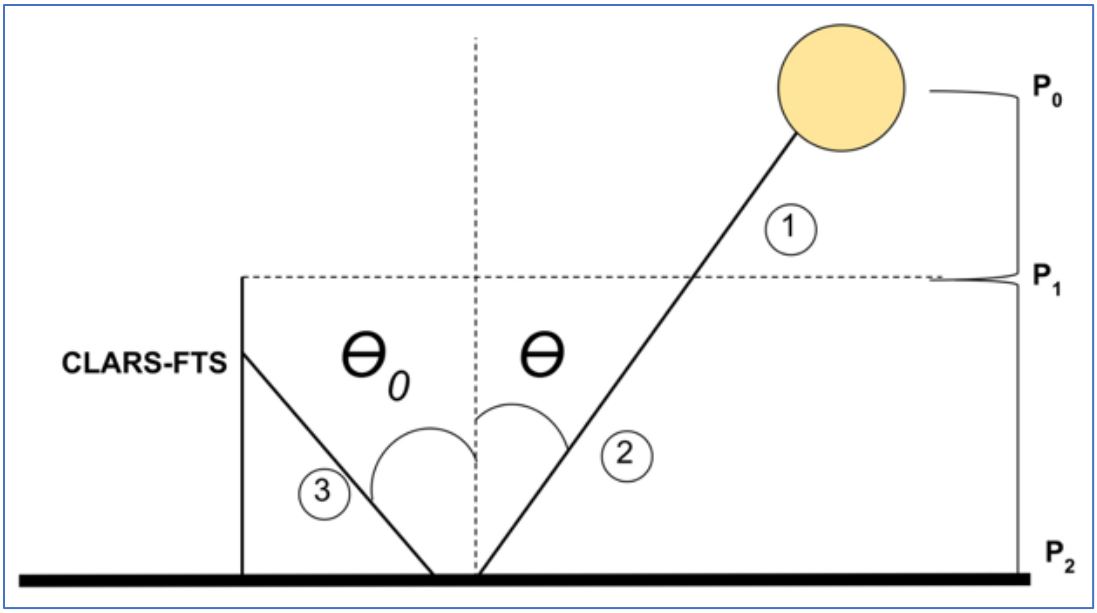

Figure A2: Diagram of 2-layer model of the atmosphere used for XN_2O and XCO_2 background calculation**,** where θ is the solar zenith angle, $\theta_0$is the viewing zenith angle, and P_0, P_1, P_2 are pressures at the top of the atmosphere, at the top of Mt. Wilson and at the basin surface respectively.

Appendix A3. Geometric correction for XCO excess from CLARS

The CLARS derived XCO difference (between LABS and SVO modes) depends on solar zenith angle since the LABS mode observation has two ray paths, one from the FTS to the surface that is fixed for a given surface target, and the other from the surface to the top of the atmosphere that changes with solar geometry. For the same amount of CO concentration in the boundary layer, the retrieved XCO difference is different for different solar zenith angles. XCO difference will be higher when the angle is smaller, and vice versa. In order to account for this geometric effect, we derive a correction factor by assuming a two-layer box model. XCO and XCOxs can be calculated using **Equations (1)** and **(2)**. The atmosphere is approximated by a two-layer model, with the interface between the two layers at the CLARS altitude. The boxes above and below CLARS are assumed to have CO mixing ratios of M_0 and M_1 respectively.

$$XCO_{svo} = M_0 \tag{A10}$$

$$XCO_{labs} = \frac{(M_0 * \frac{1-p}{\cos\theta} + M_1 * \frac{p}{\cos\theta} + M_1 * \frac{p}{\cos\theta_0})}{(\frac{1}{\cos\theta} + \frac{p}{\cos\theta_0})} \tag{A11}$$

where p is the ratio of the pressure at the CLARS level and the surface pressure (~0.16). θ_0 and θ are the viewing and solar zenith angle, respectively. Then, we have:

$$XCOdiff = XCO_{labs} - XCO_{svo} = (M_1 - M_0) * p * \frac{(\frac{1}{\cos\theta} + \frac{1}{\cos\theta_0})}{(\frac{1}{\cos\theta} + \frac{p}{\cos\theta_0})} = (M_1 - M_0) * p * \frac{(1 + \frac{\cos\theta}{\cos\theta_0})}{(1 + p * \frac{\cos\theta}{\cos\theta_0})} \tag{A12}$$

where M_1-M_0 is the XCO enhancement. From Equation (B3) we can get the correction factor between XCO difference and XCO enhancement.

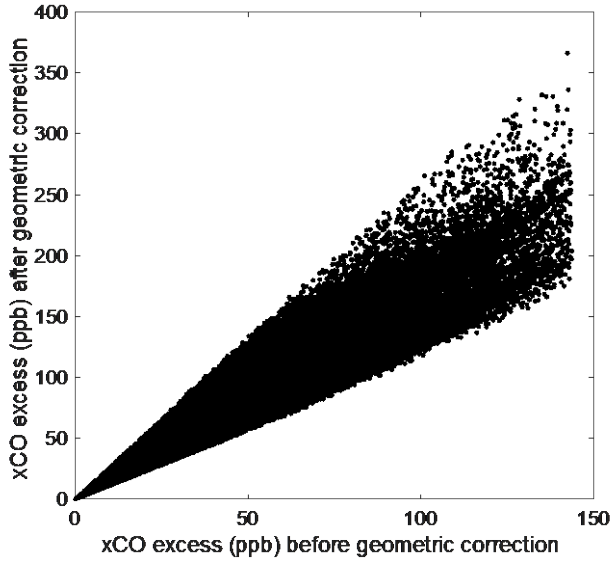

Figure A3. Scatter plot of XCO excess before and after geometric correction is applied.

Appendix A4. Averaging kernel correction

Wunch et al. (2009) and **Hedelius et al. (2018)** recommend that a correction should be implemented when comparing observations with different averaging kernels. As an example, **Figure A4** shows averaging kernels for CLARS-FTS retrievals of CO slant column density at 2.3 μm (the CO absorption band). We apply a correction to XCOxs based on the averaging kernel of the measurement. Similar to **Wunch et al. (2009)**, the XCO enhancement is divided by the averaging kernel value in the PBL to obtain the corrected XCO enhancement.

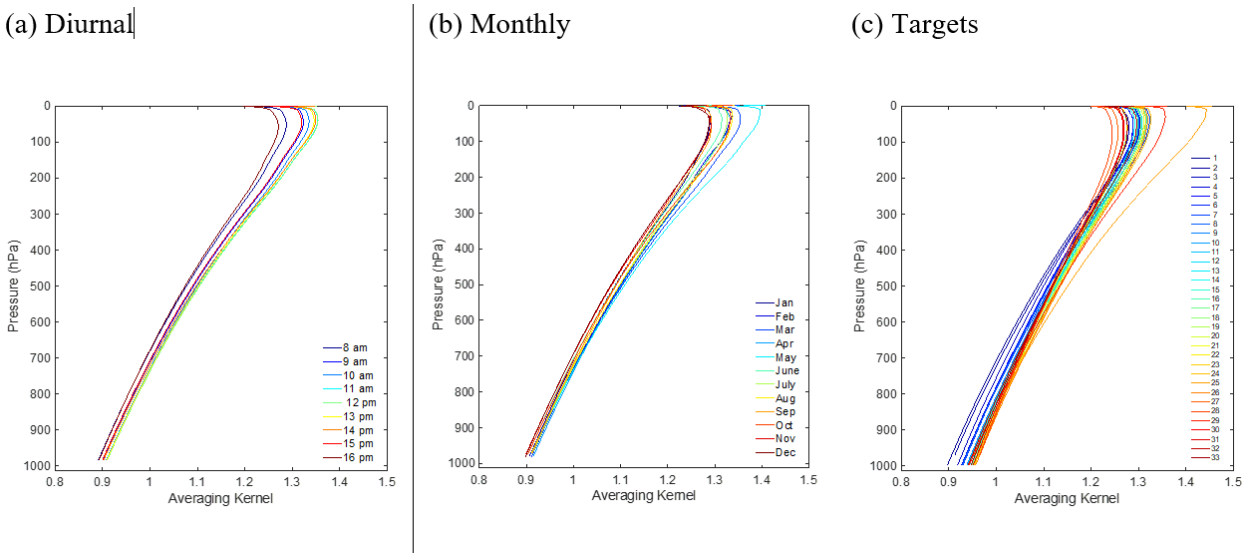

Figure A4. Averaging kernel for CLARS-FTS retrievals of CO slant column density at 2.3 μm (4290 cm^{-1}). (a) Example of diurnal variability of column averaging kernel from the W. Pasadena surface target on March 2013; (b) Example of monthly variability of column averaging kernel from W. Pasadena in 2013; (c) Example of column averaging kernels for different targets.

Appendix A5: Spatial and temporal patterns of winds in LA from ERA5 reanalysis

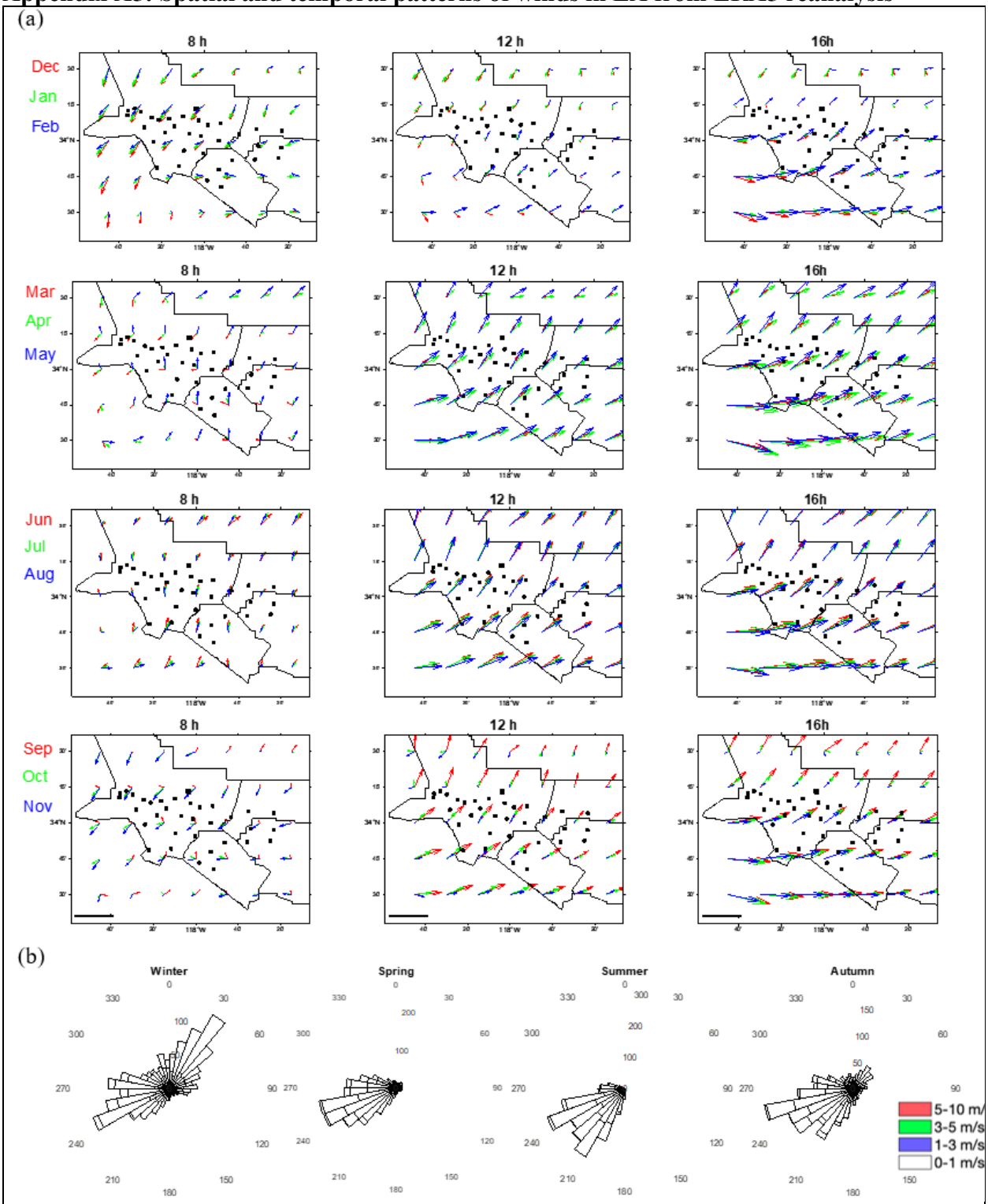

Figure A5. (a) Monthly and hourly averaged winds at 100 meters elevation in LA from ECMWF ERA5 reanalysis for the time period from 2012 to 2018. As examples, three hours of day are presented: 8h, 12h, and 16h. The data are extracted from the NCAR/UCAR CISL Research Data Archive (CISL, 2019). The length of the arrows is proportional to the wind speed. The black arrow on the bottom panel indicates a wind speed of 5 m/s, for reference. (b) Wind rose map for different seasons. All the hourly averaged wind data from ERA5 from 2011 to 2018 are

used.

Appendix A6. The PEMS measurement network

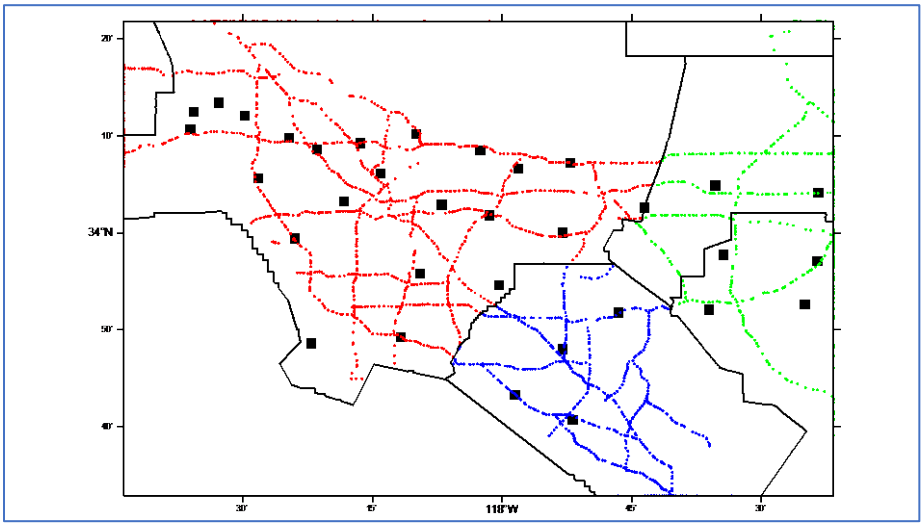

Figure A6. PEMS measurement network in LA (http://pems.dot.ca.gov/). Daily measurements for all stations in District 7 (Los Angeles and Ventura counties; in red), District 8 (San Bernardino and Riverside; in green), and District 12 (Orange County; in blue) are collected. The black squares denote the surface reflection points. The sensors basically cover all the major highways but not local roads and streets.

Appendix A7. WRF-Chem simulations

In this study, WRF-Chem v3.7 is used for model simulations of CO in the LA megacity to explain the variability of XCO enhancement observed by CLARS and to investigate the representativeness of the CLARS observing strategy for capturing this variability. WRF-Chem has been widely used for simulations of atmospheric chemistry including pollutant emissions at fine scale (e.g., Grell et al., 2005; Kim et al., 2016; Li et al., 2019). In this study, we follow the parameter settings in Li et al. (2019). We utilize the Lin cloud microphysics scheme, the RRTM longwave radiation scheme, the Goddard shortwave radiation scheme, the YSU boundary layer scheme, the MM5 similarity surface layer scheme, the Grell 3-D ensemble cumulus cloud scheme (for coarse-resolution domain only), and the unified Noah land surface model. In particular, the urban canopy model (UCM) in WRF-Chem is employed. It resolves land–atmosphere exchange over impervious surfaces in urban areas (Yang et al., 2015). The following chemistry schemes are included: the TUV photolysis scheme, RACM-ESRL gas-phase chemistry, and MADE/VBS aerosol scheme. We run the simulation for the first 10 days of four different months: January, April, July, and October in 2016, representing winter, spring, summer, and autumn, respectively. The simulation results for the first three days are meant as spin up and not used in the analysis. Hourly averages over the remaining seven days are used to obtain representative hourly values of CO in the LA megacity. Differing from Li et al. (2019), we use the European Centre for Medium-Range Weather Forecasts (ECMWF) ERA5 reanalysis dataset (ECMWF, 2019) as initial and boundary meteorological conditions. ERA5 reanalysis makes use of advanced modelling and data assimilation systems to combine historical observations into global estimates. For emission inventories, we use the US Environmental Protection Agency (EPA) National Emission Inventory (NEI) for 2011 (US EPA, 2011). To match the domain grids in the model, we regridded these inventories. **Figure A7** shows the three simulation sub-domains and the time series of anthropogenic CO emission.

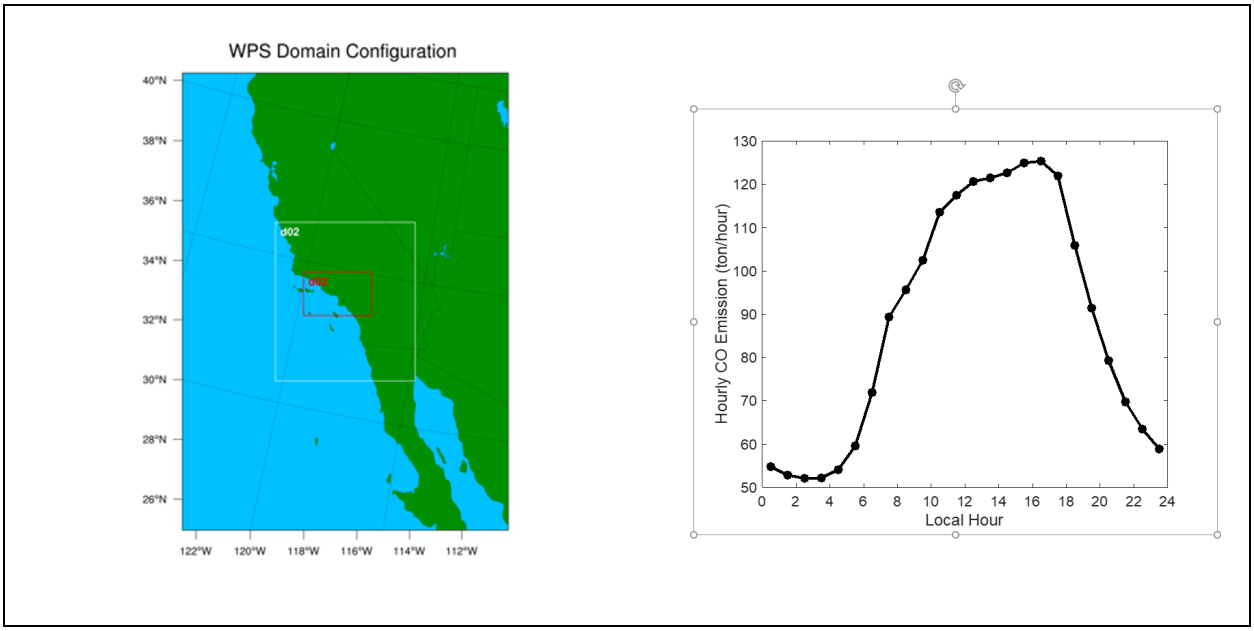

Figure A7. (a) Three nested WRF-Chem domains used in this study with horizontal resolutions of 18 km, 6 km and 2 km, respectively; (b) Diurnal pattern of bottom-up CO emission estimated from EPA inventory in the LA megacity, which is the center part of the inner domain (d03) in (a).

Appendix A8: Winter case for WRF-Chem simulations and CLARS synthetic data

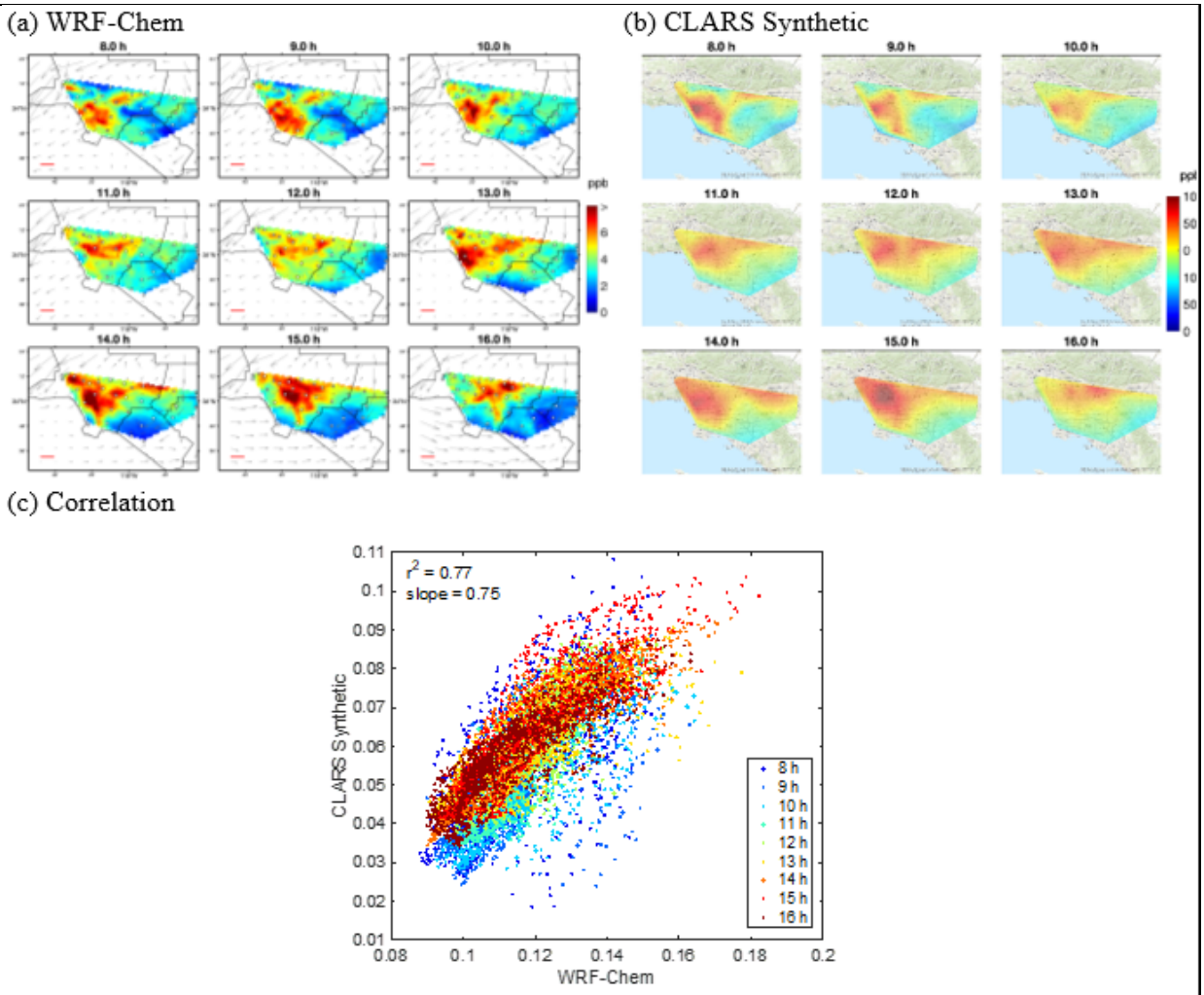

Figure A8. Same as **Figures 5.6** but for the winter season scenario with simulations for January 2016.

Appendix A9: 2S-ESS radiative transfer model

The 2-stream-exact-single-scattering (2S-ESS) radiative transfer model, developed by Spurr and Natraj (2011), is used in this study to simulate the reflected solar radiation observed by CLARS-FTS. 2S-ESS computes the single scattering using all moments of the aerosol scattering phase function to produce an exact single scattering radiation field, while multiple scattering is calculated using the two-stream approximation to achieve high computational efficiency. Under conditions when single scattering dominates, such as in urban regions with relatively dark surfaces, the 2S-ESS radiative transfer model produces accurate and fast results. This RT model has been used in several previous studies (Xi et al., 2015; Zhang et al., 2015, 2016; Zeng et al., 2017, 2018) for GHG and aerosol remote sensing. In the radiative transfer model, we use NCEP– NCAR reanalysis data (Kalnay et al., 1996) as the *a priori* atmospheric profile, which has 76 layers from the surface up to 70 km. Similar to Zeng et al. (2018), we separate the bottom part of the atmosphere below CLARS into five layers. Absorption coefficients for O_2 and CO molecules are adopted from the HITRAN database (Rothman et al., 2009). The gaseous optical depth for each layer is calculated using GFIT. The procedure for obtaining the surface albedo and AOD is described in Section 2.4. The model uses the appropriate solar and CLARS observing geometries. The single scattering albedo and phase function were obtained from averaged AERONET-Caltech retrievals. The simulated radiance is convolved with the CLARS instrument line shape, which has a full width at half maximum (FWHM) of 0.022 cm^{-1} (Fu et al., 2014).

Appendix A10. Aerosol phase function from AERONET-Caltech

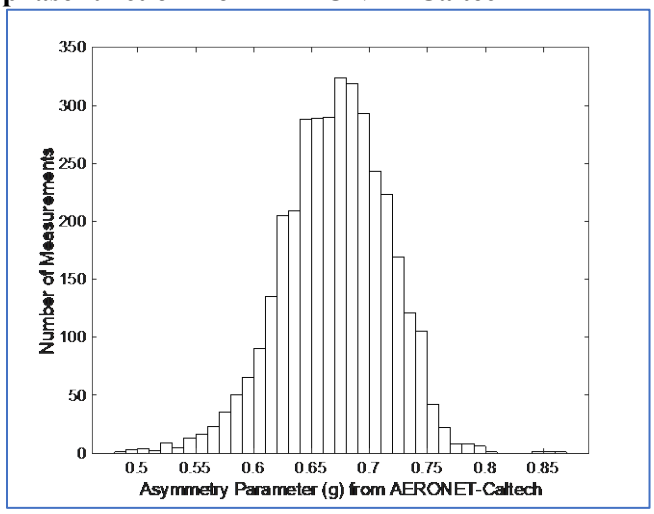

Figure A10. Histogram of asymmetry parameter at 1020 nm from AERONET-Caltech for the time period from 2011 to 2018.

Appendix A11. Variability of aerosol scattering with scattering angle

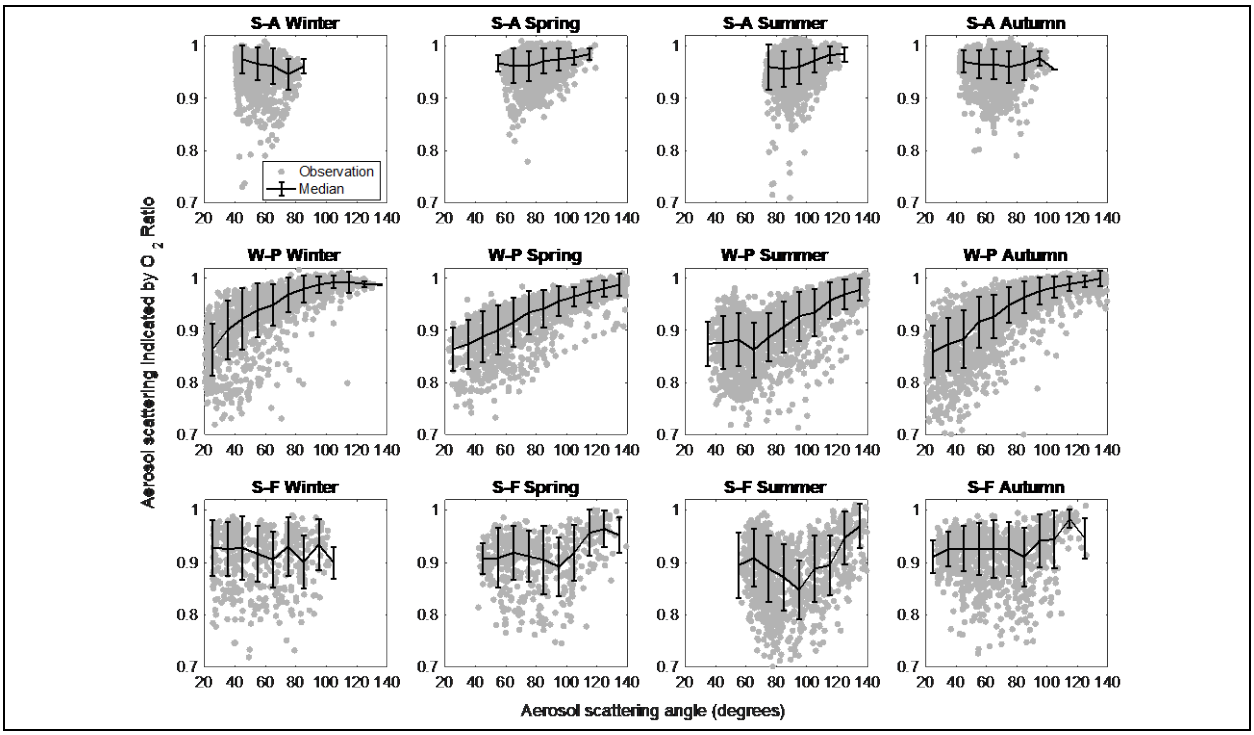

Figure A11. Same as **Figure 6.9** but with scattering angle as the x-axis. Multiyear average of O_2 ratio for the three surface reflection points, Santa Anita (S-A) on the top, West Pasadena (W-P) in the middle, and Santa Fe Dam (S-F) at the bottom from CLARS-FTS data for all seasons (The original measurements are in grey and the hourly mean in black). The corresponding simulation estimates use the 2S-ESS RT model with averaged solar geometry, aerosol optical properties, and surface reflectance. All the data from 2011 to 2018 are used.

Appendix A12. Wind patterns in LA downtown

The wind measurements are collected from a meteorological station at the USC campus in LA downtown (which is in the path of the air pollutant transport between LA downtown and eastern LA where our study sites are located). As shown in (a), there is a shift in wind direction from summer (dominated by eastward winds from the ocean) to winter (dominated by westward winds from inland). This seasonal cycle may explain the large data spread within a year as shown in **Figure 6.10(b)**. However, as shown in (b), the wind speeds (eastward direction) are very stable from year to year and there is no obvious trend detected, which is consistent with our measurements of aerosol phase function trend as shown in **Figure 6.10(c)**.

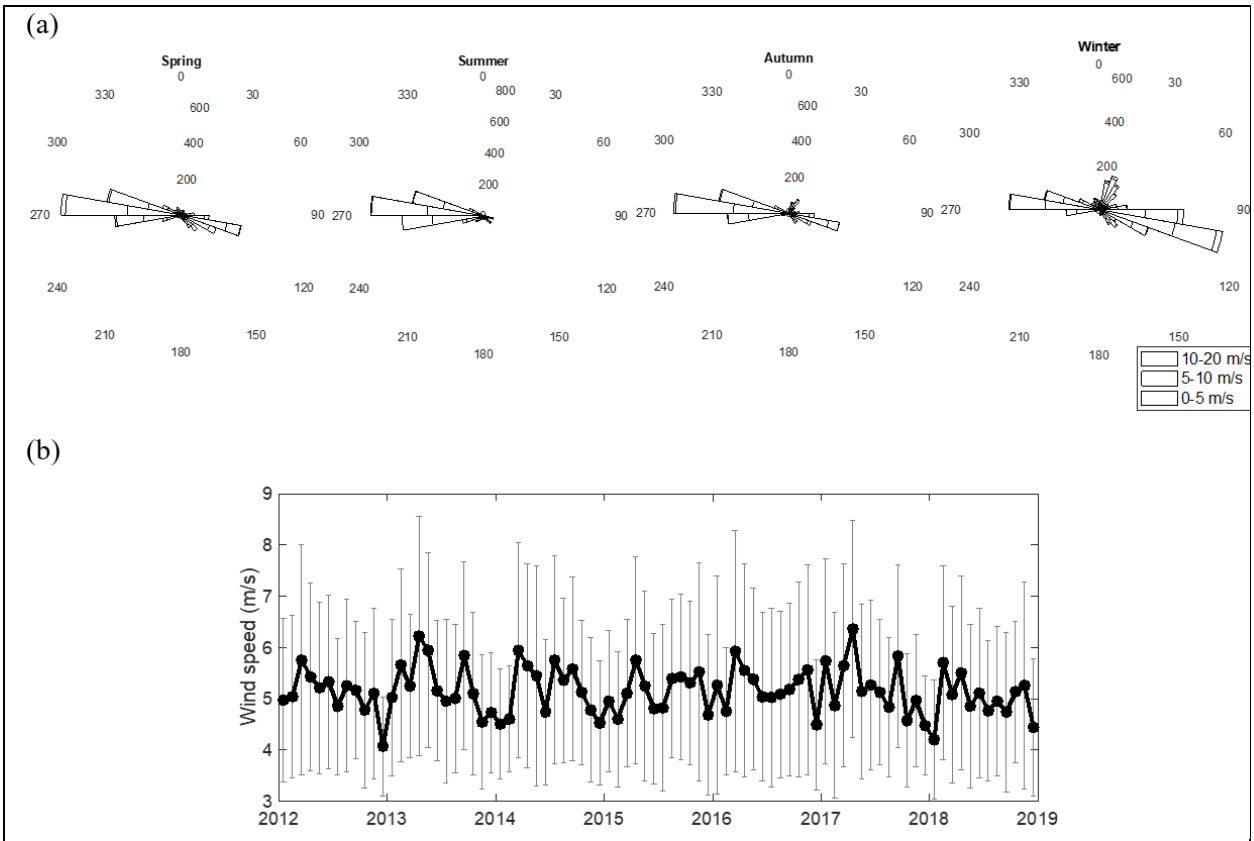

Figure A12. Wind patterns observed by the meteorological station at USC in LA downtown. (a) Wind rose diagrams for four different seasons based on all measurements from 2012 to 2018; (b) Monthly averaged wind speed in the direction between 250 and 290 degrees, which is the wind direction when the wind brings the LA downtown air eastward into the study area of this paper. The gridlines in x-axis marks the beginning of the year. The monthly mean is shown using black dots and the uncertainty (one sigma) is indicated in grey. Wind speed of zero is not considered in the average. These observations at USC can be accessed from the MesoWest datahub hosted by the University of Utah at https://mesowest.utah.edu/. The measurements of wind speed and direction are made every minute.

References

Aben, I., Hasekamp, O., and Hartmann, W. (2007). Uncertainties in the space-based measurements of CO2 columns due to scattering in the Earth's atmosphere, J. Quant. Spectrosc. Radiat. Transfer, 104, 450–459, doi:10.1016/j.jqsrt.2006.09.013.

Avrahami, S., Bohannan, B. J. M., 2009. N_2O emission rates in California meadow soil are influenced by fertilizer level, soil moisture, and community structure of ammonia-oxidixing bacteria. Glob. Chang. Biol. 15, 643-655. https://doi.org/10.1111/j.1365-2486.2008.01727.x.

Arrigo, K. R., van Dijken, G. L., & Strong, A. L. (2015). Environmental controls of marine productivity hot spots around Antarctica. *Journal of Geophysical Research: Oceans*, *120*(8), 5545-5565. https://doi.org/10.1002/2015JC010888.

Battle, M., Bender, M., Sowers, T., Tans P. P., Butler, J. H., Elkins J. W., Ellis J. T., Conway T., Zhang N., Lang P., Clarke A.D., 1996. Atmospheric gas concentrations over the past century measured in air from firn at the South Pole. Nature. 383, 231 – 235. https://doi.org/10.1038/383231a0.

Borbon, A., Gilman, J.B., Kuster, W.C., Grand, N., Chevaillier, S., Colomb, A., et al. 2013. Emission ratios of anthropogenic volatile organic compounds in northern mid-latitude megacities: Observations versus emission inventories in Los Angeles and Paris, J. Geophys. Res. Atmos., 118, 2041–2057, doi:10.1002/jgrd.50059.

Borsdorff, T., Andrasec, J., Hu, H., Aben, I. and Landgraf, J., 2018a. Detection of carbon monoxide pollution from cities and wildfires on regional and urban scales: the benefit of CO column retrievals from SCIAMACHY 2.3 µm measurements under cloudy conditions, Atmos. Meas. Tech., 11(5), 2553–2565, doi: 10.5194/amt-11-2553-2018.

Borsdorff, T., Aan de Brugh, J., Hu, H., Aben, I., Hasekamp, O., and Landgraf, J. 2018b. Measuring carbon monoxide with TROPOMI: First results and a comparison with ECMWF-IFS analysis data, Geophys. Res. Lett., 45, 2826–2832, doi:10.1002/2018GL077045.

Borsdorff, T., aan de Brugh, J., Hu, H., Hasekamp, O., Sussmann, R., Rettinger, M., et al. 2018. Mapping carbon monoxide pollution from space down to city scales with daily global coverage, Atmos. Meas. Tech., 11, 5507–5518, doi: 10.5194/amt-11-5507-2018.

Borsari, V., Assunção, J. V., 2012. Nitrous oxide emissions from gasohol, ethanol, and CNG light duty vehicles. Clim. Change. 111, 519-531. https://doi.org/10.1007/s10584-011-0203-9.

Bouwman, A. F., Boumans, L. J. M., Batjes, N.H., 2002. Emissions of N_2O and NO from fertilized fields: Summary of available measurement data. Global Biogeochem. Cycles, 16 (4), 1058. https://doi.org/10.1029/2001GB001811.

Butz, A., Hasekamp, O. P., Frankenberg, C., and Aben, I. (2009). Retrievals of atmospheric CO_2 from simulated space-borne measurements of backscattered near-infrared sunlight: accounting for aerosol effects, Appl. Opt., 48, 3322–3336, doi:10.1364/AO.48.003322.

Butler, J., Montzka, S., 2020. The NOAA Annual Greenhouse Gas Index (AGGI). NOAA Earth System Research Laboratory. https://www.esrl.noaa.gov/gmd/aggi/aggi.html.

Butterbach-Bahl, K., Baggs, E. M., Dannenmann, M., Kiese, R., Zechmeister-Boltenstern, S., 2013. Nitrous oxide emissions from soils: how well do we understand the processes and their controls? Phil. Trans. R. Soc. B. 368 (1621), 20130122. http://doi.org/10.1098/rstb.2013.0122.

Byrne, B., Strong, K., Colebatch, O., You, Y., Wunch, D., Ars, S., Jones, D.B.A., Fogal, P., Mittermeier R.L., Worthy, D., and Griffith, D.W.T., 2020. Monitoring Urban Greenhouse Gases Using Open-Path

Fourier Transform Spectroscopy. Atmosphere-Ocean 58, 25-45. https://doi.org/10.1080/07055900.2019.1698407

Byrne, B., Jones, D.B.A., Strong, K., Zeng, Z.C., Deng, F. and Liu, J., 2017. Sensitivity of CO_2 surface flux constraints to observational coverage, J. Geophys. Res. Atmos., 122(12), 6672–6694, doi: 10.1002/2016JD026164

California Air Resources Board (CARB) (2011). Greenhouse Gas Emission Inventory - Query Tool for Years 2000-2011. (Avaiable at https://www.arb.ca.gov/app/ghg/2000_2011/ghg_sector.php)

California Energy Commission (CEC) (2018). Online Database for Power Plant Statistical Information. (Accessed July 23, 2018). https://www.energy.ca.gov/almanac/electricity_data/web_qfer/Power_Plant_Statistical_Information.php.

California Legislature (2006). Assembly Bill No. 32. http://www.leginfo.ca.gov/pub/05-06/bill/asm/ab_0001-0050/ab_32_bill_20060927_chaptered.pdf.

California Environmental Protection Agency Air Resources Board, 2016. California's 2000-2014 Greenhouse Gas Emissions Inventory Technical Support Document. https://ww3.arb.ca.gov/cc/inventory/doc/methods_00-14/ghg_inventory_00-14_technical_support_document.pdf.

California Environmental Protection Agency Air Resources Board, 2017. California's 2000-2015 Greenhouse Gas Emissions Inventory Updates Since the 2016 Edition of the Inventory: Supplement to the Technical Support Document. https://ww3.arb.ca.gov/cc/inventory/pubs/reports/2000_2015/ghg_inventory_00-15_method_update_document.pdf.

California Environmental Protection Agency Air Resources Board, 2018. California's 2000-2016 Greenhouse Gas Emissions Inventory Updates Since the 2017 Edition of the Inventory: Supplement to the Technical Support Document. https://ww3.arb.ca.gov/cc/inventory/pubs/reports/2000_2016/ghg_inventory_00-16_method_update_document.pdf.

California Environmental Protection Agency Air Resources Board, 2019a. California Nitrous Oxide Inventory for 2000-2017- by IPCC Category. https://ww3.arb.ca.gov/cc/inventory/data/tables/ghg_inventory_ipcc_sum_2000-17n2o.pdf.

California Environmental Protection Agency Air Resources Board, 2019b. Greenhouse Gas Emissions Inventory. https://www.arb.ca.gov/app/ghg/2000_2017/ghg_sector.php.

Caltrans Performance Measurement System (PeMS), 2019, PeMs data clearing house: Station-Day, available at http://pems.dot.ca.gov/. Accessed date: 4 August 2019.

California Air Resources Board (CARB) (2016), California Emission Inventory Data Almanac, technical report. Available at https://www.arb.ca.gov/app/emsinv/fcemssumcat/fcemssumcat2016.php. Accessed date: 4 August 2019.

Canty, T. and Minschwaner, K., 2002. Seasonal and solar cycle variability of OH in the middle atmosphere. J. Geophys. Res. Atmos., 107(D24).

Chance, K., Liu, X., Suleiman, R.M., Flittner, D.E., Al-Saadi, J. and Janz, S.J., 2013, September. Tropospheric emissions: monitoring of pollution (TEMPO). In Earth Observing Systems XVIII (Vol. 8866, p. 88660D). International Society for Optics and Photonics.

Clerbaux, C., Edwards, D.P., Deeter, M., Emmons, L., Lamarque, J.F., Tie, X.X., et al., 2008. Carbon monoxide pollution from cities and urban areas observed by the Terra/MOPITT mission, Geophys. Res. Lett., 35(3), doi: 10.1029/2007GL032300.

Colarco, P., da Silva, A., Chin, M., and Diehl, T. (2010). Online simulations of global aerosol distributions in the NASA GEOS-4 model and comparisons to satellite and ground based aerosol optical depth, *Journal of Geophysical Research*, 115, D14207, doi:10.1029/2009JD012820.

Computational and Information Systems Laboratory (CISL). 2019. Cheyenne: HPE/SGI ICE XA System (University Community Computing). Boulder, CO: National Center for Atmospheric Research. doi:10.5065/D6RX99HX.

Conley, S., Franco, G., Faloona, I., Blake, D. R., Peischl, J., & Ryerson, T. B. (2016). Methane emissions from the 2015 Aliso Canyon blowout in Los Angeles, CA. *Science*, *351*(6279), 1317-1320. https://doi.org/10.1126/science.aaf2348.

Crisp, D., Miller, C. E., and DeCola, P. L. (2008). NASA Orbiting Carbon Observatory: Measuring the column averaged carbon dioxide mole fraction from space, *Journal of Applied Remote Sensing*, 2(1), 1–14, doi:10.1117/1.2898457.

Cui, Y. Y., Brioude, J., Angevine, W. M., Peischl, J., McKeen, S. A., Kim, S. W., et al. (2017). Top-down estimate of methane emissions in California using a mesoscale inverse modeling technique: The San Joaquin Valley. *Journal of Geophysical Research: Atmospheres*, *122*(6), 3686-3699. https://doi.org/10.1002/2016JD026398.

Cui, Y.Y., Brioude, J., McKeen, S.A., Angevine, W.M., Kim, S.W., Frost, G.J., et al., 2015. Top-down estimate of methane emissions in California using a mesoscale inverse modeling technique: The South Coast Air Basin, J. Geophys. Res. Atmos., 120(13), 6698–6711, doi: 10.1002/2014JD023002.

Daelman, M. R. J., van Voorthuizen, E. M., van Dongen, U. G. J. M., Volcke, E. I. P., van Loosdrecht, M. C. M., 2015. Seasonal and diurnal variability of N_2O emissions from a full scale municipal wastewater treatment plant. Sci. Total Environ. 536, 1-11. https://doi.org/10.1016/j.scitotenv.2015.06.122.

Diner, D.J., Braswell, B.H., Davies, R., Gobron, N., Hu, J., Jin, Y., et al. (2005). The value of multiangle measurements for retrieving structurally and radiatively consistent properties of clouds, aerosols, and surfaces. *Remote Sensing of Environment*, *97*(4), pp.495-518, doi: 10.1016/j.rse.2005.06.006.

Diner, D.J., Boland, S.W., Brauer, M., Bruegge, C., Burke, K.A., et al. (2018). Advances in multiangle satellite remote sensing of speciated airborne particulate matter and association with adverse health effects: from MISR to MAIA. *Journal of Applied Remote Sensing*, *12*(4), doi10.1117/1.JRS.12.042603.

Dubovik, O., Smirnov, A., Holben, B.N., King, M.D., Kaufman, Y.J., Eck, T.F. et al. (2000). Accuracy assessments of aerosol optical properties retrieved from Aerosol Robotic Network (AERONET) Sun and sky radiance measurements. *Journal of Geophysical Research: Atmospheres*, *105*(D8), pp.9791-9806, doi: 10.1029/2000JD900040.

Eldering A, Taylor TE, O'Dell CW, Pavlick R. (2019). The OCO-3 mission: measurement objectives and expected performance based on 1 year of simulated data. *Atmospheric Measurement Techniques*. 12(4):2341-70, doi: 10.5194/amt-12-2341-2019.

Espinosa, W.R., Martins, J.V., Remer, L.A., Puthukkudy, A., Orozco, D. and Dolgos, G. (2018). In situ measurements of angular-dependent light scattering by aerosols over the contiguous United States. *Atmospheric Chemistry and Physics*, *18*(5), pp.3737-3754, doi: 10.5194/acp-18-3737-2018.

Etminan, M., Myhre, G., Highwood, E. J., & Shine, K. P. (2016). Radiative forcing of carbon dioxide, methane, and nitrous oxide: A significant revision of the methane radiative forcing. *Geophysical*

Research Letters, *43*(24). https://doi.org/10.1002/2016GL071930.

European Centre for Medium-Range Weather Forecasts (ECMWF), ERA5 reanalysis dataset, 2019, available at https://www.ecmwf.int/en/forecasts/datasets/reanalysis-datasets/era5. Accessed date: 4 December 2019.

Feng, S., Lauvaux, T., Newman, S., Rao, P., Ahmadov, R., Deng, A., Díaz-Isaac, L.I., Duren, R.M., Fischer, M.L., Gerbig, C. and Gurney, K.R., 2016. Los Angeles megacity: a high-resolution land–atmosphere modelling system for urban CO_2 emissions, Atmos. Chem. Phys., 16(14), doi: 10.5194/acp-16-9019-2016

Fischer, M. L., Chan, W. R., Delp, W., Jeong, S., Rapp, V., & Zhu, Z. (2018). An Estimate of Natural Gas Methane Emissions from California Homes. *Environmental science & technology*, *52*(17), 10205-10213. https://doi.org/10.1021/acs.est.8b03217.

Frankenberg, C., Hasekamp, O., O'Dell, C., Sanghavi, S., Butz, A., and Worden, J. (2012). Aerosol information content analysis of multi-angle high spectral resolution measurements and its benefit for high accuracy greenhouse gas retrievals, Atmos. Meas. Tech., 5, 1809–1821, https://doi.org/10.5194/amt-5-1809-2012.

Fu, D., Pongetti, T. J., Blavier, J.-F. L., Crawford, T. J., Manatt, K. S., Toon, G. C., Wong, K. W., Sander, S. P., 2014. Near-infrared remote sensing of Los Angeles trace gas distributions from a mountaintop site. Atmos. Meas. Tech. 7, 713–729. https://doi.org/10.5194/amt-7-713-2014.

Gamnitzer, U., Karstens, U., Kromer, B., Neubert, R.E., Meijer, H.A., Schroeder, H. and Levin, I., 2006. Carbon monoxide: A quantitative tracer for fossil fuel CO2? J. Geophys. Res. Atmos., 111(D22), doi: 10.1029/2005JD006966

Graham, L. A., Belise, S. L., Rieger, P., 2009. Nitrous oxide emissions from light duty vehicles. Atm. Environ. 43, 2031- 2044. https://doi.org/10.1016/j.atmosenv.2009.01.002

Grell, G. A., Peckham, S. E., Schmitz, R., McKeen, S. A., Frost, G., Skamarock, W. C., and Eder, B., 2005. Fully Coupled "Online" Chemistry within the WRF Model, Atmos. Environ., 39, 6957–6975, doi: 10.1016/j.atmosenv.2005.04.027.

Griffith, D.W., Pohler, D., Schmitt, S., S Hammer, S., Vardag, S. and Platt, U. (2018). Long open-path measurements of greenhouse gases in air using near-infrared Fourier transform spectroscopy. *Atmospheric Measurement Techniques*, 11 (3), 1549-1563, doi: 10.5194/amt-11-1549-2018.

Grömping, U. (2006). Relative importance for linear regression in R: the package relaimpo. *Journal of statistical software*, *17*(1), 1-27. https://doi.org/10.18637/jss.v017.i01.

Guo, Q., Hu, M., Guo, S., Wu, Z., Peng, J. and Wu, Y., 2017. The variability in the relationship between black carbon and carbon monoxide over the eastern coast of China: BC aging during transport, Atmos. Chem. Phys., 17(17), 10395, doi: 10.5194/acp-17-10395-2017.

Guerlet, S., Butz, A., Schepers, D., Basu, S., Hasekamp, O. P., Kuze, A., et al. (2013). Impact of aerosol and thin cirrus on retrieving and validating XCO2 from GOSAT shortwave infrared measurements, J. Geophys. Res.-Atmos., 118, 4887–4905, doi:10.1002/jgrd.50332.

Gurney, K. R., Razlivanov, I., Song, Y., Zhou, Y., Benes, B., & Abdul-Massih, M. (2012). Quantification of fossil fuel CO_2 emissions on the building/street scale for a large US city. *Environmental science & technology*, 46(21), 12194-12202. https://doi.org/10.1021/es3011282.

Gurney, K. R., Patarasuk, R., Liang, J., Song, Y., O'Keeffe, D., Rao, P., Whetstone, J. R., Duren, R. M., Eldering, A., and Miller, C., 2019. The Hestia fossil fuel CO_2 emissions data product for the Los Angeles megacity (Hestia-LA), Earth Syst. Sci. Data. 11, 1309–1335. https://doi.org/10.5194/essd-11-1309-2019.

He, L., Zeng, Z.-C., Pongetti, T., Wong, C., Liang, J., Gurney, K. R., Newman, S., Yadav, V., Verhulst, K., Miller, C. E., Duren, R., Frankenberg, C., Wennberg, P. O., Shia, R.-L., Yung, Y. L., Sander, S. P., 2019. Atmospheric methane emissions correlate with natural gas consumption from residential and commercial sectors in Los Angeles. Geophys. Res, Lett., 46, 8563–8571. https:// doi.org/10.1029/2019GL083400.

Heft-Neal, S., Burney, J., Bendavid, E. and Burke, M. (2018). Robust relationship between air quality and infant mortality in Africa. *Nature*, *559*(7713), p.254-258, doi: 10.1038/s41586-018-0263-3.

Henyey, L. G. and Greenstein, T. L. (1941). Diffuse radiation in the galaxy, *Astrophysical Journal*, 93, 70–83.

Hedelius, J. K., Liu, J., Oda, T., Maksyutov, S., Roehl, C. M., Iraci, L. T., et al. (2018). Southern California megacity CO_2, CH_4, and CO flux estimates using ground-and space-based remote sensing and a Lagrangian model. *Atmospheric Chemistry and Physics*, *18*(22), 16271-16291. https://doi.org/10.5194/acp-18-16271-2018.

Hopkins, F. M., Kort, E. A., Bush, S. E., Ehleringer, J. R., Lai, C. T., Blake, D. R., & Randerson, J. T. (2016). Spatial patterns and source attribution of urban methane in the Los Angeles Basin. *Journal of Geophysical Research: Atmospheres*, *121*(5), 2490-2507. https://doi.org/10.1002/2015JD024429.

Holloway, T., Levy, H., and Kasibhatla, P., 2000. Global distribution of carbon monoxide, J. Geophys. Res.-Atmos., 105, 12123–12147, doi:10.1029/1999jd901173.

Holben, B. N., Eck, T. F., Slutsker, I., Tanre, D., Buis, J. P., Setzer, A., et al., 1998. AERONET – A federated instrument network and data archive for aerosol characterization, Remote Sens. Environ., 66, 1–16, doi: 10.1016/S0034-4257(98)00031-5.

Horwath, W. R., 2012. Assessment of Baseline Nitrous Oxide Emissions in California Cropping Systems. California Air Resources Board. Contact No. 08-324. https://ww2.arb.ca.gov/sites/default/files/classic//research/apr/past/08-324.pdf.

Hsu, Y. K., VanCuren, T., Park, S., Jakober, C., Herner, J., FitzGibbon, M., et al. (2010). Methane emissions inventory verification in southern California. *Atmospheric Environment*, *44*(1), 1-7. https://doi.org/10.1016/j.atmosenv.2009.10.002

Huai, T., Dubrin, T. D., Miller, J. W., Norbeck, J. M., 2004. Estimates of emission rates of nitrous oxide from light-duty vehicles using different chassis dynamometer test cycles. Atm. Environ. 38, 6621 – 6629. https://doi.org/10.1016/j.atmosenv.2004.07.007.

Ignatov, A. (1997). Estimation of the aerosol phase function in backscatter from simultaneous satellite and sun-photometer measurements. *Journal of Applied Meteorology*, *36*(6), pp.688-694.

Jeong, S., Cui, X., Blake, D. R., Miller, B., Montzka, S. A., Andrews, A., et al. (2017). Estimating methane emissions from biological and fossil-fuel sources in the San Francisco Bay Area. *Geophysical Research Letters*, *44*(1), 486-495. https://doi.org/10.1002/2016GL071794.

Jiang, Z., Worden, J. R., Worden, H., Deeter, M., Jones, D. B. A., Arellano, A. F., et al., 2017. A 15-year record of CO emissions constrained by MOPITT CO observations, Atmos. Chem. Phys., 17, 4565–4583, doi:10.5194/acp-17-4565-2017.

Jiang, Z., McDonald, B.C., Worden, H., Worden, J.R., Miyazaki, K., Qu, Z., et al., 2018. Unexpected slowdown of US pollutant emission reduction in the past decade, Proc. Natl. Acad. Sci. USA, 115(20), 5099–5104, 10.1073/pnas.1801191115.

Jiang, X., Ku, W. L., Shia, R. L., Li, Q., Elkins, J. W., Prinn, R. G., Yung, Y. L., 2007. Seasonal cycle of N_2O: Analysis of data. Global Biogeochem. Cycles. 21, GB1006. https://doi.org/10.1029/2006GB002691.

Jones, A. K., Jones, D. L., & Cross, P. (2014). The carbon footprint of lamb: sources of variation and opportunities for mitigation. *Agricultural Systems*, *123*, 97-107. https://doi.org/10.1016/J.AGSY.2013.09.006.

Kahn, R., Banerjee, P., & McDonald, D. (2001). The sensitivity of multiangle imaging to natural mixtures of aerosols over ocean. *Journal of Geophysical Research*, 106, 18219–18238.

Kalnay, E., Kanamitsu, M., Kistler, R., Collins, W., Deaven, D., Gandin, L., et al., 1996. The NCEP/NCAR 40-year reanalysis project, B. Am. Meteorol. Soc., 77, 437–471, doi: 10.1175/1520-0477(1996)077<0437:TNYRP>2.0.CO;2.

Kaufman, Y.J., Gitelson, A., Karnieli, A., Ganor, E., Fraser, R.S., Nakajima, T., et al. (1994). Size distribution and scattering phase function of aerosol particles retrieved from sky brightness measurements. *Journal of Geophysical Research: Atmospheres*, *99*(D5), pp.10341-10356.

Kim, S.-W., McDonald, B.C., Baidar, S., Brown, S.S., Dube, B., Ferrare, R.A., et al., 2016. Modeling the weekly cycle of NOx and CO emissions and their impacts on O_3 in the Los Angeles-South Coast Air Basin during the CalNex 2010 field campaign, J. Geophys. Res. Atmos., 121, 1340– 1360, doi: 10.1002/2015JD024292.

Kim, J., Lieschke, K.J. and Newman, C., 2018. The Berkeley atmospheric CO2 observation network: Field calibration and evaluation of low-cost air quality sensors, Atmos. Meas. Tech., 11(4), 1937–1946, doi: 10.5194/amt-11-1937-2018.

Kimbrough, D. E. (2017). Local Climate Change in Pasadena, Calif., and the Impact on Streamflow. *Journal-American Water Works Association*, *109*(10), E416-E425. https://doi.org/10.5942/jawwa.2017.109.0114.

Kokhanovsky, A.A. (1998). Variability of the phase function of atmospheric aerosols at large scattering angles. *Journal of the atmospheric sciences*, *55*(3), pp.314-320.

Kort, E.A., Frankenberg, C., Miller, C.E. and Oda, T., 2012. Space-based observations of megacity carbon dioxide, Geophys. Res. Lett, 39(17), doi: 10.1029/2012GL052738.

Lamb, B. K., Cambaliza, M. O., Davis, K. J., Edburg, S. L., Ferrara, T. W., Floerchinger, C., et al. (2016). Direct and indirect measurements and modeling of methane emissions in Indianapolis, Indiana. *Environmental science & technology*, *50*(16), 8910-8917. https://doi.org/10.1021/acs.est.6b01198.

Lauvaux, T., Pannekoucke, O., Sarrat, C., Chevallier, F., Ciais, P., Noilhan, J., et al., 2009. Structure of the transport uncertainty in mesoscale inversions of CO2 sources and sinks using ensemble model simulations, Biogeosciences, 6, 1089–1102, doi:10.5194/bg-6-1089-2009.

Leshchishina, O., Kassi, S., Gordon, I.E., Rothman, L.S., Wang, L. and Campargue, A., 2010. High sensitivity CRDS of the a1Δg− X3Σg− band of oxygen near 1.27 μm: Extended observations, quadrupole transitions, hot bands and minor isotopologues. *Journal of Quantitative Spectroscopy and Radiative Transfer*, 111(15), pp.2236-2245.

Li, Y., Zhang, J., Sailor, D.J. and Ban-Weiss, G.A., 2019. Effects of urbanization on regional meteorology and air quality in Southern California, Atmos. Chem. Phys., 19(7), 4439–4457, doi: 10.5194/acp-19-4439-2019.

Lindeman, R. H. (1980). *Introduction to bivariate and multivariate analysis* (No. 04; QA278, L553.).

Lin, J.C., Mitchell, L., Crosman, E., Mendoza, D.L., Buchert, M., Bares, R., Fasoli, B., Bowling, D.R., Pataki, D., Catharine, D. and Strong, C., 2018. CO_2 and carbon emissions from cities: Linkages to air

quality, socioeconomic activity, and stakeholders in the Salt Lake City urban area, B. Am. Meteorol. Soc., 99(11), 2325–2339, doi: 10.1175/BAMS-D-17-0037.1.

Liao, T., Camp, C. D. , Yung, Y. L., 2004. The seasonal cycle of N_2O. Geophys. Res. Lett. 31, L17108. https://doi.org/10.1029/2004GL020345.

Liou, K.N. (2002). *An introduction to atmospheric radiation* (Vol. 84). Elsevier.

Lu, R. and Turco, R.P., 1995. Air pollutant transport in a coastal environment—II. Three-dimensional simulations over Los Angeles basin, Atmos. Environ., 29(13), 1499–1518, doi: 10.1016/1352-2310(95)00015-Q.

Lu, R. and Turco, R.P. (1994). Air pollutant transport in a coastal environment. Part I: Two-dimensional simulations of sea-breeze and mountain effects. *Journal of the atmospheric sciences*, *51*(15), pp.2285-2308.

Machida, T., Nakazawa, T., Fujii, Y., Aoki, S., Watanabe, O., 1995. Increase in the atmospheric nitrous oxide concentration during the last 250 years. *Geophys. Res. Lett. 22, 2921-2924.* https://doi.org/10.1029/95GL02822.

Marr, L.C. and Harley, R.A., 2002. Modeling the effect of weekday−weekend differences in motor vehicle emissions on photochemical air pollution in central California, Environ Sci Technol., 36(19), 4099–4106, doi: 10.1021/es020629x.

Mays KL, Shepson, P.B., Stirm, B.H., Karion, A., Sweeney, C. and Gurney, K.R., 2009. Aircraft-based measurements of the carbon footprint of Indianapolis, Environ. Sci. Technol., 43, 7816–7823, doi: 10.1021/es901326b.

McKain K, et al. (2012) Assessment of ground-based atmospheric observations for verification of greenhouse gas emissions from an urban region, Proc. Natl. Acad. Sci. USA, 109, 8423–8428, doi: 10.1073/pnas.1116645109.

McKain, K., Down, A., Raciti, S. M., Budney, J., Hutyra, L. R., Floerchinger, C., et al. (2015). Methane emissions from natural gas infrastructure and use in the urban region of Boston, Massachusetts. *Proceedings of the National Academy of Sciences*, *112*(7), 1941-1946. https://doi.org/10.1073/pnas.1416261112.

Moore, B., Crowell, S., Rayner, P., Kumer, J., O'Dell, C., O'Brien, D., et al., 2018. The potential of the Geostationary Carbon Cycle Observatory (GeoCarb) to provide multi-scale constraints on the carbon cycle in the Americas, Front. Environ. Sci., 6, 109, doi: 10.3389/fenvs.2018.00109.

Moran, D., Kanemoto, K., Jiborn, M., Wood, R., Többen, J. and Seto, K.C., 2018. Carbon footprints of 13 000 cities, Environ. Res. Lett., 13(6), 064041, doi: 10.1088/1748-9326/aac72a.

Montzka, S.A., Dlugokenchy, E. J., Butler, J.H., 2011. Non-CO_2 greenhouse gases and climate change. Nature. 476, 43-50. https://doi.org/10.1038/nature10322.

Morgan, C. G., Allen, M., Liang, M. C., Shia, R. L., Blake, G. A., Yung, Y. L., 2004. Isotopic fractionation of nitrous oxide in the stratosphere: Comparison between model and observations. J. Geophys. Res. Atmos. 109, D04305. https://doi.org/10.1029/2003JD003402.

Mueller, K., Yadav, V., Lopez-Coto, I., Karion, A., Gourdji, S., Martin, C. and Whetstone, J., 2018. Siting background towers to characterize incoming air for urban greenhouse gas estimation: A case study in the Washington, DC/Baltimore area, J. Geophys. Res. Atmos., 123(5), 2910–2926, doi: 10.1002/2017JD027364.

Newman, S., Jeong, S., Fischer, M.L., Xu, X., Haman, C.L., Lefer, B., et al., 2013. Diurnal tracking of anthropogenic CO_2 emissions in the Los Angeles basin megacity during spring 2010, Atmos. Chem. Phys., 13, 4359–4372, doi:10.5194/acp-13-4359-2013.

Nelson, R. R., O'Dell, C. W., Taylor, T. E., Mandrake, L., and Smyth, M. (2016). The potential of clear-sky carbon dioxide satellite retrievals, Atmos. Meas. Tech., 9, 1671-1684, https://doi.org/10.5194/amt-9-1671-2016.

Nelson, R. R. and O'Dell, C. W. (2019). The impact of improved aerosol priors on near-infrared measurements of carbon dioxide, Atmos. Meas. Tech., 12, 1495-1512, https://doi.org/10.5194/amt-12-1495-2019.

Nevison, C. D., Kinnison, D. E., Weiss, R. F., 2004. Stratospheric influences on the tropospheric seasonal cycles of nitrous oxide and chlorofluorocarbons. Geophys. Res. Lett. 31, L20103. https://doi.org/10.1029/2004GL020398

Nevison, C. D., Mahowalk, N. M., Weiss, R. F., Prinn, R. G., 2007. Interannual and seasonal variability in atmospheric N_2O. Global Biogeochem. Cycles. 21, GB3017. https://doi.org/10.1029/2006GB002755

National Oceanic and Atmospheric Administration, 2019. Earth System Research Laboratory Global Monitoring Division (ESRL GMD) projects at Mt. Wilson Observatory. (Accessed October 31, 2020. http://www.esrl.noaa.gov/gmd/dv/site/MWO.html

O'Dell, C. W., Connor, B., Bösch, H., O'Brien, D., Frankenberg, C., Castano, R., et al. (2012). The ACOS CO_2 retrieval algorithm – Part 1: Description and validation against synthetic observations. *Atmospheric Measurement Techniques*, 5, 99–121, doi:10.5194/amt-5-99-2012.

Peischl, J., Ryerson, T. B., Brioude, J., Aikin, K. C., Andrews, A. E., Atlas, E., et al. (2013). Quantifying sources of methane using light alkanes in the Los Angeles basin, California. *Journal of Geophysical Research: Atmospheres*, *118*(10), 4974-4990. https://doi.org/10.1002/jgrd.50413.

Pommier, M., McLinden, C. A., and Deeter, M., 2013. Relative changes in CO emissions over megacities based on observations from space, Geophys. Res. Lett., 40, 3766–3771, doi:10.1002/grl.50704.

Prinn, R. G., Cunnold, D. M., Rasmussen, R., Simmonds, P. G., Alyea, F. N., Crawford, A., Fraser, P. J., Rosen, R. D., 1990. Atmospheric emissions and trends of nitrous oxide deduced from 10 years of ALE/GAGE data. J.Geophys.Res. 95,18,369-18,385. https://doi.org/10.1029/JD095iD11p18369.

Prinn, R. G., Weiss, R. F., Fraser, P. J., Simmonds, P. G., Cunnold, D. M., Alyea, F. N., O'Doherty, S., Salameh, P., Miller, B. R., Huang, J., Wang, R. H. J., Hartley, D. E., Harth, C., Steele, L. P., Sturrock, G., Midgley, P. M., McCulloch, A., 2000. A history of chemically and radiatively im;ortant gases in air deduced from ALE/GAGE/AGAGE. J. Geophys. Res. 105, 17751-17792. https://doi.org/10.1029/2000JD900141.

Raphael, M.N., 2003. The Santa Ana winds of California, Earth Interactions, 7(8), 1–13, doi: 10.1175/1087-3562(2003)007<0001:TSAWOC>2.0.CO;2.

Rinsland, C.P., Luo, M., Logan, J.A., Beer, R., Worden, H., Kulawik, S.S., et al., 2006. Nadir measurements of carbon monoxide distributions by the Tropospheric Emission Spectrometer instrument onboard the Aura Spacecraft: Overview of analysis approach and examples of initial results, Geophys. Res. Lett., 33(22), doi: 10.1029/2006GL027000.

Rienecker, M. M., Suarez, M. J., Gelaro, R., Todling, R., Bacmeister, J., Liu, R., et al. (2011). MERRA: NASA's Modern-Era Retrospective Analysis for Research and Applications, J. Climate, 24, 3624–3648.

Rodgers, C. D. (2000). *Inverse Methods for Atmospheric Sounding: Theory and Practice*, World Scientific, Singapore.

Rothman, L. S., Gordon, I. E., Barbe, A., Benner, D. C., Bernath, P. E., Birk, M. (2009). The HITRAN 2008 molecular spectroscopic database, *Journal of Quantitative Spectroscopy & Radiative Transfer*, 110, 533–572, doi:10.1016/j.jqsrt.2009.02.013.

Sanders, A. F. J., de Haan, J. F., Sneep, M., Apituley, A., Stammes, P., Vieitez, M. O., et al. (2015). Evaluation of the operational Aerosol Layer Height retrieval algorithm for Sentinel-5 Precursor: application to O_2 A band observations from GOME-2A, *Atmospheric Measurement Techniques*, 8, 4947-4977, doi: 10.5194/amt-8-4947-2015.

Seinfeld, J. and Pandis, S. (2006). Atmospheric chemistry and physics: from air pollution to climate change, Wiley, Inc., New Jersey, USA, p. 1224.

Southern California Gas Company (SoCalGas) (2018). Online Gas Energy Usage Database (2018). (Accessed June 20, 2018). https://energydatarequest.socalgas.com/.

Spivakovsky, C.M., Logan, J.A., Montzka, S.A., Balkanski, Y.J., Foreman-Fowler, M., Jones, D.B.A., Horowitz, L.W., Fusco, A.C., Brenninkmeijer, C.A.M., Prather, M.J. and Wofsy, S.C., 2000. Three-dimensional climatological distribution of tropospheric OH: Update and evaluation. J. Geophys. Res. Atmos., 105(D7), 8931–8980, doi: 10.1029/1999JD901006.

Spurr, R. J. D., and Natraj, V., 2011. A linearized 2-stream radiative transfer code for fast approximation of multiple-scatter fields, J. Quant. Spectrosc. Radiat. Transfer, 112(16), 2630–2637, doi:10.1016/j.jqsrt.2011.06.014.

Stocker, T. ed., 2014. *Climate change 2013: the physical science basis: Working Group I contribution to the Fifth assessment report of the Intergovernmental Panel on Climate Change*. Cambridge University Press.

Strong, C., Stwertka, C., Bowling, D.R., Stephens, B.B., Ehleringer, J.R., 2011. Urban carbon dioxide cycles within the Salt Lake Valley: A multiple-box model validated by observations, J Geophys Res, 116, D15307, doi: 10.1029/2011JD015693.

Stein, L. Y., Yung, Y. L., 2003. Production, Isotropic Composition, and Atmospheric Fate of Biologically Produced Nitrous Oxide. Annu. Rev. Earth Planet Sci. 31, 329-356. https://doi.org/10.1146/annurev.earth.31.110502.080901

Syakila, A., Kroeze, C., 2011. The global nitrous oxide budget revisited, Greenhouse Gas Measurement and Management, 1, 17–26. https://doi.org/10.3763/ghgmm.2010.0007.

Tanaka, T., Yates, E., Iraci, L. T., Johnson, M. S., Gore, W., Tadić, J. M., et al. (2016). Two-Year Comparison of Airborne Measurements of CO_2 and CH_4 With GOSAT at Railroad Valley, Nevada. *IEEE Transactions on Geoscience and Remote Sensing*, *54*(8), 4367-4375. https://doi.org/10.1109/TGRS.2016.2539973.

Taylor, T. E., O'Dell, C. W., Frankenberg, C., Partain, P. T., Cronk, H. Q., Savtchenko, A., et al. (2016). Orbiting Carbon Observatory-2 (OCO-2) cloud screening algorithms: Validation against collocated MODIS and CALIOP data. *Atmospheric Measurement Techniques*, *9*(3), pp.973-989.

Thompson, J. E., Hayes, P. L., Jimenez, J. L., Adachi, K., Zhang, X., Liu, J., et al. (2012). Aerosol optical properties at Pasadena, CA during CalNex 2010, *Atmospheric Environment*, 55, pp.190-200, doi:10.1016/j.atmosenv.2012.03.011.

Toon, G. C., Farmer, C. B., Schaper, P. W., Lowes, L. L., and Norton, R. H. (1992). Composition measurements of the 1989 Arctic winter stratosphere by airborne infrared solar absorption spectroscopy, *Journal of Geophysical Research*, 97, 7939–7961, 1992.

Townsend-Small, A., Pataki, D. E., Czimczik, C I., Tyler, S. C., 2011. Nitrous oxide emissions and isotopic composiiont in urban and agricultural systems in Southern California. J. Geophys. Res. Biogeosci. 116, G01013. https://doi.org/10.2134/jeq2011.0059

Townsend-Small A, Prokopenko,M.G., and Berelson, W. M., 2014. Nitrous oxide cycling in the water column and sediments of the oxygen minimum zone, eastern subtropical North Pacific, Southern California and Northern Mexico. J. Geophys. Res. Oceans. 119, 3158-3170. https://doi.org/10.1002/2013JC009580

Thompson, T.M., Butler, J.H., Daube, B.C., Dutton, G.S., Elkins, J.W., Hall, B.D., Hurst, D.F., King, D.B., Kline, E.S., Lafleur, B.G., Lind, J., Lovitz, S., Mondeel, D. J., Montzka, S.A., Moore, F.L., Nance, J.D., Neu, J.L., Romashkin, P.A., Scheffer, A., Snible, W.J., 2004. Halocarbons and other atmospheric trace species. NOAA CMDL Summary Report no. 27, 115–135.

Turnbull, J.C., Sweeney, C., Karion, A., Newberger, T., Lehman, S.J., Tans, P.P., et al., 2015. Toward quantification and source sector identification of fossil fuel CO_2 emissions from an urban area: Results from the INFLUX experiment, J. Geophys. Res. Atmos., 120(1), 292–312, doi: 10.1002/2014JD022555.

U.S. Energy Information Administration (EIA) (2018). Online Database for Electricity. Accessed May 20, 2018. https://www.eia.gov/electricity/data/state/.

U.S. Environmental Protection Agency (EPA) (2018). Inventory of U.S. Greenhouse Gas Emissions and Sinks. Report No. EPA 430-R-18-003, Annex 2013, Washington, D.C. (Available at https://www.epa.gov/ghgemissions/inventory-us-greenhouse-gas-emissions-and-sinks-1990-2016)

US Environmental Protection Agency (EPA), National Emission Inventory (NEI) for 2011, available at https://www.epa.gov/air-emissions-inventories/national-emissions-inventory-nei. Accessed date: 4 August 2019.

United States Environmental Protection Agency, 2019. Overview of Greenhouse Gases. https://www.epa.gov/ghgemissions/overview-greenhouse-gases.

Vasilaki, V., Massara, T. M., Stanchev, P., Fatone, F., Katsou, E., 2019. A decade of nitrous oxide (N_2O) monitoring in full-scale wastewater treatment processes: A critical review. Water Res. 161, 392-412. https://doi.org/10.1016/j.watres.2019.04.022.

Verhulst, K. R., Karion, A., Kim, J., Salameh, P. K., Keeling, R. F., Newman, S., et al., 2017. Carbon dioxide and methane measurements from the Los Angeles Megacity Carbon Project – Part 1: calibration, urban enhancements, and uncertainty estimates, Atmos. Chem. Phys., 17, 8313–8341, doi: 10.5194/acp-17-8313-2017.

Ware, J., Kort, E. A., DeCola, P., & Duren, R. (2016). Aerosol lidar observations of atmospheric mixing in Los Angeles: Climatology and implications for greenhouse gas observations. *Journal of Geophysical Research: Atmospheres*, *121*(16), 9862-9878. https://doi.org/10.1002/2016JD024953

Wennberg, P. O., Mui, W., Wunch, D., Kort, E. A., Blake, D. R., Atlas, E. L., et al. (2012). On the sources of methane to the Los Angeles atmosphere. *Environmental science & technology*, *46*(17), 9282-9289. https://doi.org/10.1021/es301138y.

Western Regional Climate Center. Climate Historical Summaries. (2019). Online Database for Los Angeles DWTN USC campus (Accessed April 8, 2019). https://wrcc.dri.edu/cgi-bin/cliMAIN.pl?ca5115.

World Meteorological Organization, 2019. WMO Greenhouse Gas Bulletin. No. 15. https://library.wmo.int/index.php?lvl=notice_display&id=21620#.Xtf9PZ5KhN0.

Wong, K. W., Fu, D., Pongetti, T. J., Newman, S., Kort, E. A., Duren, R., Hsu, Y.-K., Miller, C. E., Yung, Y. L., Sander, S. P., 2015. Mapping CH_4: CO_2 ratios in Los Angeles with CLARS- FTS from Mount Wilson, California, Atmos. Chem. Phys. 15, 241–252. https://doi.org/10.5194/acp-15-241-2015.

Wong, C. K., Pongetti, T. J., Oda, T., Rao, P., Gurney, K. R., Newman, S., Duren, R. M., Miller, C. E., Yung, Y. L., Sander, S. P. 2016. Monthly trends in methane emissions in Los Angeles from 2011 to 2015 inferred by CLARS-FTS observations. Atmos. Chem. Phys. 16, 13121-13130. https://doi.org/10.5194/acp-16-13121-2016.

Wu, Z., He, H. S., Liang, Y., Cai, L., & Lewis, B. J. (2013). Determining relative contributions of vegetation and topography to burn severity from LANDSAT imagery. *Environmental management*, *52*(4), 821-836. https://doi.org/10.1007/s00267-013-0128-3.

Wunch, D., Wennberg, P. O., Toon, G. C., Keppel-Aleks, G., Yavin, Y. G., 2009. Emissions of greenhouse gases from a North American megacity. Geophys. Res. Lett. 36, L15810. https://doi.org/10.1029/2009GL039825.

Wunch, D., Toon, G. C., Wennberg, P. O., Wofsy, S. C., Stephens, B. B., Fischer, M. L., Uchino, O., Abshire, J. B., Bernath, P., Biraud, S. C., Blavier, J.-F. L., Boone, C., Bowman, K. P., Browell, E. V., Campos, T., Connor, B. J., Daube, B. C., Deutscher, N. M., Diao, M., Elkins, J. W., Gerbig, C., Gottlieb, E., Griffith, D. W. T., Hurst, D. F., Jiménez, R., Keppel-Aleks, G., Kort, E. A., Macatangay, R., Machida, T., Matsueda, H., Moore, F., Morino, I., Park, S., Robinson, J., Roehl, C. M., Sawa, Y., Sherlock, V., Sweeney, C., Tanaka, T., and Zondlo, M. A., 2010. Calibration of the Total Carbon Column Observing Network using aircraft profile data. Atmos. Meas. Tech. 3, 1351–1362. https://doi.org/10.5194/amt-3-1351-2010, 2010

Wunch, D., Toon, G. C., Blavier, J.-F. L., Washenfelder, R., Notholt, J., Connor, B. J., et al. (2011). The Total Carbon Column Observing Network, *Philosophical Transactions of the Royal Society A*, 369, 2087–2112, doi:10.1098/rsta.2010.0240.

Wunch, D., Toon, G. C., Hedelius, J. K., Vizenor, N., Roehl, C. M., Saad, K. M., et al. (2016). Quantifying the loss of processed natural gas within California's South Coast Air Basin using long-term measurements of ethane and methane. *Atmospheric Chemistry and Physics*, *16*(22), 14091. https://doi.org/10.5194/acp-16-14091-2016.

Wunderlin, P., Mohn, J., Joss, A., Emmenegger, L., Siegrist, H., 2011. Mechanisms of N_2O production in biological wastewater treatment under nitrifying and denitrifying conditions. Water Res. 46, 1027-1037. https://doi.org/10.1016/j.watres.2011.11.080.

Xiang, B., Miller, S. M., Kort, E. A., Santoni, G. W., Daube, B. C., Commane, R., Angevine, W. M., Ryerson, T. B, Trainer, M. K., Andrews, A. E., Nehrkorn, T., Tian, H., Wofsy, S. C., 2013. Nitrous oxide (N_2O) emissions from California based on 2010 CalNex airborne measurements. J. Geophys. Res. Atmos. 118, 2809-2820. https://doi.org/10.1002/jgrd.50189.

Xi, X., Natraj, V., Shia, R. L., Luo, M., Zhang, Q., Newman, S., et al. (2015). Simulated retrievals for the remote sensing of CO_2, CH_4, CO, and H_2O from geostationary orbit, *Atmospheric Measurement Techniques*, 8, 4817-4830, doi:10.5194/amt-8- 4817-2015.

Xu, F., van Harten, G., Diner, D. J., Kalashnikova, O. V., Seidel, F. C., Bruegge, C. J., et al. (2017). Coupled retrieval of aerosol properties and land surface reflection using the Airborne Multiangle SpectroPolarimetric Imager (AirMSPI), *Journal of Geophysical Research*, 122, 7004-7026.

Xu, F., Dubovik, O., Zhai, P.-W., Diner, D. J., Kalashnikova, O. V., Seidel, F. C., et al. (2016). Joint retrieval of aerosol and water-leaving radiance from multi-spectral, multi-angular and polarimetric measurements over ocean, *Atmospheric Measurement Techniques,* 9, 2877-2907.

Yamamoto, G., and Wark, D. Q. (1961). Discussion of the letter by R.A. Hanel, "Determination of cloud altitude from a satellite". *Journal of Geophysical Research*, 66, 3596.

Yadav, V., Duren, R., Mueller, K., Verhulst, K. R., Nehrkorn, T., Kim, J., et al. (2019). Spatio-temporally resolved methane fluxes from the Los Angeles Megacity. *Journal of Geophysical Research: Atmospheres*, *124*(9), 5131-5148. https://doi.org/10.1029/2018JD029224.

Yang, J., Wang, Z.-H., Chen, F., Miao, S., Tewari, M., Voogt, J. A., and Myint, S., 2015. Enhancing hydrologic modelling in the Coupled Weather Research and Forecasting–Urban Modelling System, Bound.-Lay. Meteorol., 155, 87–109, doi: 10.1007/s10546-015-0020-1.

Yokota, T., Yoshida, Y., Eguchi, N., Ota, Y., Tanaka, T., Watanabe, H. et al. (2009). Global concentrations of CO_2 and CH_4 retrieved from GOSAT: First preliminary results. *Sola*, *5*, pp.160-163.

Yoshida, Y., Ota, Y., Eguchi, N., Kikuchi, N., Nobuta, K., Tran, H., et al. (2011). Retrieval algorithm for CO_2 and CH_4 column abundances from short-wavelength infrared spectral observations by the Greenhouse gases observing satellite, Atmos. Meas. Tech., 4, 717–734, doi:10.5194/amt-4-717-2011.

Yoshida, N., Toyoda, N., 2000. Constraining the atmospheric N2O budget from intramolecular site preference in N_2O isotopomers. Nature. 405, 330-334. https://doi.org/10.1038/35012558.

Zavala-Araiza, D., Lyon, D., Alvarez, R. A., Palacios, V., Harriss, R., Lan, X., et al. (2015). Toward a functional definition of methane super-emitters: Application to natural gas production sites. *Environmental science & technology*, *49*(13), 8167-8174. https://doi.org/10.1021/acs.est.5b00133.

Zeng, Z. C., Natraj, V., Xu, F., Pongetti, T. J., Shia, R. L., Kort, E. A., Toon, G. C., Sander, S. P., Yung, Y. L., 2018. Constraining Aerosol Vertical Profile in the Boundary Layer Using Hyperspectral Measurements of Oxygen Absorption. *Geophys. Res. Lett.* 45 (19), 10-772- 10-778. https://doi.org/10.1029/2018GL079286.

Zeng, Z. C., Xu, F., Natraj, V., Pongetti, T. J., Shia, R. L., Zhang, Q, Sander, S. P., Yung, Y. L., 2020. Remote Sensing of Angular Scattering Effect of Aerosols in a North America Megacity. Rem. Sens. Environ. 242, 11760. https://doi.org/10.1016/j.rse.2020.111760.

Zeng, Z.-C., Zhang, Q., Natraj, V., Margolis, J. S., Shia, R.-L., Newman, S., et al., 2017. Aerosol scattering effects on water vapor retrievals over the Los Angeles Basin, Atmos. Chem. Phys., 17, 2495–2508, doi:10.5194/acp-17-2495-2017.

Zeng, Z. C., V. Natraj, F. Xu, T. J. Pongetti, R.-L. Shia, E. A. Kort, et al., 2018. Constraining aerosol vertical profile in the boundary layer using hyperspectral measurements of oxygen absorption, Geophys. Res. Lett., doi:10.1029/2018GL079286.

Zeng, Z.C., Chen, S., Natraj, V., Le, T., Xu, F., Merrelli, A., Crisp, D., Sander, S.P. and Yung, Y.L., 2020a. Constraining the vertical distribution of coastal dust aerosol using OCO-2 O_2 A-band measurements, Remote Sens. Environ., 236, 111494, doi: 10.1016/j.rse.2019.111494.

Zeng, Z.-C., F. Xu, V. Natraj, T. J. Pongetti, R.-L. Shia, Q. Zhang, S. P. Sander, and Y. L. Yung, 2020b. Remote sensing of angular scattering effect of aerosols in a North American megacity, Remote Sens. Environ., doi:10.1016/j.rse.2020.111760.

Zhang, Q., Natraj, V., Li, K.-F., Shia, R.-L., Fu, D., Pongetti, T. J., Sander, S. P., Roehl, C. M., Yung, Y. L., 2015. Accounting for aerosol scattering in the CLARS retrieval of column averaged CO2 mixing ratios. J. Geophys. Res. Atmos., 120, 7205–7218, https://doi.org/10.1002/2015JD023499

Zhiseng, Y. Pelster, D. E., Liu, C., Zheng, X., Butterbach-Bahl, K. 2020. Soil N intensity as a measure to estimate annual N_2O and NO fluxes from natural and managed ecosystems. Curr. Opin. Environ. Sustain. 47, 1-6. https://doi.org/10.1016/j.cosust.2020.03.008.

Zhou, M., Langerock, B., Wells, K. C., Millet, D. B., Vigouroux, C., Sha, M. K., Hermans, C., Metzger, J.-M., Kivi, R., Heikkinen, P., Smale, D., Pollard, D. F., Jones, N., Deutscher, N. M., Blumenstock, T., Schneider, M., Palm, M., Notholt, J., Hannigan, J. W., and De Mazière, M., 2019. An intercomparison of total column-averaged nitrous oxide between ground-based FTIR TCCON and NDACC measurements at seven sites and comparisons with the GEOS-Chem model. Atmos. Meas. Tech. 12, 1393–1408. https://doi.org/10.5194/amt-12-1393-2019.

Acknowledgements

The CLARS project receives support from the California Air Resources Board. The views expressed in this article are those of the authors and do not necessarily reflect the official opinions of the funding agencies for this work. The CLARS team has continuously received support from our colleagues and collaborators and we would like to acknowledge their help here. On the CLARS methane work, we gratefully acknowledge discussions with M. Fischer, G. Heath, J. Hedelius, M. Weitz and V. Camobreco. We thank A. Andrews and E. Dlugokencky for providing the NOAA flask measurements at Mt. Wilson Observatory. On the CLARS N_2O work, O. A. acknowledges support from the Jet Propulsion Laboratory (Maximizing Student Potential in STEM) and from Occidental College (NSF COSMOS). On the CLARS CO work, we thank the reviewers and Drs. Nehzat Motallebi, Matthias Falk, and Abhilash Vijayan at California Air Resources Board for constructive comments and suggestions that helped improve the manuscript. Discussions with Yi Yin and Jiani Yang at Caltech, Dylan Jones at University of Toronto, and Paul O. Wennberg at Caltech, are acknowledged. We thank Dr. Jochen Stutz and his staff for establishing and maintaining the AERONET Caltech site. We also thank Dr. Pavel Ionov and his staff for establishing and maintaining the AERONET El Segundo site. The AERONET data for Caltech and El Segundo are available at https://aeronet.gsfc.nasa.gov/. The CO emission inventories are downloaded from EPA (available at https://www.epa.gov/air-emissions-inventories/national-emissions-inventory-nei). We would like to acknowledge high-performance computing support to Z.-C. Zeng (UCIT0004) from Cheyenne (doi:10.5065/D6RX99HX) provided by NCAR's Computational and Information Systems Laboratory, sponsored by the National Science Foundation. WRF-Chem is developed and distributed by NCAR (available at https://www2.acom.ucar.edu/wrf-chem). We thank the European Centre for Medium-Range Weather Forecasts (ECMWF) for providing the ERA5 reanalysis dataset, available at https://www.ecmwf.int/en/forecasts/datasets/reanalysis-datasets/era5. On the CLARS aerosol work, our collaborator Vijay Natraj acknowledges support from the NASA Earth Science US Participating Investigator program (solicitation NNH16ZDA001N-ESUSPI), and collaborator Feng Xu acknowledges support from the NASA Remote Sensing Theory program under grant 14-RST14-0100. We are also thankful for the support from the Jet Propulsion Laboratory Research and Technology Development Program. MERRAero is available from NASA GMAO at https://gmao.gsfc.nasa.gov/reanalysis/MERRA/. CLARS-FTS data are available at the following archive: https://data.caltech.edu/records/1985. The DOI of the archive is https://doi.org/10.22002/D1.1985. A portion of this research was carried out at the Jet Propulsion Laboratory, California Institute of Technology, under a contract with the National Aeronautics and Space Administration.